TECHNISCHE UNIVERSITÄT MÜNCHEN
Lehrstuhl für Aerodynamik und Strömungsmechanik

Quantitative Analysis of Vehicle Aerodynamics during Crosswind Gusts

Johannes D. Wojciak

Preface

The work in hand is the result of my activities as research fellow at the Institute of Aerodynamics and Fluid Dynamics at Technische Universität München. The thesis was carried out within a joint research project with BMW Group AG.

First of all I want to thank my supervisors Prof. Dr.-Ing. habil. Nikolaus A. Adams and Dr.-Ing. Thomas Indinger for their trustful guidance and their support during my working period. The time they devoted to me as well as their technical and personal advice formed the basis of my thesis. I also thank Prof. Dr. rer. nat. habil. Christian J. Kähler and Prof. Dr.-Ing. Hans-Jakob Kaltenbach, who consented to join the board of examiners.

Since this work has been heavily supported by the department of aerodynamics at BMW Group AG, I would like to express my special gratitude, amongst many colleagues of that department, to their head Holger Winkelmann as well as to Dr.-Ing. Rainer Demuth, who both monitored the joint project and actively contributed with their technical advice to a successful outcome. Furthermore, I appreciate the assistance of the technical staff at BMW's department for wind tunnel operations, the department for model design and construction and the group specialized on geometries and surface data as well as many others, who assisted me in setting up the experiments necessary for this work.

The same applies to the technical staff at the Institute of Aerodynamics and Fluid Mechanics at TUM, who supported the wind tunnel experiments at BMW's facility. Thanks to Sven Martinek and Christian Stemmer for solving a lot of IT problems and to Leibnitz Rechenzentrum for providing computational resources. In particular, the kind collaboration with the colleagues of the institute and within the young group of vehicle aerodynamics is acknowledged. Technical and informal discussions helped me to learn about fluid mechanics, working methods, foreign countries and private issues. Special thanks to my co-lecturers, who proofread my manuscripts.

Next, I would like to thank my many international colleagues that I have got to know during the last years and who taught me a lot when discussing at conferences, via e-mails or via their publications. The most important technical assistance, however, has been provided by the tight collaboration with Pascal Theissen, who worked at BMW on the same project at the same time. The daily dispute, a vast number of meetings, countless hours of preparation for the experiments, night shifts in the wind tunnel, common lunches, the trip to New York and the occasional beer in the evening are warmly appreciated. In that time a close friendship developed!

Above all, this thesis has been written with all the support of my family. Many thanks!

München, January 2012

Abstract

Aerodynamics in gusty crosswind conditions will be of increased significance in the future vehicle development process. Recent investigations demonstrated that unsteady aerodynamic loads can exceed steady loads considerably which may deteriorate driving stability. In order to compute and finally evaluate the vehicle response to a crosswind gust, it is essential to correctly determine the aerodynamic excitation of the vehicle.

One of the achievements of this thesis is to provide detailed information on the oncoming flow which faces a vehicle during crosswind gusts. According to on-road tests at Beaufort 4–7, turbulence length scales are between $10\,\mathrm{m}$ and $80\,\mathrm{m}$ and velocity distortions are maximum $8\,\mathrm{m/s}$. At $140\,\mathrm{km/h}$ vehicle speed this translates into excitation frequencies between $0.5\,\mathrm{Hz}$ and $4\,\mathrm{Hz}$ at maximum $13°$ yaw angle. Thus, it is proved that velocity distortions have been exaggerated in the past and pointed out, which turbulence scales have to be considered instead in the future development process.

This information is then used to set up an experiment that replicates realistic unsteady flow conditions, as they occur during crosswind gusts. To this end, a 1:2 scale generic notchback model is oscillated around its vertical axis while being exposed to constant oncoming flow in a wind tunnel. Characteristic mechanisms of fluid behavior and resulting surface pressure developments are revealed. It is verified that a delayed reaction of the wake flow to a change of the oncoming flow leads to enhanced and delayed surface pressure oscillations at the rear. This results in a lateral force at the rear which increases the total unsteady yaw moment amplitude and decreases the total side force amplitude.

The difference between unsteady and quasi-steady loads is shown to be constant for oscillation amplitudes between $\pm 2.2°$ and $\pm 4.4°$. Instead, the unsteady mechanism depends on the Strouhal number. Largest unsteady to quasi-steady yaw moment is observed, when the time scale of the model oscillation and the time scale of the wake flow are proportioned so that $\mathrm{Sr} = 0.12$. Although the position and the intensity of that peak depend on the vehicle shape, identical qualitative behavior is observed for fastback and station wagon variants, as well. In particular, the yaw moment overshoot turns out to be slightly smaller for the station wagon.

In the following, the experimental results are used to validate a CFD simulation tool. Though the general characteristics of the unsteady mechanism are correctly reproduced, numerical errors appear which prohibit its application for a reliable prediction of unsteady aerodynamic loads in industry. It is indicated that these deficiencies do not appear for simplified underfloor geometries or reduced ground clearance and can be overcome by applying a different turbulence model that requires the usage of another solver.

Zusammenfassung

Die Aerodynamik in böigem Seitenwind wird in der zukünftigen Fahrzeugentwicklung an Bedeutung gewinnen. Neueste Untersuchungen zeigten, dass instationäre aerodynamische Kräfte deren stationäre Referenzwerte erheblich übertreffen können, was eine mögliche Minderung der Fahrstabilität nach sich zieht. Um die Fahrzeugantwort auf Seitenwindböen berechnen und später bewerten zu können, ist es unerlässlich, die aerodynamische Anregung des Fahrzeugs korrekt zu bestimmen.

Eine Errungenschaft der vorliegenden Arbeit sind detaillierte Information über die bei Seitenwindböen auf ein Fahrzeug treffende Strömung. Turbulente Längenskalen bei Beaufort 4–7 sind gemäß den Ergebnissen von Fahrversuchen zwischen 10 m und 80 m und Geschwindigkeitsänderungen sind maximal 8 m/s. Bei 140 km/h Fahrzeuggeschwindigkeit ergibt sich daraus eine Fahrzeuganregung zwischen 0.5 Hz und 4 Hz und ein maximaler Anströmwinkel von 13°. So wird belegt, dass Geschwindigkeitsstörungen in der Vergangenheit überzeichnet wurden und aufgezeigt, welche Turbulenzskalen anstelle dessen in zukünftigen Entwicklungsprozessen berücksichtigt werden müssen.

Diese Information wird in der Folge für einen experimentellen Aufbau verwendet, welcher realistische instationäre Strömungsbedingungen bei Seitenwindböen nachbildet. Dabei wird ein 1:2 Modell eines generischen Stufenhecks bei Geradanströmung in einem Windkanal um seine Hochachse oszilliert. Charakteristische Strömungsmechanismen und daraus resultierende Entwicklungen der Oberflächendruckverteilungen werden erörtert. Es wird belegt, dass eine verzögerte Reaktion des Nachlaufs auf eine Anströmungsänderung zu verstärkten und verzögerten Druckschwankungen auf der Heckoberfläche führen. Im Gegenzug entsteht eine Seitenkraftkomponente, welche die Giermomentamplitude vergrößert und die Seitenkraftamplitude verringert.

Der Unterschied zwischen instationären und quasi-stationären Lasten ist für Oszillationsamplituden zwischen $\pm 2.2°$ und $\pm 4.4°$ konstant. Stattdessen hängt der instationäre Mechanismus von der Strouhal Zahl ab. Größtes instationäres zu quasi-stationäres Giermoment stellt sich ein, wenn die Zeitskale der Modelloszillation so im Verhältnis zur Zeitskale der Nachlaufströmung steht, dass $Sr = 0.12$. Obwohl die Lage und Stärke dieser Überhöhung von der Fahrzeugform abhängen, ergibt sich für Fließheck- und Vollheckvarianten identisches qualitatives Verhalten. Im Einzelnen ist die Giermomentenüberhöhung für das Vollheck am geringsten.

Nachfolgend werden die experimentellen Ergebnisse benutzt, um einen CFD-Löser zu validieren. Obwohl die grundsätzlichen Merkmale des instationären Wirkmechanismus richtig widergegeben werden, treten numerische Fehler auf, welche eine industrielle Anwendung zur zuverlässigen Vorhersage instationärer aerodynamischer Lasten nicht zulassen. Es wird aufgezeigt, dass dieser Mangel bei vereinfachten Unterbodengeometrien oder reduziertem Bodenabstand nicht entsteht und durch Anwendung eines anderen Turbulenzmodells behoben werden kann, was einen alternativen Strömungslöser erfordert.

Contents

Nomenclature

Latin symbols

a	m/s	Speed of sound
A_x	m^2	Cross-section in x-direction
A_y	m^2	Cross-section in y-direction
B	–	Beaufort scale number
B_{veh}	m	Width of vehicle
c_f	–	Friction coefficient
C_i	–	Force coefficient in i direction
C_{M_i}	–	Moment coefficient in i direction
C_p	–	Pressure coefficient
$C_{p,tot}$	–	Total pressure coefficient
f	–	Particle distribution function
f	Hz	Frequency
F	N	Force
g	m/s^2	Gravitation
H_{veh}	m	Height of vehicle
k	m^2/s^2	Turbulent kinetic energy
Kn	–	Knudsen number
L	m	Characteristic dimension
$\mathcal{L}$	m	Turbulence length scale
L_{veh}	m	Length of vehicle
L_{wb}	m	Wheel base
m	kg	Mass
M	Nm	Moment
Ma	–	Mach number
p	N/m^2	Pressure
$\mathcal{P}$	m^2/s^3	Production rate of turbulent kinetic energy
Pr	–	Prandtl number
R	Nm/kgK	Ideal gas constant
Re	–	Reynolds number
S	s^{-1}	Modulus of the mean rate of strain tensor

$\langle S_{ij} \rangle$	s^{-1}	Mean rate of strain tensor
S_u	m^2/s	Spectral power density of u
Sr	–	Strouhal number
t	s	Time
T	s	Oscillation period
T	s	Characteristic time
$\mathcal{T}$	s	Turbulence time scale
Tu	–	Turbulence intensity
u	m/s	First component of the Cartesian velocity vector or in index notation any component of the Cartesian velocity vector or velocity in main flow direction
u, v, w	m/s	Components of the Cartesian velocity vector in x-, y-, z-direction
$\boldsymbol{u}$	m/s	Resulting velocity vector
U	m/s	Euklid norm of the velocity vector
u_τ	m/s	Friction velocity
x	m	First Cartesian coordinate or in index notation any Cartesian coordinate
y	m	Second Cartesian coordinate or wall-normal direction
x, y, z	m	Cartesian coordinates
$\boldsymbol{x}$	m	Position vector

Greek symbols

β	°	Yaw angle
β	K^{-1}	Thermal expansion coefficient
γ	–	Adiabatic index
δ_{ij}	–	Kronecker Delta ($\delta_{ij} = 1$ for $i = j$, $\delta_{ij} = 0$ for $i \neq j$)
δt	s	Time step
Δt	s	Time lag
ε	m^2/s^3	(Turbulent) dissipation rate
ϑ	K	Temperature
κ	–	Von Kármán constant
λ	m	Free path
μ	kg/ms	Dynamic viscosity
ν	m^2/s	Kinematic viscosity
ν_t	Pa s	Eddy viscosity
ξ	–	Particle velocity
π	–	Ratio of circle's circumference to diameter (≈ 3.1416)
ρ	kg/m^3	Density

x

σ	–	Standard deviation
τ	N/m^2	(Shear) stress
ϕ	–	Flow quantity
ω	s^{-1}	Vorticity
ω	s^{-1}	Angular frequency
ω_{coll}	s^{-1}	Collision frequency
$\langle \Omega_{ij} \rangle$	s^{-1}	Mean rate of rotation tensor

Sub- and superscripts

amp	Amplitude
b	Buoyancy
$coll$	Collision
eff	Effective
eq	Equilibrium
i, j, k	In i, j, k-direction
ref	Reference
rel	Relative
t	Turbulent
tot	Total
veh	Vehicle
w	Wall
wb	Wheelbase
$wind$	Wind
x, y, z	In x, y, z-direction
ϕ'	Fluctuating part of a parameter ($\phi' = \phi - \langle \phi \rangle$)
$\langle \phi \rangle$	Arithmetic averaged parameter (ensemble-averaged)
$\overline{\phi}$	Time averaged parameter
∞	Not disturbed by the object of investigation
$+$	Non dimensional quantity in wall units

Symbols

$|a|$	Absolute value of a
$\max(a, b)$	Maximum of a and b
$\min(a, b)$	Minimum of a and b
$\boldsymbol{a}$	Vector
Δ	Variation or difference of a parameter

Abbreviations

CAD	Computer aided design
CFD	Computational fluid dynamics
BGK	Bhatangar, Gross and Krook (-model)
FFT	Fast Fourier transformation
FOAM	Field operation and manipulation
GAMG	Geometric-algebraic multi-grid
GGI	Generalized grid interface
LB	Lattice Boltzmann
M	Million
QS	Quasi steady
RANS	Reynolds-averaged Navier-Stokes (-equations or -model)
RNG	Re-normalization group
SIMPLE	Semi-implicit method for pressure linked equations
SST	Shear stress transport (-turbulence model)
TUM	Technische Universitaet Muenchen
URANS	Unsteady Reynolds-averaged Navier-Stokes (-equations or -model)
US	Unsteady

1 Motivation and objectives

1.1 Introduction

Recently, car manufacturers expanded their effort to improve the aerodynamic properties of vehicles in order to reduce CO_2 emissions and to contribute to a reduction of fuel consumption. However, the industrial development processes is often limited to the optimization of the flow around a vehicle during steady and low turbulent flow conditions at zero incident flow angle.

In fact, the flow conditions met on-road can be very turbulent and unsteady. Turbulence is on the one hand part of the atmospheric flow itself and on the other hand generated by interaction of the atmospheric flow with obstacles or traffic participants. Particularly unsteady flow conditions occur for instance during passing maneuvers, follow-up driving, passing of road-side obstacles or during wind gusts. This work deals with crosswind gusts, since they are considered most severe regarding driving stability.

As known from aircraft aerodynamics during landing, crosswind gusts can be a safety and comfort issue when hitting a vehicle particularly at high speeds. According to an encyclopedia[1], crosswind is a "strong wind that blows across the direction that vehicles, boats, or aircraft are traveling in, and that makes it difficult for them to keep moving steadily forward". The latter is certainly true for large vehicles such as railways and trucks. Still, a trend towards aerodynamically more efficient passenger cars can have an adverse effect on their driving stability and thus on their safety and comfort, as well. In combination with increasing use of lightweight materials and taller vehicle concepts a reliable analysis and prediction of crosswind sensitivity becomes indispensable within the aerodynamic development process of future passenger cars.

Crosswind sensitivity is, however, not only an aerodynamic issue. Depending on the dynamics of the vehicle suspension and the behavior of the driver, an aerodynamic excitation may be enhanced or damped. Investigations on the interaction of these disciplines were performed for instance by Schaible [91], Wagner [119] and Schrefl [93] during on-road testing. Their approach is suitable for an analysis of the complete system, but lacks reproducibility and exact definition of the aerodynamic excitation. Furthermore, a prototype of the test vehicle is required, which is usually not available at an early development stage.

The work in hand does not aim for a global investigation of crosswind sensitivity. Instead, vehicle dynamics and the driver are left aside and it is concentrated on the aerodynamic loads. An exact definition of on-road flow conditions during crosswind gusts and a quan-

---

[1]http://woerterbuch.reverso.net/englisch-cobuild/crosswind

titative estimation of how accurate unsteady aerodynamic loads can be numerically predicted are issues that have not been fully addressed in the past. However, this information is indispensable, since simulation tools are highly desirable in a development process to accurately predict aerodynamic loads.

1.2 Definitions

1.2.1 Coordinate system

The vehicle coordinate system is defined as outlined in Figure 1.1. The x-axis points towards the rear of the vehicle, the y-axis towards the right vehicle side and the z-axis towards the vehicle roof. The origin of the coordinate system is located at mid width of the front axis. The velocity components u, v and w denote the velocity components in x-, y- and z-direction, respectively. The forces C_x, C_y and C_z are defined accordingly. The moments C_{M_x}, C_{M_y} and C_{M_z} are defined around the corresponding axes according to the right-hand rule. The moment reference point is located at mid wheel base in x-direction, symmetry plane in y-direction and at minimum bound of the wheels in z-direction. The yaw angle β describes the angle of incidence of the oncoming velocity vector in the x-y-plane. The yaw angle β is positive, if the flow faces the vehicle from the right co-driver side. This corresponds to a positive rotation of the vehicle around the z-axis according to the right-hand rule. Figure 1.1 indicates the original and the rotated x-axis for a positive yaw angle β.
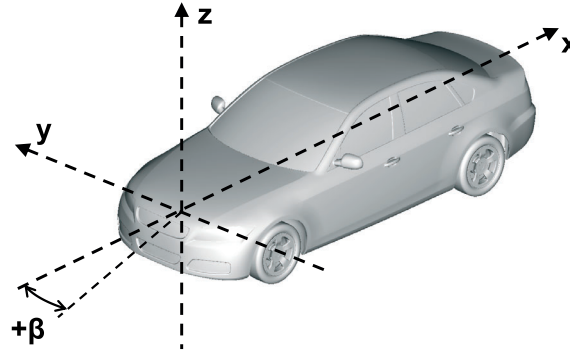
Figure 1.1: Coordinate system.

1.2.2 Dimensionless flow parameters

A fluid flow is characterized by dimensionless flow parameters. Similarity of these parameters ensures similar flow phenomena when modeling the flow in different geometric scales. The dimensionless parameters relevant for the work in hand are defined as follows.

Reynolds number The Reynolds number Re is defined as the ratio of inertial to viscous forces, see Equation 1.1. Therein, ρ denotes the fluid density, ν and μ are the kinematic

and dynamic viscosity of the fluid and U and L are a characteristic velocity and dimension of the flow problem.

$$\mathrm{Re} = \frac{\rho \cdot U \cdot \mathrm{L}}{\mu} = \frac{U \cdot \mathrm{L}}{\nu} \tag{1.1}$$

Strouhal number   The Strouhal number Sr is defined as a non-dimensional frequency. Here, the frequency of the gust distortion f is related to a characteristic dimension L and a characteristic velocity U of the flow problem,

$$\mathrm{Sr} = \frac{f \cdot \mathrm{L}}{U}. \tag{1.2}$$

In this work, the vehicle length L_{veh} is used as characteristic length L for Reynolds and Strouhal number.

Mach number   The Mach number is defined as the ratio of the flow velocity U and the speed of sound a,

$$\mathrm{Ma} = \frac{U}{a} = \frac{U}{\sqrt{\gamma R \vartheta}}. \tag{1.3}$$

The speed of sound can be derived from the temperature ϑ, the ideal gas constant R and the adiabatic index γ. The Mach number is a measure for the compressibility of flows, which must be regarded as significant for $\mathrm{Ma} \gtrsim 0.3$.

Dimensionless pressures and loads   The dimensionless pressure coefficient C_p is defined as the difference of pressure p and a reference pressure p_{ref} related to the dynamic pressure $\frac{\rho}{2}U^2$,

$$C_p = \frac{p - p_{ref}}{\frac{\rho}{2}U^2}. \tag{1.4}$$

The ambient pressure is usually chosen as reference pressure p_{ref}. The dimensionless total pressure coefficient $C_{p,tot}$ is defined accordingly with the total pressure p_{tot} instead of the pressure p,

$$C_{p,tot} = \frac{p_{tot} - p_{ref}}{\frac{\rho}{2}U^2}. \tag{1.5}$$

Forces and moments are non-dimensionalized as in Equations 1.6 and Equation 1.7 for $i = x, y, z$. The frontal cross section area A_x and the wheelbase L_{wb} of the vehicle are used as reference area and reference length.

$$C_i = \frac{F_i}{\frac{\rho}{2}U^2 A_x} \tag{1.6}$$

$$C_{M_i} = \frac{M_i}{\frac{\rho}{2}U^2 A_x L_{wb}} \tag{1.7}$$

1.2.3 Quasi-steady approximation

In this work, the term "quasi-steady" is frequently used. Here, it is defined as follows. A quasi-steady development of the flow and its properties means that the flow reaches steady state at each time step of its change. For instance, during a sinusoidal change of a flow situation, the flow properties would exhibit in-phase periodic changes, as well. Hence, the quasi-steady approach does not account for unsteady phenomena, which may alter the amplitude or the phase of the flow property transients. Indeed, the quasi-steady approximation is a rough estimation of unsteady developments based on property values encountered during steady conditions. Quasi-steady load transients are commonly derived by interpolating between minimum and maximum steady loads according to the change of yaw angle. Since this procedure is based on a linear dependency of the aerodynamic loads against yaw angle changes, it is only applicable for side force, roll and yaw moment.

The magnification factor describes the ratio of unsteady to quasi-steady amplitude of a flow property development. The time shift describes the phase lag of unsteady and quasi-steady developments of a flow property. In this work, a positive time shift means that the unsteady signal lags behind the quasi-steady approximation.

1.3 Background

In the following, an overview of previous investigations on aerodynamics of vehicles subjected to gusty crosswind is given. According to the main part of this work this section is subdivided into a discussion of the oncoming flow, followed by a description of experimental and numerical models for simulating vehicles being exposed to crosswind gusts.

1.3.1 Analysis of the oncoming flow field

Generally, the undisturbed velocity vector of the flow $\boldsymbol{u}$ facing a vehicle which is driving at the speed $\boldsymbol{u}_{veh}$, is defined as

$$\boldsymbol{u}(\boldsymbol{x}, t) = -\boldsymbol{u}_{veh} + \boldsymbol{u}_{wind}(\boldsymbol{x}, t), \tag{1.8}$$

where $\boldsymbol{u}_{wind}$ denotes the wind velocity vector and $\boldsymbol{x}$ denotes the position vector. Assuming constant vehicle speed, the oncoming velocity vector $\boldsymbol{u}$ is entirely determined by the wind velocity distribution. Unfortunately, the latter highly fluctuates during wind gusts and is hard to assess.

1.3.1.1 Theoretical Framework

Saunders et al. [89] and Cooper [29] theoretically analyzed the wind velocity distribution using fundamental correlations provided by Engineering Sciences Data Unit [36,37]. Based on the correlations deduced by von Kármán, spectral functions were provided for the

turbulent velocity vector encountered by a moving vehicle in windy conditions. According to their findings, the non-dimensional longitudinal energy spectrum is defined as

$$\frac{f \cdot S_u(f)}{\sigma_u^2} = \frac{4\frac{f \cdot \mathcal{L}_u}{\overline{U}}}{\left(1 + 70.8 \left(\frac{f \cdot \mathcal{L}_u}{\overline{U}}\right)^2\right)^{\frac{5}{6}}} \tag{1.9}$$

and the lateral and vertical energy spectra are defined as

$$\frac{f \cdot S_{v,w}(f)}{\sigma_{v,w}^2} = \frac{8\frac{f \cdot \mathcal{L}_{v,w}}{\overline{U}}\left(0.5 + 94.4 \left(\frac{f \cdot \mathcal{L}_{v,w}}{\overline{U}}\right)^2\right)}{\left(1 + 70.8 \left(\frac{f \cdot \mathcal{L}_{v,w}}{\overline{U}}\right)^2\right)^{\frac{11}{6}}} \tag{1.10}$$

with the power density $S_i(f)$, the frequency f, the mean velocity $\overline{U}$ and the longitudinal turbulence length scale $\mathcal{L}_i$ for $i = u, v, w$. Figure 1.2 illustrates a series of power spectra for various turbulence intensities and length scales. The turbulence intensity mainly determines the energy level, while the length scale determines the position of the roll-off point and predominantly shapes the power spectrum in the low frequency range.
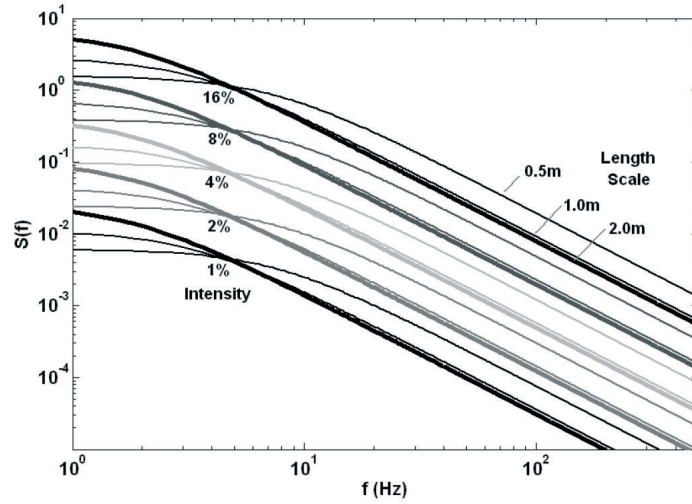
Figure 1.2: Examples of smoothed dimensional longitudinal power spectra for different turbulence intensities and length scales ($U_{veh} = 27.8 \, \text{m/s}$) from Wordley et al. [127].

1.3.1.2 Application to vehicle aerodynamics

According to its assumptions, the von Kármán spectrum is valid for homogeneous, isotropic turbulence in thermally stable flows. It was, however, unclear, whether these assumptions were satisfied in close proximity to the ground relevant for vehicle aerodynamics. As an example, fair agreement of the theoretical spectra and single measurements in close proximity to the ground at steady wind conditions and small surface roughness were reported in [27, 121]. However, measurement data in low heights were very limited. So, a profound validation of the theoretical spectra was not achievable. For this reason Cooper [27] and Watkins [121] thoroughly analyzed wind engineering data regarding

their eventual application to vehicle aerodynamics. These measurement data are usually recorded at 10 m above ground. Eventually, their extrapolation to vehicle heights around 1.5 m above ground turned out to be problematic [27, 85, 89, 126]. For this reason, it was lastly started to systematically assess the velocity distribution on-road in the recent past. Albeit the focus was mostly within constant wind and albeit gusty crosswind was not considered, the approach and the results are still valuable information for the subsequent gust analysis of the present work.

1.3.1.3 Measurement setups

The most extensive attempt to measure on-road wind conditions in detail was conducted by Wordley and Saunders [89, 126, 127]. To the author's knowledge, they were the first to measure turbulence characteristics of the undisturbed oncoming flow by placing fluid probes in front of a vehicle.
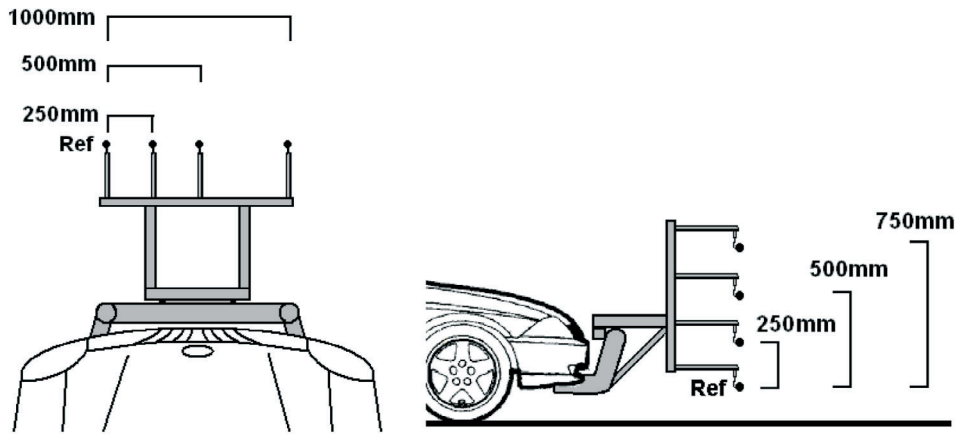
Figure 1.3: Top and side view of the measurement setup of Wordley et al. [127].

Figure 1.3 sketches the principal setup of Wordley et al., where a horizontal and a vertical array of four-hole dynamic pressure probes were located 1.0 m in front of a mid-sized passenger car. Wind tunnel as well as on-road tests showed that corrections for vehicle interference effects were not required for this setup for yaw angles up to 8°. A tri-axis accelerometer was mounted to the probe structure in order to correct the vertical component of the wind velocity for the pitching motion of the vehicle and the support structure.

In many other investigations the fluid probes were mounted above the roof, above the hood or in close proximity to the front end of a test vehicle. This is problematic as flow structures are strongly modified by the displacement effect of the vehicle, which alters the turbulence characteristics of the oncoming flow (compare Wordley et al. [126, 127]).

1.3.1.4 Steady wind conditions

Wordley et al. [126, 127] measured the oncoming flow field at a constant vehicle speed $U_{veh} = 100 \, \text{km/h}$ for several traffic and road-side conditions. However, these measure-

ments were conducted at steady wind conditions only and did not contain any transient events such as for example crosswind gusts or passing maneuvers. Still, the results are valuable in this context, since they provide an excellent reference data base of turbulence characteristics encountered at constant wind, including permanent head- or tailwind.
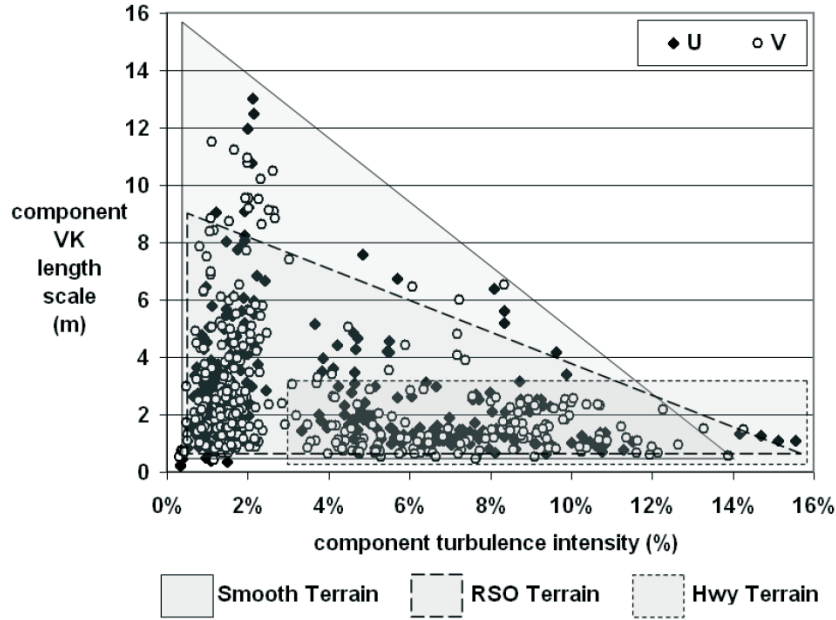

Figure 1.4: Turbulence intensities and length scales measured by Wordley et al. for different road conditions (RSO=roadside obstacles, Hwy=highway) [127].

Figure 1.4 summarizes how traffic and road-side conditions modify the turbulence characteristics of the oncoming flow field. According to Figure 1.4, the turbulence length scales decrease with increasing turbulence intensity for smooth terrains and terrains with roadside obstacles. Maximum length scales are $14\,\mathrm{m}$ and maximum turbulence intensities are 14%. On the other hand, length scales are generally small for highway traffic terrains, which is feasible, since turbulent structures are broken up by interaction with other traffic participants. At this point a comparison with other on-road tests is worth doing. As part of an aeroacoustic road-to-tunnel study, Lindener et al. [71] related smallest turbulence scales to strong traffic conditions, as well. The turbulence scales and intensities found by Oettle et al. [81] during on-road measurements for a correlation of turbulent oncoming flow and in-cabin noise are in a very similar range as those presented in Figure 1.4. To conclude, Wordley's results were confirmed independently by other studies.

Length scales in vertical direction were left out of Figure 1.4, since they were consistently less than $1\,\mathrm{m}$. The ratio of turbulence intensities in x-, y- and z- direction, known as the anisotropic ratio, was $\mathrm{Tu}_u \div \mathrm{Tu}_v \div \mathrm{Tu}_w = 1.00 \div 1.01 \div 0.61$, comparing well with on-road measurements of Lindener et al. [71] and Schröck et al. [95]. Note that the turbulence intensities by definition depend on the speed of the test vehicle (here $U_{veh} = 100\,\mathrm{km/h}$). In Figure 1.4 length scales were estimated by Kármán-fitting, which results in roughly half of the length scales using the auto-correlation method (compare Wordley et al. [126,127]).

Figure 1.5 and Figure 1.6 outline the influence of consistent tail- and headwind on turbulence intensity and length scale for smooth terrain. According to these figures, the turbulence intensity increases likewise with increasing tail- and headwind. The asymme-
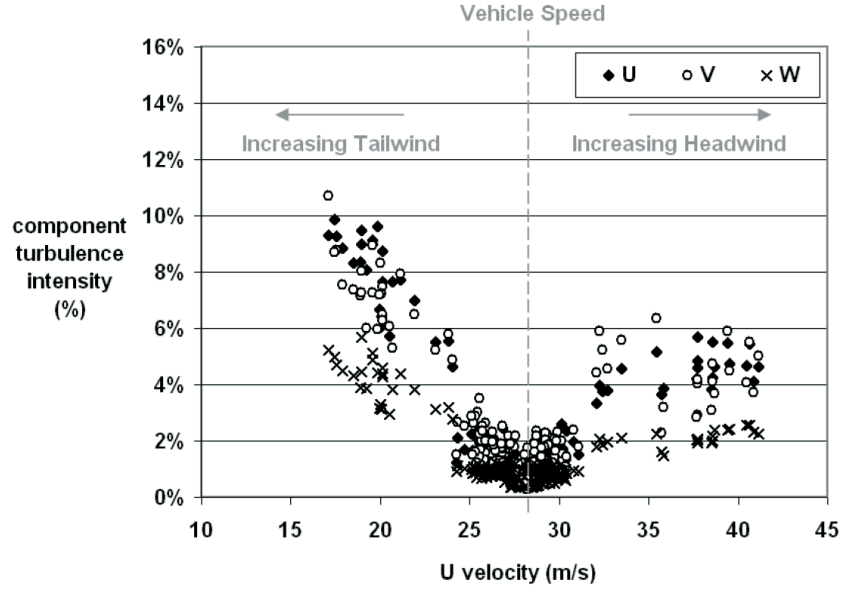
Figure 1.5: Turbulence intensity versus axial flow velocity as presented by Wordley et al. [127].

try in Figure 1.5 is due to the different velocities U, which form the denominator in the turbulence intensity term and can be removed by simply plotting the standard deviation. Subtracting the vehicle velocity gives turbulence intensities of solely the atmospheric wind of 19%, 17% and 10% for the u-, v- and w-velocity components. These values agree well with stationary measurements of Flay [45]. In addition to that, Wordley et al. also assessed the development of the turbulence length scale at tail- and headwind. Figure 1.6 outlines that the component length scales decrease similarly for increasing head- and tailwind.
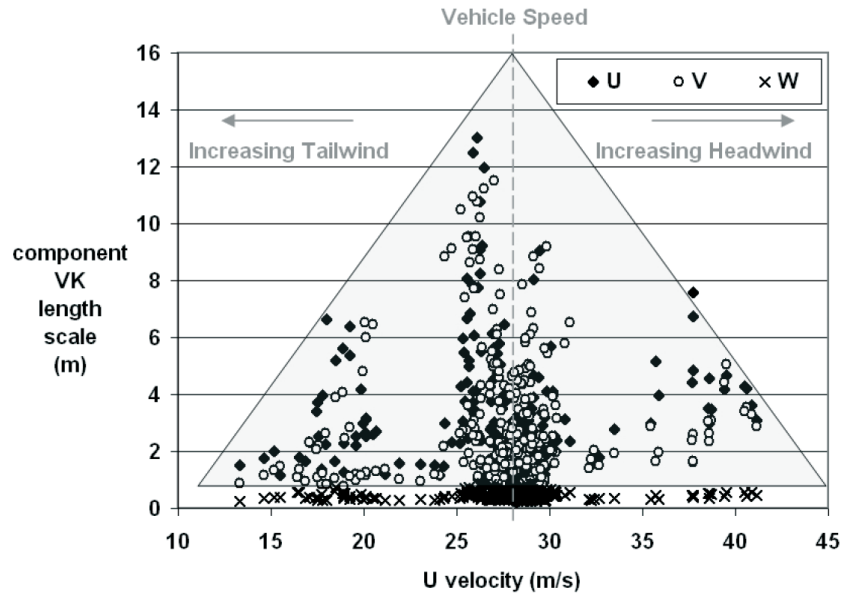
Figure 1.6: Turbulence length scale versus axial flow velocity as presented by Wordley et al. [127].

1.3.1.5 Unsteady wind conditions

Following the above, the oncoming velocity field is fairly well known at steady wind conditions. The opposite is true for unsteady conditions, where only occasional studies exist. These are briefly outlined below.

Schrefl [93] and Mayer et al. [74] conducted on-road measurements closed to the North Sea in Germany during heavy wind. They evaluated surface pressures, vehicle motions and the oncoming flow above the hood of their test vehicle. Maximum yaw angles of 9° were recorded at 200 km/h vehicle speed. Unfortunately, single gust events were not analyzed separately but only averaged power spectra were published. Thus, no further information on single gust events can be extracted from their results.

Schröck et al. [95] measured the oncoming flow during various ambient conditions on German highways between 140 km/h and 160 km/h vehicle speed. The front area of the vehicle was used as a fluid probe (based on [112]), which is debatable when aiming at assessing turbulence characteristics of the undisturbed flow. The results were classified into calm and windy measurement days as well as into little, moderate and strong traffic. Data were recorded over several hours and processed as initially presented by Wordley et al. [126, 127], although statistical stationary conditions were not satisfied. Finally, the results partly contradicted the findings of Wordley et al. [127]. According to Schröck et al., the turbulence intensity and the lateral length scale increase at strong wind, whereas the longitudinal length scale remains roughly constant. In contrast, Wordley stated that the length scales decrease with increasing turbulence intensity [126, 127]. As another disagreement, Schröck et al. reported maximum integral length scales three times as high as reported by Wordley et al. [127]. Unfortunately, Schröck et al. did not evaluate single gust events except for one transient measurement. There, a single wind gust led to a sudden, peak shaped yaw angle deviation of 6° resulting in a transient increase of the turbulence intensity up to 6% and of the length scale up to 70 m in longitudinal and 50 m in lateral direction.

Summing up, manifold and statistical relevant information about the flow field during single crosswind gusts are missing. To the author's knowledge, there is no investigation which allows to draw conclusions on the development of flow parameters and turbulence scales during single gust events.

1.3.2 Experimental modeling

1.3.2.1 First attempts

Though the flow field in gusty crosswind has not been sufficiently quantified until now, it was attempted very early to model gusty crosswind in experiments. In 1981, Cooper [28] was possibly the first to study an eventual overturning of trains in high cross wind by propelling a 1:5 scale train model along a 950 m long track in open air. He finally stated that "moving model experiments in the open air are expensive and difficult to perform and there is insufficient control over the experimental situation" [28]. Instead, he suggested "to

perform experiments with moving models through wind tunnel simulations of the earth boundary layer" [28].

1.3.2.2 Analytical descriptions

In 1984, Cooper provided an analytical framework for the computation of power spectral density of the aerodynamic side force during crosswind gusts and the ratio of unsteady to steady side force amplitude [29]. This framework was, however, based on a linear relationship between unsteady side force and turbulence velocity. Using this simplified model Cooper was able to prove that significant excitation of vehicle suspension modes with eigenfrequencies around 1 Hz may occur for vehicle speed above 40 m/s.

At the same time, Baker [4–7] analytically studied the behavior of ground vehicles in cross wind gusts, as well. Baker already predicted that quasi-steady approximation is valid for large turbulence scales and that the ratio of unsteady to steady loads can exhibit marked frequency peaks "under some conditions" [5]. However, experimental data were scarce in order to verify his analytical framework. In accordance to Cooper [29] he eventually stated the "need for a substantial experimental program, using moving models propelled through atmospheric turbulence" [6].

1.3.2.3 Propelled models and atmospheric boundary layer simulation

The results of several subsequent experimental campaigns, where models were catapulted across a wind tunnel, in which an atmospheric boundary layer was simulated upstream of the test section, were summarized by Baker [8]. The experimental setup for the simulation of an atmospheric boundary layer had been adopted from investigations on building aerodynamics. Using this setup, Baker reported ratios of unsteady to steady loads above one. Interestingly, these ratios were larger for small yaw angles (10°) than for extreme yaw angles (45-90°). This could not be explained by Baker's analytical framework [4–6], which revealed a general problem: due to a lack of reliable experimental data of the relation between unsteady and quasi-steady loads, analytical models could not be validated.

In order to acquire these data, the suggestion of propelling models across a wind tunnel with atmospheric boundary layer turned out to be detrimental. The specification of a reference height for velocities was difficult, since little was known about the boundary layer in close vicinity to the ground. Besides, the setup was very complex and allowed to model only very high yaw angle flow conditions. Moreover, it was limited to very small model scales (approx. 1:50) and low wind speeds. Thus, only unrealistic Reynolds numbers could be achieved. Additionally, the signal to noise ratio was low and reproducibility was insufficient due to imperfect model propulsion units. Despite all these deficiencies, Kobayashi and Yamada [65] reported a yaw moment overshoot for a generic 1:10 scale model, which was catapulted with 7 m/s through a wind tunnel test section ($u_{wind} = 4$ m/s) leading to a sudden yaw angle of 30°. A delayed adaption of the flow on the leeward side was attributed to this phenomenon, given that full adaption to steady state was not achieved until four vehicle lengths.

1.3.2.4 Flapping wings and oscillating models

Later on, some other experimental techniques were tested and two principal approaches appeared most promising for generating reproducible time dependent oncoming flow conditions similar to crosswind gusts: First, oscillating devices such as airfoils were used upstream of the vehicle to deflect the flow. This approach was initially implemented by Bearman and Mullarkey [10], followed by Mullarkey [77] and Passmore et al. [83]. More recently, this technique was adopted by Cogotti et al. for Pininfarina's full scale wind tunnel [19, 24–26] and by Schroeck et al. [96, 97] for the FKFS model wind tunnel in Stuttgart. Second, time-dependent oncoming flow was generated by applying a rotational motion to the test model, as proposed by Garry and Cooper [46] and subsequently done by Passmore and Mansor [73, 82], Guilmineau and Chometon [50] and most recently by Theissen and the author of the work in hand [107, 111, 124].

The challenge of the first setup is to specify the time-dependent oncoming flow conditions as seen by the car, which differ slightly from the imposed flow deflection. Alternatively, when working with rotating models, mechanical inaccuracies often lead to poor reproducibility and large uncertainties of aerodynamic loads. Both experimental methods can lack in their ability of simulating velocity distortions of sufficiently high frequencies or amplitudes depending on the mechanical design of the test rig. Still, the results achieved using both approaches, which are chronologically outlined in the following, contributed to an improved physical understanding of unsteady aerodynamics during crosswind gusts.

Bearman and Mullarkey Bearman and Mullarkey [10] oscillated two airfoils in front of a generic vehicle model (Davis model) at $\text{Re} = 4.5 \cdot 10^5$ based on $L_{veh} = 0.3\,\text{m}$. They concluded that maximum side forces and yaw moments are conservatively approximated by steady values at maximum incident angle of the airfoils. Only for Strouhal numbers between 0.45 and 0.55, a yaw moment overshoot of approximately 10% was reported.

Garry and Cooper The results of Garry and Cooper [46], who rotated a generic model with $L_{veh} = 0.34\,\text{m}$ at constant yaw rates between $0.25°/\text{s}$ and $64°/\text{s}$ at $\text{Re} = 4.5 \cdot 10^5$, are in agreement with Bearman and Mullarkey [10] as the drag and yaw moment magnitudes did not differ from steady results. Instead, phase shifts of unsteady against steady load-to-yaw curves were observed, which depended on the yaw rate and the model geometry.

Passmore et al. Passmore et al. [83] worked with oscillating airfoils and a 1:6 scale Davis model at $\text{Re} = 1 \cdot 10^6$ and $0.03 \leq \text{Sr} \leq 0.23$. As opposed to preceding investigations, a significant overshoot of unsteady against steady yaw moment amplitudes of 5–30% was observed. In contrast, the unsteady side force exhibited smaller amplitudes than in the quasi-steady state. Furthermore, surface pressure oscillations lagged behind the model rotation at the model side (up to 140°), while they were in phase at the model front. For higher Strouhal numbers, the lagged pressure oscillations were restricted to the rear side. The largest pressure amplification at the rear was found for $0.03 \leq \text{Sr} \leq 0.06$.

Passmore and Mansor For unknown reasons, Passmore and Mansor [73, 82] later switched to the alternative approach using an oscillating 15% scale Davis model at $4.3 \cdot 10^5 \leq \mathrm{Re} \leq 1.7 \cdot 10^6$ and $0.02 \leq \mathrm{Sr} \leq 0.23$. Unsteady side force and yaw moment were reported to exceed their steady values up to four times. In combination with large fluctuations of the experimental data, the reproducibility might be impaired, which was not explicitly dealt with in that publication.

Schrefl and Mayer et al. Similar concerns were reported by Mayer et al. [74] and Schrefl [93], when testing a full scale notchback at $\mathrm{Re} = 1.2 \cdot 10^7$ and $0.01 \leq \mathrm{Sr} \leq 0.1$ in Pininfarina's wind tunnel facility with oscillating flap wings. In particular, the authors criticized the flow homogeneity and the reproducibility at higher frequencies. Still, a yaw moment overshoot occurred for $\mathrm{Sr} \geq 0.08$ with a maximum overshoot of 40% at $\mathrm{Sr} = 0.1$. The unsteady side force was consistently smaller than steady but increased with increasing frequency towards $\mathrm{Sr} = 0.1$.

Guilmineau and Chometon Guilmineau and Chometon [50] studied a generic train body oscillating at $\mathrm{Sr} = 0.07$ and $\mathrm{Re} = 0.9 \cdot 10^6$. In their experiment, pressure oscillations at the rear of the body exhibited hysteresis effects. A numerical validation confirmed this effect by drag, side force and yaw moment transients. A significant yaw moment overshoot of 20–25% is documented for an oscillation amplitude of $\pm 30°$, whereas it was insignificant for $\pm 10°$.
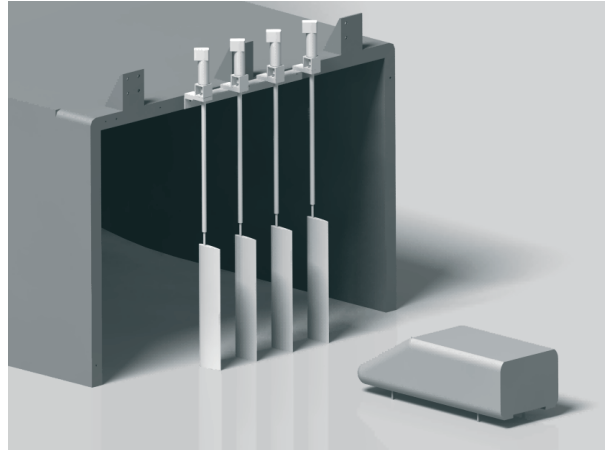
Figure 1.7: Model wind tunnel with oscillating flaps from Schröck et al. [96].

Schröck et al. Very recently, Schröck et al. [96,97] upgraded a model wind tunnel facility in Stuttgart by implementing oscillating flaps into the nozzle, see Figure 1.7. Using this setup they studied a 1:5 scale fastback and hatchback SAE model. The Reynolds number was $\mathrm{Re} = 4.5 \cdot 10^6$ and the Strouhal number varied according to the excitation of the flaps (max. amplitude $\pm 10°$) within a limited frequency range giving $0.0 \leq \mathrm{Sr} \leq 0.15$. It is reported that the unsteady yaw moment amplitude exceeds the steady yaw moment at maximum incident flap angle by 15% for $0.10 \leq \mathrm{Sr} \geq 0.15$. In contrast, the unsteady side force amplitudes are smaller than at steady conditions for the complete frequency range.

Dominy and Ryan   Besides all, Dominy and Ryan [34,87,88] came up with a completely different experimental setup using a main wind tunnel and a second cross wind tunnel, whose jet is impinged by a series of shutters along the test section of the main wind tunnel. Thus, a lateral flow distortion propagates along the test section giving a maximum yaw angle, which is fixed to around 30°. Their main goal was to increase the signal to noise ratio compared to other experimental approaches. At $Re = 3 \cdot 10^5$ and unknown Strouhal number, unsteady yaw moment and side force were reported to exceed steady values at $\beta = 30°$. However, deficiencies of the crosswind flow quality were eventually reported by Ryan [87] and no further results have been published since then.

Summary of experimental results   The most relevant information on unsteady vehicle aerodynamics during crosswind gusts found from experiments is the following:

- ▶ Unsteady load transients differ from quasi-steady developments.

- ▶ Very often, the unsteady yaw moment amplitude exceeds the steady value at maximum angular position of the flaps and the model, respectively.

- ▶ The differences between unsteady and steady loads depend on the Strouhal number and the yaw amplitude.

- ▶ Most experiments were carried out at unrealistically low Reynolds numbers.

- ▶ Strouhal numbers and yaw amplitudes simulated in the experiments varied a lot, since profound information on the oncoming flow during crosswind gusts is missing.

1.3.3 Numerical modeling

In the last years, numerical investigations of vehicle aerodynamics during crosswind gust events followed. The most relevant findings with respect to this work are briefly summarized below.

Demuth and Buck   Demuth and Buck modeled a single sinusoidal gust with a yaw angle change from $\beta = 0°$ to $\beta = 6°$ and back to $\beta = 0°$ passing a full scale notchback at $Re = 1.2 \cdot 10^7$ and $Sr = 0.12$ as well as at $Re = 1.7 \cdot 10^7$ and $Sr = 0.08$ [32]. The numerical study clearly revealed a yaw moment overshoot against quasi-steady approximation, which was attributed to loads at the vehicle rear. Experimental data were not available for validation.

Favre et al.   Favre et al. [38, 40–42] presented numerical investigations following the experiments of Chadwick et al. [20]. There, a generic station wagon (Windsor model) had been propelled along a track perpendicular to a wind tunnel, which translates to a trapezoidal variation of yaw angle with maximum $\beta = 20°$. The experiment was replicated by detached eddy simulation for $Re = 2.0 \cdot 10^6$ and $0.15 \leq Sr \leq 0.33$. Favre et al. reported

significant overshoot of unsteady against quasi-steady yaw moment amplitudes as well as a delay of unsteady against quasi-steady side force and roll moment transients for the times, where the model enters and leaves the crosswind zone. This was explained by a delayed reaction of the flow field on the leeward side. For Sr = 0.5 the yaw moment overshoot was more pronounced and no unsteady phenomena occurred at Sr = 0.1, which is in disagreement with other investigations, for instance Demuth and Buck [32]. An investigation of different rear screen angles gave the largest yaw moment overshoot but the smallest absolute yaw moment for a station wagon-similar 0° slant angle.

Tsubokura et al. Tsubokura and Nakashima et al. applied large eddy simulation to vehicle aerodynamics at sudden crosswind [115, 117]. First, their numerical setup was successfully validated against experimental results for steady flow conditions at $\beta \neq 0°$. Then, it was used for unsteady simulations of sudden crosswind, which was modeled as yaw angle step from $\beta = 0°$ to $\beta = 10°$, where it remained until steady flow conditions were reached. Then the yaw angle stepped back to $\beta = 0°$. The frequency of the steps was 10 Hz corresponding to a Strouhal number of Sr = 1.2 and the Reynolds number was Re = $1.0 \cdot 10^7$. Using this setup, asymmetric pressure distributions at the rear of a simplified full scale notchback were observed, which did not agree with steady results. Instead, the yaw moment was amplified at the beginning and at the end of the crosswind period.

In another study, Tsubokura et al. investigated a realistic but simplified station wagon subjected to a trapezoidal gust from 0° to 30° at Re = $2.9 \cdot 10^5$ [116]. There, an unsteady overshoot was observed for the yaw moment, but not for the side force. The phenomenon was attributed to a delayed reaction of the leeward flow.

In 2010, Tsubokura et al. applied their numerical method to a simplified heavy duty truck [118]. Experimental data from the DNW wind tunnel for $\beta = 0°, 3°, 5°, 10°$ were in good agreement with steady numerical results. According to their preceding study, a trapezoidal excitation from $\beta = 0°$ to $\beta = 10°$ was chosen to simulate sudden crosswind. The Reynolds number was Re = $1.7 \cdot 10^7$ based on the truck length of 12 m. The Strouhal number was Sr = 0.03. The unsteady yaw moment was observed to exceed the values encountered during steady simulations by a factor of almost 2. The unsteady side force, however, did not reach steady values. It was assumed that the pressure field responds quickly to a transition of the surrounding incoming field, but the velocity field reacts with a certain time delay. Hence, surface pressure oscillations were enhanced. Nakashima et al. [78, 79] extended the investigation of Tsubokura et al. [118] by coupling vehicle aerodynamics with vehicle dynamics. Thus, the vehicle response was assessed and compared with the response resulting from uncoupled simulations.

Later, Tsubokura et al. studied 1:4 scale notchback and station wagon geometries [114]. The notchback had a flat and a rugged underfloor. Sudden crosswind was modeled as trapezoidal excitation from $\beta = 0°$ to $\beta = 15°$ and the Reynolds number was Re = $2.5 \cdot 10^6$. Information on the Strouhal number was not given. Unsteady yaw moment magnification was most distinct for the notchback and for the flat underfloor. When comparing different underfloor geometries, largest surface pressure differences were surprisingly observed on the upper body . From this, Tsubokura et al. concluded that a

rugged underfloor diffuses the fluid momentum loss behind the front wheel resulting in less intense interaction with the rear wheel and its losses.

Mankowski et al. Mankowski et al. [72] recently conducted 2-dimensional simulations using a very generic body (Docton model) exposed to sinusoidal gusts at $\mathrm{Re} = 3.2 \cdot 10^6$ and $0.005 \leq \mathrm{Sr} \leq 1.4$. The implementation of gusts basically followed Demuth and Buck's approach. According to Mankowski et al. flow can be treated quasi steady for $\mathrm{Sr} \leq 0.05$, whereas a significant change of drag occurred for $0.05 \leq \mathrm{Sr} \leq 0.24$. The standard deviation of side force depended on the yaw amplitude, but decreased with increasing Strouhal number. In addition to that, Mankowski et al. made an interesting investigation on multiple frequency components. They studied a basic gust ($\mathrm{Sr} = 0.5$) superimposed with a low ($\mathrm{Sr} = 0.005$) and a high ($\mathrm{Sr} = 1.4$) frequency part, respectively. Finally, the additional frequency part did not have a summative impact, but corresponded to side force results from isolated simulations at $\mathrm{Sr} = 0.5$.

Summary of numerical results The most relevant information on unsteady vehicle aerodynamics during crosswind gusts found from numerical simulations is the following:

► Numerical simulations were frequently used to validate experimental results and hence limited to unrealistic flow conditions of the corresponding experiments.

► Numerical simulations of crosswind gusts have proved that unsteady aerodynamic loads on passenger vehicles during crosswind gusts differ significantly from quasi-steady loads.

► Most studies agree that unsteady yaw moment is underestimated and unsteady side force is overestimated by quasi-steady approximation of aerodynamic loads based on constant yaw data.

► Many studies report a delay of the side force transient against a yaw angle change.

► A delayed reaction of the flow field and enhanced pressure oscillations at the vehicle rear are sporadically documented.

► A consistent description of the physical mechanism is missing.

1.3.4 Experimental and numerical investigations of Theissen
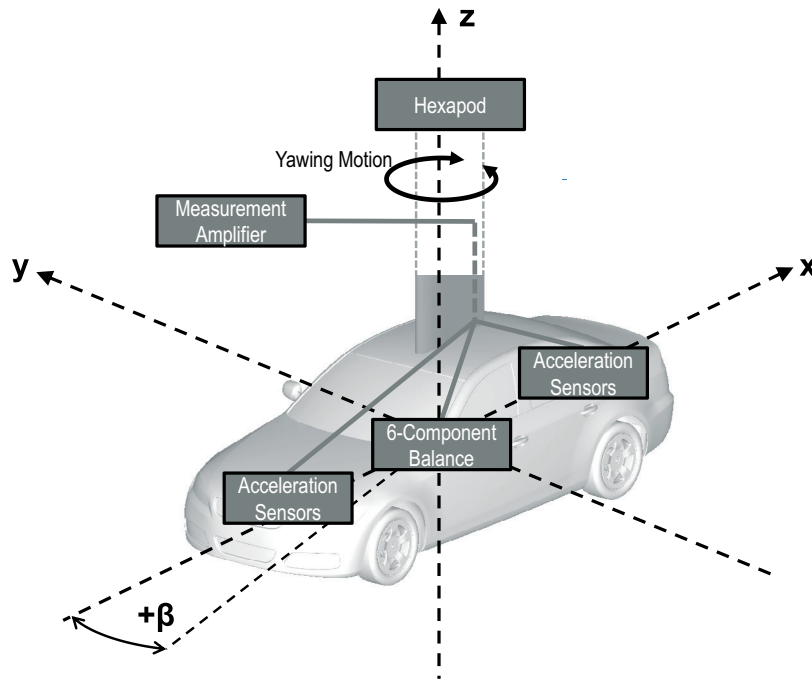
Results from Theissen [107, 108, 110, 111] are particularly relevant for the present work, since both have been very much interacting. Theissen's main objectives were the determination of unsteady aerodynamic loads of realistic vehicles during gusty crosswind, the detailed identification of the underlying flow mechanism and the analysis of sensitivities to geometric changes.

1.3.4.1 Numerical setup

In his numerical simulations, Theissen studied a slightly simplified BMW notchback geometry and the generic but realistic DrivAer model. He used time-dependent inlet boundary conditions to model sinusoidal oscillations of v. So, a lateral velocity distortion was created numerically, which propagated through the entire simulation domain and thereby passed the vehicle. The standard test case was at $Re = 1.2 \cdot 10^7$ and $Sr = 0.12$ with a maximum and minimum yaw angle of $\pm 3°$ and $\pm 6°$, respectively.

1.3.4.2 Experimental setup

An experimental setup was developed by Theissen and the author, where a 1:2 scale DrivAer notchback was oscillated around its vertical axis whilst being exposed to constant oncoming flow. This was implemented in BMW's Aerolab wind tunnel featuring a nozzle cross section of $14\,\mathrm{m}^2$, a single moving belt and boundary layer treatment. The model was mounted to a hexapod and was slightly lifted off the moving ground. In particular, the setup overcame the deficiencies of many experimental setups presented previously by measuring at realistic Reynolds and Strouhal numbers at the same time. For the standard test case, the Reynolds number was $0.89 \cdot 10^7$, the Strouhal number was 0.08 and the yaw angle amplitude was $\pm 3.3°$. The accuracy of the model motion prescribed by the hexapod unit was extraordinary, exhibiting maximum translatory errors in any direction of $4\,\mathrm{mm}$ and maximum rotational errors of $0.2°$. The setup is schematically outlined in Figure 1.8 and a detailed description can be found in [111] and [107].

Figure 1.8: Schematic view of the experimental setup from Theissen et al. [111].

(a) Drag

(b) Roll Moment

(c) Side Force

(d) Pitching Moment

(e) Lift Force

(f) Yaw Moment
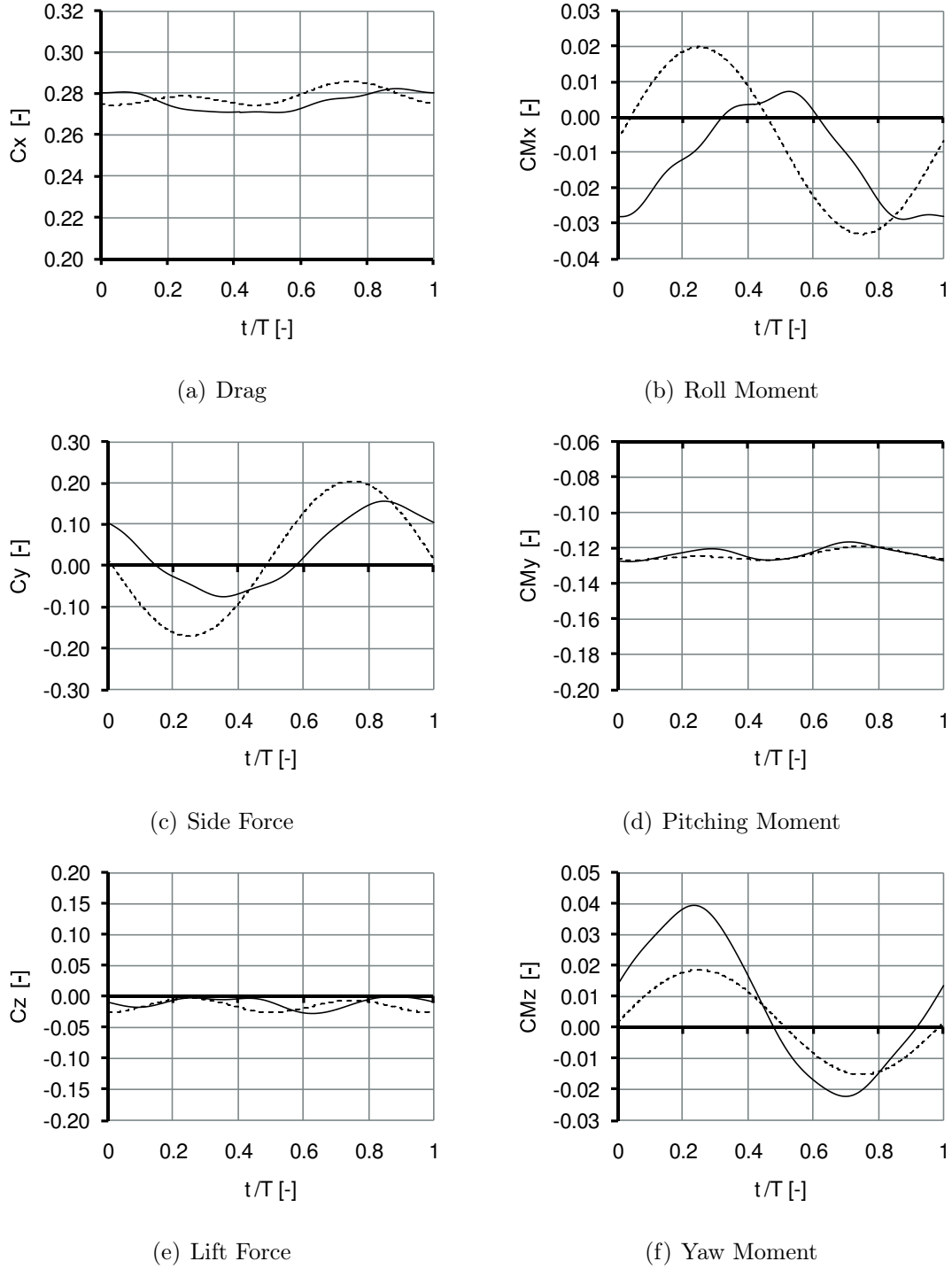
Figure 1.9: Unsteady and quasi-steady evolution of aerodynamic loads at oscillation with $f = 2\,\text{Hz}$ and $\beta = \pm 3.3°$ from experiment as presented by Theissen [107].

1.3.4.3 Unsteady aerodynamic loads during crosswind gusts

Resulting unsteady aerodynamic loads from experimental model oscillation with $f = 2\,\text{Hz}$ and $\beta = \pm3.3°$ are presented in Figure 1.9. Therein, unsteady data are periodically averaged and 11 Hz low pass filtered. Quasi-steady curves are derived from interpolation of steady loads according to the yawing motion. Following the results, drag, lift and pitching moment exhibit only small variations. Instead, significant differences occur for side force, roll moment and yaw moment, which are most relevant in terms of gusty crosswind. Most important, unsteady yaw moment oscillations are amplified and run slightly ahead of the model motion. In contrast, unsteady side force and roll moment oscillations are reduced and delayed. In order to facilitate their analysis, differences between unsteady and quasi-steady loads are summarized in Table 1.1. In comparison to these experimental results, Theissen's numerical results exhibit similar behavior of unsteady and quasi-steady aerodynamic loads, though the setup and geometry differ to some extent.

Table 1.1: Ratio and difference of unsteady (US) and quasi-steady (QS) load amplitudes (half peak-to-peak) as well as time lag of unsteady against quasi-steady load transients from experimental model oscillation with $f = 2\,\text{Hz}$ and $\beta = \pm3.3°$ as presented by Theissen [107].

	C_y	C_{M_x}	C_{M_z}
US / QS	62%	68%	183%
US - QS	-0.072	-0.008	+0.014
$\Delta t/T$	+0.12	+0.22	-0.04

### 1.3.4.4 Proposal of unsteady mechanism

From numerical simulations Theissen found that surface pressures at the front react instantaneously on a distortion of the oncoming flow, whereas surface pressures at the rear of the vehicle are enhanced and react with a time delay. A very important achievement of Theissen was to provide the link between the phenomena at the vehicle rear and a characteristic flow topology at constant $\beta \neq 0$. In agreement to Lemke [70], Gohlke et al. [48,49], Guilmineau and Chometon [50] and Heuler [54], Theissen found a flow region exhibiting high lateral velocity around the leeward rear lights, which characterizes the wake flow field. This fluid entering into the wake region from the leeward side is accompanied by two counter-rotating vortices or at least high positive and negative vorticity, compare Figure 1.10. As previously stated by Guilmineau and Chometon [50], Theissen considers a delayed reaction of the leeward flow to a change of the oncoming flow to be responsible for the delayed and enhanced pressure oscillations at the vehicle rear. Theissen verified that delayed inflow by numerical simulations as well as experimental measurements.

The unsteady mechanism is summarized in Figure ??, where the 2-dimensional flow field is schematically shown for a change from negative to positive yaw. The resulting side force components at the vehicle front and rear are indicated by different arrow sizes. At negative yaw, leeward inflow into the wake region results in a lower static pressure at
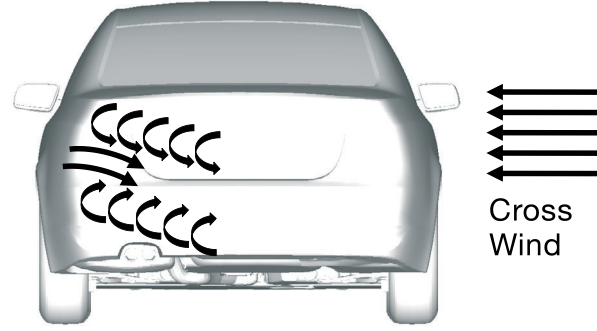
Figure 1.10: Schematic of the leeward wake flow at steady crosswind (from Theissen et al. [108]).

the leeward than at the windward rear corner due to leeward fluid acceleration. Then, for a sudden change of the oncoming flow to positive yaw, the flow at the front adopts instantaneously, while the wake flow initially remains unchanged. This results in even higher velocities and lower pressures on the right rear corner and the inverse at the left rear corner. Hence the static pressure differences at the rear give a side force, which increases the total yaw moment but decreases the total side force. Finally, after a certain time delay, the wake flow adopts and quasi-steady state is reached again.
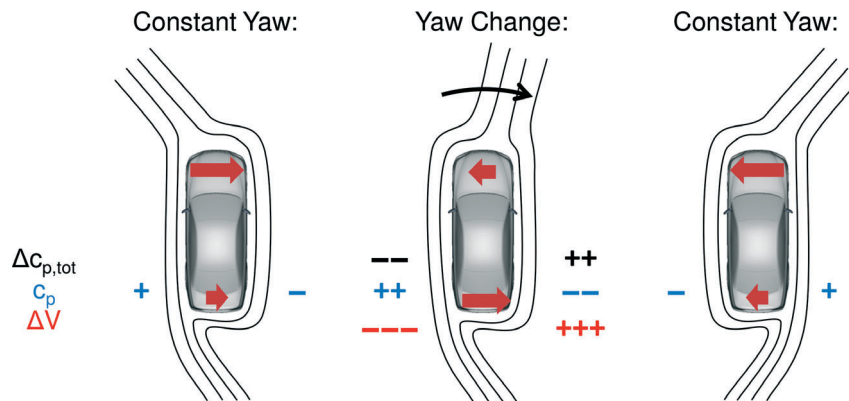

Figure 1.11: Schematic view of 2-dimensional flow field at constant yaw (left and right) and during a gust event (center) from Theissen [107].

Theissen further specified the impact of leeward inflow on unsteady loads based on numerical findings. He showed that the strength of the leeward inflow peaks at approximately 9° yaw. Accordingly, the rear surface pressure distribution is dominated by the wake flow for smaller yaw angles, whereas it is dominated by the oncoming flow for higher yaw angles. So, the unsteady mechanism presented above is most significant in a yaw angle range $-9° \leq \beta \leq +9°$ and unsteady phenomena are drastically reduced beyond. Besides, there is a discontinuity in the integral loads versus yaw angle curve at $\beta = 0°$, since the pressure differences at the rear are suddenly reversed due to a reversed flow topology.

1.3.4.5 Dependency on gust parameters

Having characterized the unsteady physical mechanism, Theissen numerically investigated its dependency on the gust frequency, vehicle speed and on the initial yaw angle. According to his results, the absence of a zero-crossing in the yaw angle change and thus the absence of a change of windward and leeward side significantly reduces unsteady phenomena. This occurs, because surface pressure oscillations on right and left vehicle rear are in that case out of phase, although a delayed reaction of the wake flow still appears.

According to Theissen, the unsteady mechanism is predominantly influenced by the Strouhal number comprising influence of gust frequency and vehicle speed. In contrast, the influence of the Reynolds number is small within $0.63 \cdot 10^7 \leq \text{Re} \leq 1.96 \cdot 10^7$. Figure 1.12 presents the variation of aerodynamic load magnification and time delay for various Strouhal numbers $0.03 \leq \text{Sr} \leq 0.50$. The yaw moment overshoot is largest around $\text{Sr} = 0.16$, whereas the side force and roll moment undershoot are largest around $\text{Sr} = 0.22$ for the BMW notchback geometry investigated. The phase relations are highly Strouhal dependent, as well. Finally, unsteady effects are determined by the amplification of loads at the rear as well as the phase lag between front and rear load contributions.
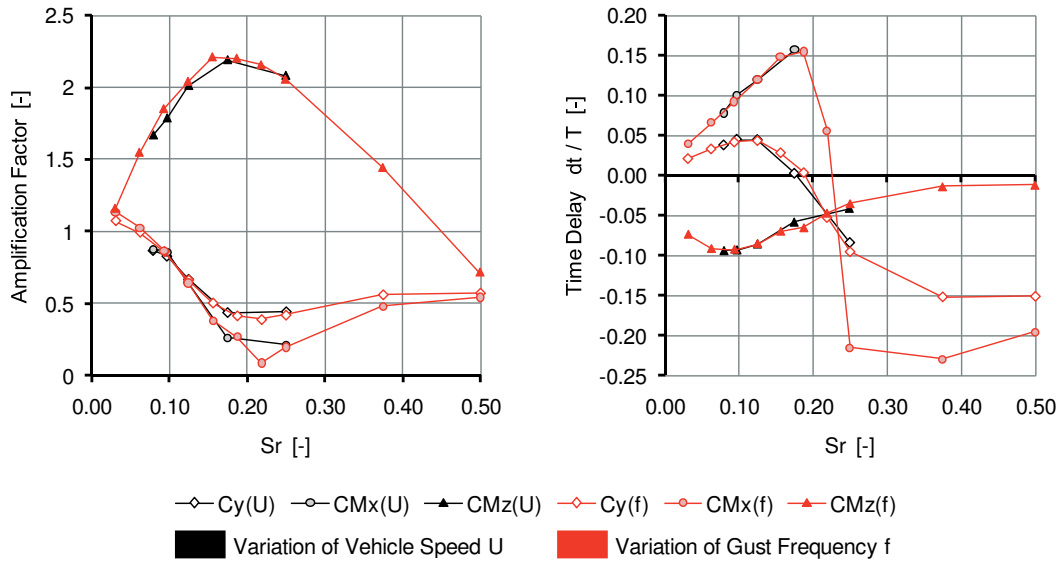
Figure 1.12: Amplification and time delay of side force, roll moment and yaw moment versus Strouhal number from Theissen [107].

In addition, Theissen numerically studied different vehicle types subjected to crosswind gusts. He found that the proposed unsteady mechanism applies similarly to the station wagon, fastback and notchback. However, differences between unsteady and quasi-steady loads were less pronounced for the station wagon geometry than for notchback and fastback. From that Theissen followed that the intensity of unsteady phenomena depends on the strength of the leeward inflow, the time delay of the wake flow and the size of the influenced lateral area.

1.3.4.6 Summary

Summing up, Theissen continued the work of preceding investigations on vehicle aerodynamics during crosswind gusts. He confirmed that the unsteady yaw moment is underestimated and the unsteady side force is overestimated by quasi-steady approximation of loads. It is emphasized that his results apply to realistic Strouhal and Reynolds numbers. As his most valuable achievement, Theissen described decidedly, how a delayed reaction of the wake topology affects unsteady load transients. He also verified this unsteady mechanism by experiments. Moreover, he proved and explained the dependency of unsteady loads on the Strouhal number. However, his results are only qualitative since the numerical simulation tool used for his studies was not validated.

1.4 Objectives

As mentioned in the introduction, the vehicle response to gusty crosswind is a complex and coupled procedure, which involves aerodynamics, vehicle dynamics and the driver's reaction. In order to accurately determine the vehicle response, a reliable prediction of transient aerodynamic loads is indispensable. Since this is preferably done at an early stage of the product development, aerodynamic simulation tools are highly desirable. The overall objective of this work is to assess, how accurate a commercial simulation tool currently established in industry computes unsteady aerodynamic loads during crosswind gusts. To this end, the following issues have to be addressed:

▶ First, profound information on the oncoming flow facing a vehicle during crosswind gusts is missing. It is therefore not possible to deduce the development of flow parameters and turbulence characteristics during gusty wind at heights of approximately 1 m above ground relevant for vehicle aerodynamics. In particular, the profile, the amplitude and the frequency of velocity distortions are unknown. However, this information is obligatory, as it defines the inlet boundary condition of any experimental and numerical investigation on gusty crosswind. An aim of the present work is to record and analyze single crosswind gusts during on-road measurements. Thus, the oncoming flow should be characterized such that the information can be used in future experimental and numerical studies. Besides, it is aimed for a classification into relevant and irrelevant turbulence scales, which should be considered when assessing vehicle stability during crosswind gusts.

▶ It is mentioned previously in this chapter that recent experimental and numerical investigations have assumed different flow conditions during crosswind gusts. As will be shown in the main part of this work, Reynolds and Strouhal numbers as well as velocity amplitudes often differed from realistic values. Hence, those investigations are essentially limited to providing qualitative results. Therefore, a second aim of this work is to acquire experimental data from a wind tunnel experiment, which allows for replicating flow conditions similar to during crosswind gusts on road. The experimental setup was developed in close collaboration with Pascal Theissen and was presented in [107, 111]. Theissen used the results to verify a physical mechanism encountered in numerical simulations. Here, the objective is to substantiate

the relationship proposed by Theissen by a thorough analysis of unsteady pressure measurements. In addition, experimental load transients should be compared for varying oncoming flow conditions and for various vehicle geometries. Thus, a quantitative understanding of on-road aerodynamics, when a crosswind gust is hitting a vehicle, is aimed for.

▶ As a third objective of the present work, the experimental results should be used to assess the capability and accuracy of a numerical simulation tool used in industry. This tool intends to predict transient aerodynamic loads during crosswind gusts, which would facilitate a virtual crosswind gust analysis at an early stage of the product development process.

1.5 Theory

1.5.1 Lattice Boltzmann method and implementation in PowerFLOW®

The theoretical framework of the Lattice Boltzmann method is briefly introduced in the following. A detailed description can be found in the literature, for instance in Hänel [59], Succi [104] and Chen et al. [23]. Here, the focus is within its implementation in the commercial solver PowerFLOW®.

1.5.1.1 Boltzmann equations

The Boltzmann method is based on a mesoscopic description of the molecular dynamics of fluids, where the state of a fluid system is characterized by the evolution of a scalar distribution function $f(\boldsymbol{\xi}, \boldsymbol{x}, t)$. The scalar distribution function defines the number of particles at a time t at the position $\boldsymbol{x}$ with a velocity $\boldsymbol{\xi}$. The transport equations of the distribution function in the 6-dimensional phase space (3-dimensional velocity space and 3-dimensional position space) are

$$\frac{\partial f}{\partial t} + \boldsymbol{\xi}\frac{\partial f}{\partial \boldsymbol{x}} + \frac{\boldsymbol{F}}{m}\frac{\partial f}{\partial \boldsymbol{\xi}} = \left(\frac{\partial f}{\partial t}\right)_{coll} \tag{1.11}$$

with the collision term on the right hand side describing the change of the distribution function due to molecular collisions. Hence, the collision term must obey the basic laws of conservation, such as the conservation of mass and momentum. According to Bhatangar, Gross and Krook (BGK model [15]) the collision term can be replaced by a relaxation of the distribution function to the local equilibrium distribution function f^{eq},

$$\left(\frac{\partial f}{\partial t}\right)_{coll} = \omega_{coll}(f^{eq} - f). \tag{1.12}$$

There, ω_{coll} denotes the collision frequency corresponding to the inverse of the relaxation time scale. The equilibrium distribution is a Maxwell distribution, which does not include

information about molecular transport properties being necessary for the determination of Reynolds stresses and heat transfer. It can be derived for Kn $\to$ 0, where the Knudsen number Kn is defined as

$$\text{Kn} = \frac{\bar{\lambda}}{\text{L}} \tag{1.13}$$

with the mean free path $\bar{\lambda}$ and a characteristic length of the flow problem L. For small Knudsen numbers, i.e. small deviations from thermodynamic equilibrium, a non-equilibrium distribution can be approximated by a Chapman-Enskog developing, compare Chen et al. [23]. Small deviations from thermodynamic equilibrium mean that the collision processes in the fluid are much faster than changes of macroscopic properties. A first order approximation of the non-equilibrium distribution functions can then be segued into the Navier-Stokes equations (compare [59]).

1.5.1.2 Lattice Boltzmann method

The Lattice Boltzmann (LB) Method is based on a discrete formulation of the Boltzmann equation with BGK model

$$f_i(\boldsymbol{x} + \boldsymbol{\xi}_i \delta t, t + \delta t) = f_i(\boldsymbol{x}, t) + \omega_{coll} \delta t (f_i^{eq}(\boldsymbol{x}, t) - f_i(\boldsymbol{x}, t)). \tag{1.14}$$

The discrete particle distribution function f_i defines the number of particles at the location $\boldsymbol{x}$ at a time t. $\boldsymbol{\xi}_i$ denotes the discrete particle velocity in the ith direction, δt the time step, ω_{coll} the collision frequency and $f_i^{eq}(\boldsymbol{x}, t)$ the discrete equilibrium distribution function. The discrete particle distribution is calculated at each node of a spatial grid. In PowerFLOW® 3-dimensional volumes are discredited with a cubic grid with identical node distances in any direction i. The grid is called lattice in many LB methods and the volume elements are called voxel. Particles must stick to the lattice, i.e. they can only move from one node to another node per time step. The LB method is only valid for weakly compressible flows with small Mach and Knudsen numbers and the collision term is approximated with a discrete formulation of the Maxwell distribution. One calculation step consists of two partial steps: A propagation step, where the distribution function is transported in the direction i, and a collision step, where the change of the distribution function is calculated. Having solved the set of i Equations 1.14, the basic macroscopic fluid properties density and momentum are recovered by summation,

$$\rho(\boldsymbol{x}, t) = \sum_i f_i(\boldsymbol{x}, t), \tag{1.15}$$

$$\rho \boldsymbol{u}(\boldsymbol{x}, t) = \sum_i \boldsymbol{\xi} f_i(\boldsymbol{x}, t). \tag{1.16}$$

1.5.1.3 Turbulence model

The Lattice Boltzmann method is generally capable of accurately calculating turbulent flows – given the grid resolution is high enough to resolve the whole range of turbulence scales. Since this usually cannot be satisfied in many industrial applications, a turbulence model that accounts for smaller turbulent structures is implemented in

PowerFLOW®. Turbulent fluctuations are modeled in analogy to eddy viscosity models for Reynolds-averaged Navier-Stokes (RANS) methods. The only turbulence model available in PowerFLOW® is a two equation k-ϵ RNG model. It is implemented by replacing the molecular collision frequency ω_{coll} with a modified formulation of the collision frequency $\omega_{coll,eff}$ derived from a systematic re-normalization group (RNG) procedure [21, 22, 84, 105],

$$\frac{1}{\omega_{coll,eff}} = \frac{1}{\omega_{coll}} + C_\mu \frac{k^2/\varepsilon}{\vartheta(1+\eta^2)^{1/2}},\qquad(1.17)$$

where C_μ is a constant, ϑ is the temperature, k and ε are the turbulent kinetic energy and dissipation rate, respectively. The Parameter

$$\eta = \frac{Sk}{\varepsilon}$$

is a combination of local strain, turbulent kinetic energy and dissipation. This approach is different from the Boussinesq approximation commonly applied in RANS, where k and ε are usually coupled to the momentum equation with a linear relation to the Reynolds stress term. Here, the transport equations for k and ε are

$$\frac{\partial}{\partial t}(\rho k) + \frac{\partial}{\partial x_i}(\rho k u_i) = \frac{\partial}{\partial x_j}\left[\left(\frac{\rho\nu_0}{\sigma_{k_0}} + \frac{\rho\nu_t}{\sigma_{k_t}}\right)\frac{\partial k}{\partial x_j}\right] + \mathcal{P}_k - \rho\varepsilon \qquad(1.18)$$

$$\frac{\partial}{\partial t}(\rho\varepsilon) + \frac{\partial}{\partial x_i}(\rho\varepsilon u_i) = \frac{\partial}{\partial x_j}\left[\left(\frac{\rho\nu_0}{\sigma_{\varepsilon_0}} + \frac{\rho\nu_t}{\sigma_{\varepsilon_t}}\right)\frac{\partial\varepsilon}{\partial x_j}\right] + C_{\varepsilon 1}\frac{\varepsilon}{k}\mathcal{P}_k - \left[C_{\varepsilon 2} + C_\mu\frac{\eta^3(1-\eta/\eta_0)}{1+\beta\eta^3}\right]\rho\frac{\varepsilon^2}{k}$$
$$(1.19)$$

and the eddy viscosity ν_t is

$$\nu_t = C_\mu\frac{k^2}{\varepsilon}.\qquad(1.20)$$

In those equations

$$\mathcal{P}_k = \rho\nu_t S^2$$

is the production of turbulent kinetic energy with the mean rate of strain tensor

$$\langle S_{ij}\rangle = \frac{1}{2}\left(\frac{\partial\langle u_i\rangle}{\partial x_j} + \frac{\partial\langle u_j\rangle}{\partial x_i}\right)\qquad(1.21)$$

and its modulus

$$S = \sqrt{2\langle S_{ij}\rangle\langle S_{ij}\rangle}.\qquad(1.22)$$

The model coefficients are C_μ=0.085, σ_{k_0}=σ_{k_t}=σ_{ε_0}=σ_{ε_t}=0.719, $C_{\varepsilon 1}$=1.42, $C_{\varepsilon 2}$=1.68, η_0=4.38 and β=0.012.

1.5.1.4 Wall model

In order to economize the computationally expensive resolution of the boundary layer, a turbulent wall model is implemented in PowerFLOW®. Instead of forcing the velocity to be exactly zero at the wall, the wall shear stress is calculated in the voxel closest to the wall by assuming that the shear stress in that voxel is equivalent to the wall shear stress

$$\tau_\mathrm{w} = \rho u_\tau^2 = \frac{1}{2}c_f\rho U^2.\qquad(1.23)$$

In Equation 1.23 c_f denotes the friction coefficient and u_τ the friction velocity. The velocity profile in the boundary layer is subdivided into three layers. Using the dimensionless wall-normal distance

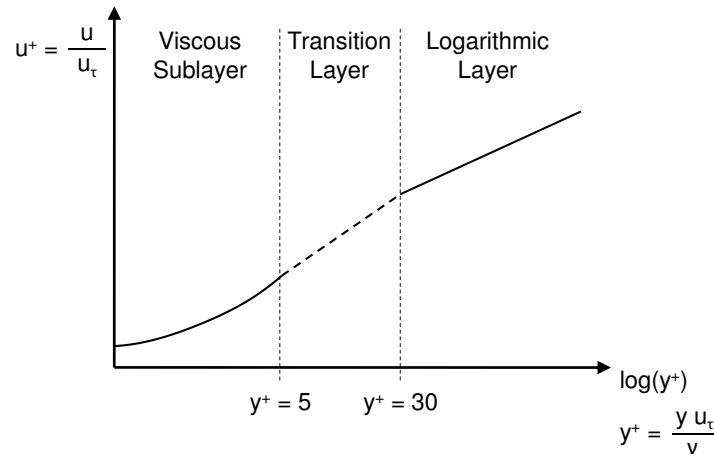$$y^+ = yu_\tau/\nu \tag{1.24}$$

and the dimensionless velocity

$$u^+ = u/u_\tau \tag{1.25}$$

the boundary layer is defined as outlined in Figure 1.13. In the viscous sublayer

$$u^+ = y^+ \tag{1.26}$$

and in the logarithmic layer

$$u^+ = \frac{1}{\kappa}\ln y^+ + B. \tag{1.27}$$

Figure 1.13: Segmentation of the velocity profile in a boundary layer as used by PowerFLOW® (from [107]).

The transition layer connects the viscous sublayer and the logarithmic layer. The constants κ=0.41 and B=5.0 are adjusted so that the velocity profile is continuous. Together with Equation 1.23 these equations facilitate the calculation of the wall shear stress. The influence of a horizontal pressure gradient is accounted for with a scaling factor which adjusts the dimensionless wall distance y^+ according to the streamwise pressure gradient, the density and the turbulent kinetic energy.

1.5.2 Reynolds-averaged Navier-Stokes method and implementation in OpenFOAM®

A different numerical method is introduced, which is based on the Reynolds-averaged Navier-Stokes equations. Here, its implementation in the steady-state solver SimpleFOAM of the open source package OpenFOAM® Version 1.5 dev is of particular interest. Deeper insight into the theory of the method is provided e.g. by Pope [86] and Ferziger et al. [43].

1.5.2.1 RANS method

On a macroscopic level, fluid continua are mathematically described by the Navier-Stokes equations. For incompressible fluid flow without volume forces, the mass and momentum conservation denote as

$$\frac{\partial u_i}{\partial x_i} = 0 \tag{1.28}$$

$$\frac{\partial u_i}{\partial t} + u_j \frac{\partial u_i}{\partial x_j} = -\frac{1}{\rho} \frac{\partial p}{\partial x_i} + \nu \frac{\partial^2 u_i}{\partial x_j{}^2} \tag{1.29}$$

with the velocity u_i and the position x_i in the ith direction, the density ρ, the pressure p and the kinematic viscosity ν. Repeated indexes i and j denote a summation over $i, j = 1, 2, 3$. For turbulent flows, flow quantities ϕ can be divided into the mean flow quantity $\langle \phi \rangle$ and a fluctuating part of the quantity ϕ' by

$$\phi(\boldsymbol{x}, t) = \langle \phi \rangle (\boldsymbol{x}, t) + \phi'(\boldsymbol{x}, t), \tag{1.30}$$

which is known as Reynolds averaging. Applying this to Equations 1.28 and 1.29 gives the Reynolds-averaged Navier-Stokes (RANS) equations

$$\frac{\partial \langle u_i \rangle}{\partial x_i} = 0 \tag{1.31}$$

$$\frac{\partial \langle u_i \rangle}{\partial t} + \langle u_j \rangle \frac{\partial \langle u_i \rangle}{\partial x_j} = -\frac{1}{\rho} \frac{\partial \langle p \rangle}{\partial x_i} + \nu \frac{\partial^2 \langle u_i \rangle}{\partial x_j{}^2} - \frac{\partial \langle u_i' u_j' \rangle}{\partial x_j} \tag{1.32}$$

with the Reynolds stress tensor $-\frac{\partial \langle u_i' u_j' \rangle}{\partial x_j}$. The systems of four equations comprises ten unknowns and is hence not fully determined, commonly denoted as closure problem.

1.5.2.2 Turbulence model

The closure problem of the RANS equations can be dealt with by using eddy-viscosity models, which imply the eddy-viscosity or Boussinesq assumption

$$-\frac{\partial \langle u_i' u_j' \rangle}{\partial x_j} = 2\nu_t \langle S_{ij} \rangle - \frac{2}{3} \delta_{ij} k \tag{1.33}$$

with the Kronecker delta δ_{ij}, the turbulent kinetic energy $k = \frac{1}{2} \langle \boldsymbol{u}' \cdot \boldsymbol{u}' \rangle$ and the mean rate of strain as defined in Equation 1.21. This assumption translates turbulent fluctuations into an additional dissipation ν_t so that the total viscosity $\nu_{eff} = \nu + \nu_t$. Introducing the Boussinesq assumption into the momentum equation gives

$$\frac{\partial \langle u_i \rangle}{\partial t} + \langle u_j \rangle \frac{\partial \langle u_i \rangle}{\partial x_j} = -\frac{1}{\rho} \frac{\partial \langle p_t \rangle}{\partial x_i} + 2 \frac{\partial}{\partial x_j} \left(\nu_{eff} \langle S_{ij} \rangle \right) \tag{1.34}$$

with the modified pressure $p_t = \langle p \rangle + \frac{2}{3} \rho k$. Hence, only the eddy viscosity has to be modeled instead of all six components of the Reynolds stress tensor.

Different eddy-viscosity models are are available in OpenFOAM®, among which a two-equation model is relevant for the present work, namely the realizable k-ε model by Shih et al. [98]. The most distinct difference to other k-ε models is to make C_μ variable and dependent on the mean flow and the turbulence. Thus, positivity of normal stresses and Schwarz inequality for shear stresses are ensured, denoted as "realizability". This allows the model to satisfy certain mathematical constraints consistent with the physics of turbulence, which are violated by the standard or RNG k-ε model.

The transport equations for the turbulent kinetic energy k and the dissipation rate of the turbulent kinetic energy ε are

$$\frac{\partial}{\partial t}(\rho k) + \frac{\partial}{\partial x_j}(\rho k u_j) = \frac{\partial}{\partial x_i}\left[\left(\rho\nu + \frac{\rho\nu_t}{\sigma_k}\right)\frac{\partial k}{\partial x_j}\right] + \mathcal{P}_k + \mathcal{P}_b - \rho\varepsilon - Y_M + S_k \tag{1.35}$$

$$\frac{\partial}{\partial t}(\rho\varepsilon) + \frac{\partial}{\partial x_j}(\rho\varepsilon u_j) = \frac{\partial}{\partial x_j}\left[\left(\rho\nu + \frac{\rho\nu_t}{\sigma_\varepsilon}\right)\frac{\partial\varepsilon}{\partial x_j}\right] + \rho C_1 S\varepsilon - \rho C_2 \frac{\varepsilon^2}{k + \sqrt{\nu\varepsilon}} + C_{1\varepsilon}\frac{\varepsilon}{k}C_{3\varepsilon}\mathcal{P}_b + S_\varepsilon \tag{1.36}$$

where

$$C_1 = max\left(0.43, \frac{\eta}{\eta + 5}\right)$$

$$\eta = \frac{Sk}{\varepsilon}$$

$$S = \sqrt{2\langle S_{ij}\rangle\langle S_{ij}\rangle}.$$

In these equations, $\mathcal{P}_k$ represents the generation of turbulent kinetic energy due to the mean velocity gradients, calculated as

$$\mathcal{P}_k = \rho\nu_t S^2.$$

$\mathcal{P}_b$ is the generation of turbulence kinetic energy due to buoyancy, calculated as

$$\mathcal{P}_b = \beta g_i \frac{\rho\nu_t}{\text{Pr}_t}\frac{\partial\vartheta}{\partial x_i}$$

with the turbulent Prandtl number for energy $\text{Pr}_t = 0.85$, the component of the gravitational vector in the ith direction g_i and the coefficient of thermal expansion β,

$$\beta = -\frac{1}{\rho}\left(\frac{\partial\rho}{\partial\vartheta}\right)_p.$$

Y_M is the dilitation dissipation and is neglected for incompressible flows. C_2, $C_{1\varepsilon}$, σ_k and σ_ε are constants, S_k and S_ε are user-defined source terms.

The transport equation for turbulent kinetic energy is identical to the standard or RNG k-ε model, except for the model constants. In contrast, the transport equation for ε is different, as the production term of ε does not comprise the production of k and as the third term on the right hand side excludes any singularity. The model has been extensively validated in the past and generally performed at least as well as the standard or RNG k-ε model. In particular, enhancements were observed for rotating homogenous shear flows,

free flows including jets and mixing layers, channel and boundary flows and separated flows.

As in other k-ε models, the turbulent viscosity ν_t is then computed as

$$\nu_t = C_\mu \frac{k^2}{\varepsilon} \tag{1.37}$$

with the model parameter C_μ, which is no longer constant as with the standard or RNG k-ε model, but is instead given by

$$C_\mu = \frac{1}{A_0 + A_s \frac{k}{\varepsilon} U^*}$$

with

$$U^* \equiv \sqrt{\langle S_{ij}\rangle \langle S_{ij}\rangle + \tilde{\Omega}_{ij}\tilde{\Omega}_{ij}},$$

$$\tilde{\Omega}_{ij} = \Omega_{ij} - 2\varepsilon_{ijk}\omega_k,$$

$$\Omega_{ij} = \langle \Omega_{ij}\rangle - \varepsilon_{ijk}\omega_k,$$

where $\langle\Omega_{ij}\rangle$ is the mean rate of rotation tensor viewed in a rotating reference frame with the angular velocity ω_k. The model constants are given by

$$A_0 = 4.04, A_s = \sqrt{6}\cos\phi$$

with

$$\phi = \frac{1}{3}\cos^{-1}(\sqrt{6}W), W = \frac{\langle S_{ij}\rangle \langle S_{jk}\rangle \langle S_{ki}\rangle}{\tilde{S}}, \tilde{S} = \sqrt{\langle S_{ij}\rangle \langle S_{ij}\rangle}.$$

So, C_μ is a function of the mean strain and rotation rates, the angular velocity of the system rotation and the turbulence properties k and ε. C_μ recovers the standard value of 0.09 for an inertial sublayer in an equilibrium boundary layer. The model constants are $C_{1\varepsilon} = 1.44$, $C_2 = 1.9$, $\sigma_k = 1.0$ and $\sigma_\varepsilon = 1.2$.

1.5.2.3 Wall model

Since high-Re flows would require a very fine resolution of the boundary layer to achieve accurate results, wall functions are applied in order to limit the computational effort. The near wall velocity profile implemented in OpenFOAM® is based on a division of the boundary layer as shown in Figure 1.13. The relation between y^+ and u^+ corresponds to Equation 1.26 for the viscous sublayer and to Equation 1.27 for the logarithmic layer, however with $\kappa = 0.4187$ and $B = 5.25$. By assuming a balance of turbulent production and dissipation in the logarithmic layer the friction velocity yields

$$u_\tau = C_\mu^{0.25}\sqrt{k} \tag{1.38}$$

and the dimensionless wall distance calculates to

$$y^+ = \frac{C_\mu^{0.25}\sqrt{k}}{\nu}y. \tag{1.39}$$

The production and dissipation of turbulent kinetic energy is then

$$\varepsilon = \frac{C_\mu^{0.75} k^{1.5}}{\kappa y} \tag{1.40}$$

and the turbulent viscosity at the wall is

$$\nu_t = \nu \left(\frac{\kappa y^+}{\ln(E y^+)} - 1 \right) \tag{1.41}$$

with the model constant $E = 9.0$.

1.5.2.4 Implementation in OpenFOAM®

OpenFOAM® uses the Finite Volume Method. Here, it is not aimed for a detailed presentation of that method, which is intensively dealt with in literature (refer to e.g. Ferziger et al. [43]). Instead, information is provided on the numerical settings used in the present work and its implementation in OpenFOAM®.

The numerical domain is discretized using polyhedral cells. Having integrated the governing equations over the single cell volumes, spatial and temporal terms are discretized giving a linear system of equations. Thereby, convective terms are discretized by a first order upwind scheme and diffusive terms are discretized by second order central differencing. Surface-normal gradients are computed using an explicit non-orthogonal correction. RANS and additional equations are solved in segregated way and the solution variables are stored in the cell center.

As there is no independent equation for the pressure within the Navier-Stokes equations, a pressure field is constructed, which fulfills mass conservation, denoted as pressure correction. In OpenFOAM®'s simpleFOAM solver, mass conservation is achieved by the SIMPLE (Semi-Implicit Pressure Linked Equations) algorithm according to Caretto et al. [18]. This algorithm consists of three steps. First, a velocity field is obtained with the pressure from the last step. Second, the pressure correction equation is solved. Third, the obtained pressure is employed to correct the velocity field. This new velocity field fulfills mass conservation. However, a correct pressure field would require repetitions of that loop, which is omitted in the simpleFOAM solver, as time steps are large and non-linear effects are hence more important than to obtain a correct pressure field. Besides, simpleFOAM uses under-relaxation factors according to Jasak [61]. In the present work, the pressure is under-relaxed by a factor of 0.1, whereas the other solution variables are under-relaxed by a factor of 0.3 in order to accelerate convergence. Thereby, an under-relaxation factor close to zero corresponds to a dominance of the old solution.

The equations for $\boldsymbol{u}$, k, ϵ and ω are solved using a Gauss-Seidel smoothed solver. The GAMG (Geometric-Algebraic Multi-Grid) algorithm is applied for the pressure equation. It first solves the equation on a very coarse grid and then step-by-step increases the grid's resolution. By mapping the coarse solution on the fine grid it can achieve good rates of convergence. A diagonal based incomplete Cholesky factorization is chosen for preconditioning.

2 Experimental investigation of on-road flow conditions during crosswind gusts

As mentioned in the introduction, research in the field of unsteady vehicle aerodynamics fundamentally lacks information on the oncoming flow which faces a vehicle. Basically, "the presence of turbulent flow leads to a wide variety of flow conditions that do not occur in the smooth-flow wind tunnel" [27]. Since Cooper realized that "it is [...] impractical to consider them all" [27] and since crosswind gusts are considered most severe regarding driving stability, the objective of the following chapter is limited to the investigation of single gust events. To this end, on-road measurements of the oncoming flow during crosswind gusts are analyzed and presented. Further unsteady scenarios such as interactions with other traffic participants or passing of road-side obstacles are not taken into account.

2.1 Experimental setup

The experiment is based on Wordely's setup [126, 127], compare Figure 1.3, which minimizes the displacement effect of the car on the flow and allows measurements during different traffic situations and driving maneuvers. A combination with vehicle dynamics measurement instrumentation is feasible, as well. Figure 2.1(a) sketches the overall design of the setup, which consists of a test vehicle, a probe holding device, three fluid probes and additional measurement equipment.

(a) Overall Setup   (b) Probe Setup
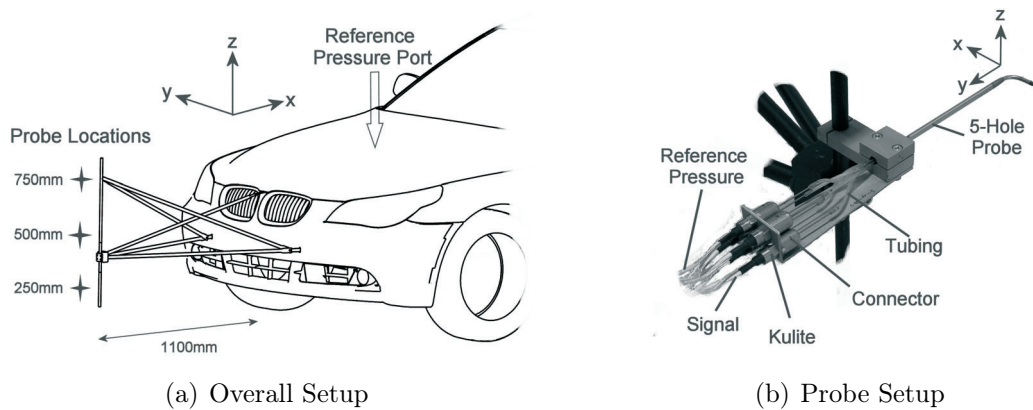
Figure 2.1: Overall setup and fluid probe.

2.1.1 Probe position and probe motion

The probes are positioned 1100 mm in front of the vehicle and 250 mm, 500 mm and 750 mm, respectively, above the ground. If not indicated differently, the results presented in the following refer to the main probe positioned 500 mm above ground, which roughly corresponds to the height of the stagnation point. Positioning of the probes can be assumed to be fully identical for all test runs. The probe location in x-direction meets a compromise between least influence of the vehicle and an acceptable amount of probe motion. Wordley et al. proved that turbulent velocity fluctuations in front of a similarly shaped car remained unaffected until 1.0 m ahead of the front bumper. Furthermore, he showed that the mean velocity measured at 1.0 m ahead of the front bumper only differed fractionally from the undisturbed flow velocity [126].

In order to assess the effect of the probe motion, a tri-axis accelerometer was initially mounted at the front end of the probe holding device, as originally proposed by Wordley et al. [126]. Spectral analysis proved that the energy content of the probe motion in x- and y-direction is at least two orders of magnitude smaller than the energy content of the corresponding wind velocities measured by the probe, which agrees with Wordley's observations [126]. During gust events the low frequency energy content of the probe motion in y-direction can be one order of magnitude higher due to steering action. Since it is intended to measure the total velocity vector within the vehicle fixed coordinate system, which corresponds to the unsteady boundary data to be set in numerical simulations, the steering action is intentionally not accounted for. Regarding the probe motion in vertical direction, the energy spectrum exhibits a peak between 10 Hz and 11 Hz. At average track conditions this peak is two orders of magnitude smaller than the corresponding spectral energy content of the vertical wind velocity component. The highest peak measured at an exceptional bad track was one order of magnitude higher. Hence, the probe motion in vertical direction can be disregarded in the following and measurements can be performed without accelerometer. Besides, it will be shown that the variation of vertical velocity is of minor importance during crosswind gusts.

2.1.2 Fluid probe

2.1.2.1 Probe selection

Since hot wire or hot film probes have the drawback to be very sensitive to particles, robust L-shaped five-hole probes [1] are used for the on-road measurement of the oncoming flow velocity vector in this study. The probes were calibrated by the manufacturer[1] for steady flow conditions and are suitable for a velocity range from 25 m/s to 60 m/s and a yaw angle range of $\pm 55°$. Accuracy is indicated to be better than 1% of the flow speed and $0.5°$ in flow angle.

---

[1]Aeroprobe Corp.

2.1.2.2 In-situ calibration

An in-situ calibration of the probes correcting the influence of the vehicle displacement effect on the measurement location is determined in the Aschheim wind tunnel facility of BMW for wind speeds between 33.3 m/s and 50.0 m/s in a yaw angle range of ±20°. A linear yaw angle and velocity magnitude correction is defined accordingly. Application of the corrections does not reduce the accuracies indicated by the probe manufacturer for isolated usage.

2.1.2.3 Acoustic correction

The five-hole probes are originally not intended for unsteady measurements [1]. This is why fast response multi-hole probes have been designed by some manufacturers embedding pressure transducers in the probe shafts, which increases the frequency response to around 1 kHz. Since fast response probes were not available, the five-hole probes used in this work are adapted in a very similar way. The probes are equipped with five miniature differential pressure transducers directly behind the probe shaft. Kulite XT-190 (M) series transducers with a pressure range of ±6895 Pa are used for that purpose featuring a typical error of ±0.1% full scale output and a maximum error of ±0.5% full scale output for combined non-linearity, hysteresis and repeatability [67]. The steel pipes of the probes are connected with 40 mm flexible tubing to an adapter, where the pressure transducers are screwed into. The full setup is illustrated in Figure 2.1(b).

As there is a non-negligible volume between the tip of the probe and the pressure transducers behind the shaft, damping and phase shifting of the pressure signals have to be accounted for. A transfer function between the pressure oscillation at the probe tip and the pressure transducer signal behind the shaft is measured in the laboratory and later applied for a correction of pressure signals in on-road measurements. This is denoted as acoustic correction and was shown to increase the frequency response of a common multi-hole probe up to maximum 1 kHz, described in detail by Sims-Williams [101, 102].
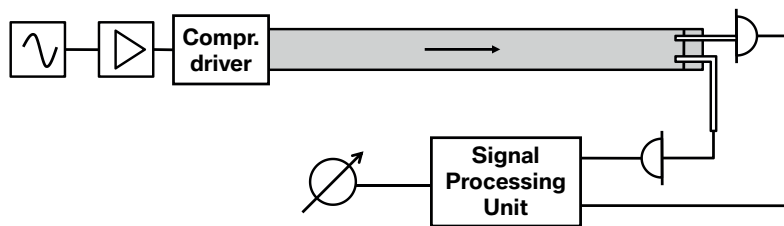
Figure 2.2: Schematic of the experimental setup for the determination of the acoustic correction.

The calibration setup used for the acoustic correction is equal to the one presented by Sims-Williams, but the pressure excitation is generated by a compression driver as proposed by Kameier [62]. The advantage against speakers is the generation of much higher energy densities of the excitation signal. The setup finally used in this work is outlined in Figure 2.2. The compression driver generates pressure oscillations with frequencies between 0 Hz and 1000 Hz propagating through a cylindrical plexiglass pipe. The first mode

of the pressure fluctuations is a plane wave which guarantees to impose the pressure fluctuation simultaneously on a microphone and the tip of the five-hole probe, which are mounted next to each other in the end cap of the cylindrical pipe. The reference microphone [16] exactly records the pressure oscillations as they occur at the probe tip, whereas the pressure transients recorded by the transducers comprise the damped and shifted signals. Thus, the transfer function is calculated for each probe-hole-and-transducer combination. This is exemplified for one combination in Figure 2.3. Using the inverse Fourier transform of the transfer function in data processing during on-road measurements allows to correct for the acoustic damping measured in this calibration process.

(a) Magnitude Ratio

(b) Phase
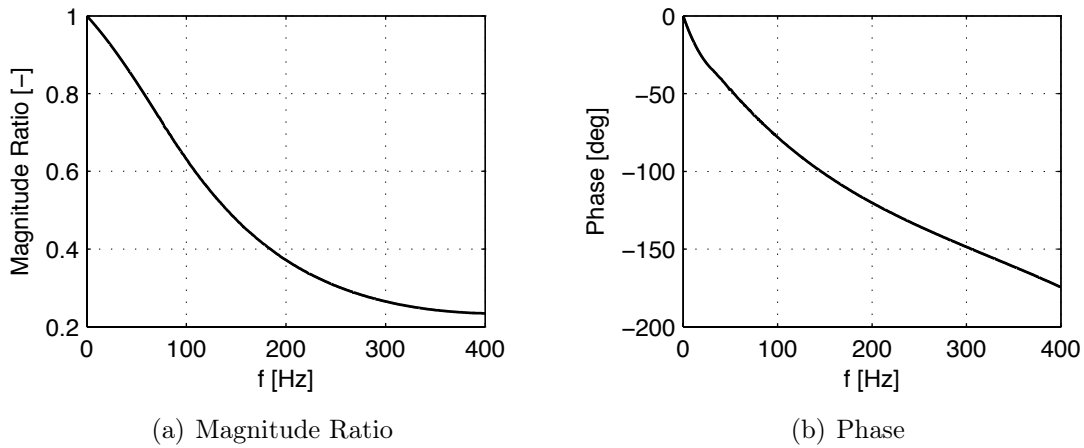
Figure 2.3: Exemplary transfer function for a probe-hole-and-transducer combination.

2.1.2.4 Reference pressure

As opposed to wind tunnel or laboratory experiments, it is much more difficult to acquire a constant reference pressure for the differential pressure transducers during on-road measurements. Here, a pressure tap at $y = 0$ and roughly mid length of the hood is used, as indicted in Figure 2.1(a). In separate wind tunnel tests it was found that the tap features less than 50 Pa difference from atmospheric pressure for any vehicle position within -15° $\leq \beta \leq$ +15°. This is sufficient, since the probe's data reduction algorithm for reducing the five pressure values to velocities and angles is not very sensitive against changes in the reference pressure. Finally, the maximum errors due to inaccurate determination of the reference pressure accumulate to 0.05 m/s and 0.05° for flow velocities and flow angles, respectively.

2.1.3 Signal processing unit

The signal of the pressure transducers is processed in a 24 bit amplifier and analog-digital-converter unit in the vehicle interior powered by an additional measurement battery and controlled by a laptop. The signal processing unit is permanently running during the test runs but only storing into a ring buffer. A measurement is initiated by a hardware

trigger, when a wind gust is noticed by the driver on an absolutely straight highway section without any other vehicles. The trigger is programmed to start the measurement some seconds before the trigger has been activated by taking the latter data of the ring buffer. Thus, single wind gusts can be captured in short time blocks without storing hours of data. Data are logged with a laptop in sets of 16384 samples corresponding to 20.48 s logging time at a sampling frequency of 800 Hz using a 200 Hz low pass Bessel filter for anti-aliasing.

2.1.4 Measurement procedure

The measurements were conducted on highways around Munich (Germany) featuring no speed limit, little traffic and various types of roadside obstacles. In order to base the results on a statistical relevant number of measurements, a total of 163 gust events at Beaufort 4 to 6, locally even 7, were recorded during several days in autumn 2009. The Beaufort scale is based on the empirical formula

$$u_{wind} = 0.836 \cdot B^{3/2} \frac{m}{s},$$ (2.1)

which links the wind speed at 10 m above the surface to the Beaufort scale number B. The Beaufort numbers provided by weather forecasts or meteorologic statistics are 10 min mean values and do not cover single gust peak values, which can be easily twice the 10 min mean value. The Beaufort range chosen is considered as most relevant regarding vehicle dynamics, as the gusts are strong enough to have a fair impact on the driver's safety and comfort but the gusts are not as strong that a driver would intuitively slow down. Atmospheric pressure and temperature is measured by a barometer before and after the test runs and rechecked with meteorologic observations. The vehicle speed is kept constant at 38.9 m/s by the help of a cruise control and steering action is suppressed as much as possible.

2.2 Data processing

First, the raw pressure data are corrected for the signal damping and phase shifting. Then, the corrected pressure data are reduced to velocity and flow angle data using a local least square method implemented by the probe manufacturer [1] and adapted by additionally taking into account the corrections from the in-situ calibration.

For turbulence analysis a certain time block smaller than the measurement time, later called analysis block, is introduced. To obtain the unsteady evolution of turbulence characteristics such as turbulence intensity, length scale and spectral power density, the analysis block is shifted through the data set while the parameters are evaluated within the analysis block.

2.2.1 Turbulence intensity

Turbulence intensity of $i = u, v, w$ is defined as

$$\text{Tu}_i = \frac{\sigma_i}{\overline{u}} \tag{2.2}$$

with the mean velocity in main flow direction $\overline{u}$ and the standard deviation

$$\sigma_i = \sqrt{\frac{1}{N} \cdot \sum_{n=1}^{N} (i_n - \overline{i})^2}, \tag{2.3}$$

where N denotes the number of samples within one analysis block. Due to the objectives of this study the velocity data measured during gusty conditions do not satisfy the requirement of statistical stationarity, i.e. $\overline{i}$ does not remain constant when shifting the analysis block. Hence, calculating the standard deviation by evaluating the difference between the measurement signal i_n and the mean of the signal within the analysis block $\overline{i}$ leads to confusing turbulence intensities. Instead, the difference between the measurement signal i_n and a mean signal has to be evaluated. The mean signal, or in other words the de-trended signal, is found in practice by filtering the raw measurement signal. A 10 Hz low pass filter is used in the following investigation. Thus, the turbulence intensity becomes an estimate for velocity fluctuations above 10 Hz.

2.2.2 Turbulence length scale

Turbulence scales are characteristic temporal or spatial dimensions of the turbulent structures contained in the oncoming flow. It is expected that the scales encountered in gusty wind differ from those at constant wind conditions [89]. Generally, velocity measurements at a single point in space allow for the calculation of characteristic time scales $\mathcal{T}_i$, where $i = u, v, w$. Assuming that Taylor's Hypothesis applies, these time scales can be translated into characteristic length scales ${}^x\mathcal{L}_i$ for the along-wind direction [36]. According to Iyengar et al. [60] there are three different techniques for the estimation of time and length scales:

1. The value of the spectrum at frequency $f = 0$.

2. The area beneath the two-point auto-correlation curve.

3. The location of the spectral peak.

The first technique exhibits significant errors in the determination of sample spectral values at $f = 0$ and is therefore not practicable. The second technique is based on the auto-correlation function

$$ACorr_i(\Delta t) = \frac{1}{\sigma_i^2} \cdot \lim_{T \to \infty} \frac{1}{2T} \int_{-T}^{T} i(t) \cdot i(t + \Delta t) dt, \tag{2.4}$$

where Δt is the time lag, T is the total time period and $i = u, v, w$. The auto-correlation shows spurious periodicity at high lags and has to be truncated at some point (usually the first zero-crossing) for the calculation of the area under the curve. Applying this technique for statistical non-stationary time signals gives incorrect results: the length scales derived strongly depend on the length of the analysis block and do not correlate at all with the velocity transients and power spectra.

The third technique is an empirical attempt of fitting turbulence spectra, such as the von Kármán spectrum, to the dimensionless power spectra measured. In the form presented by Equations 1.9 and 1.10 the curve of $(f \cdot S_i(f)/\sigma_i^2)$ versus $(f \cdot \mathcal{L}_i/\overline{U})$ has a peak, whose position allows for the determination of $\mathcal{L}_i$ for $i = u, v, w$. Details can be found e.g. in [36, 85]. The spectral fitting method generally suffers from errors due to the difficulty in determining accurately the position of the peak [60]. Here, an automatic fitting algorithm is implemented that aligns the empirical curve best possible with the spectrum of each analysis block. The turbulence length scales determined by spectral fitting still depend on the length of the analysis block. However, low frequency peaks in the spectra of the velocity signals, i.e. large turbulent length scales, are much better reproduced as opposed to using the auto-correlation method. An analysis-block length of 4096 samples is chosen for the evaluation of power spectra thus capturing time scales as long as 5.12 s and frequencies as low as 0.2 Hz respectively, which is considered appropriate in the context of vehicle stability in gusty crosswind.

Discrepancies in the evaluation of characteristic length scales with the auto-correlation method on the one hand and with spectral fitting methods on the other hand were also detected by Wordley [126, 127]. In his study the auto-correlation method consistently led to length scales twice as large as derived by fitting to the von Kármán spectrum [126]. Finally, Wordley suggested to use the spectral fitting method. As opposed to this, many other studies applied the auto-correlation method avoiding the effort of implementing automatic spectrum fittings (e.g. [71, 95]).

2.3 Results and discussion

2.3.1 Exemplary gust event

An example for a wind gust event is presented in Figure 2.4, where the time dependent behavior of the velocity components u, v and w is plotted for a section of one measurement set. The results for turbulence intensity and turbulence length scale of v are added as well. The gust event is marked with a dashed rectangle.

The gust is clearly visible as a strong, low frequency distortion in u and v. Depending on the gust direction, such a distinct distortion is visible in any of the 163 gust measurements either in u or in v or - as in 85% of the measurements - in both u and v. With respect to vehicle dynamics lateral velocity distortions are most relevant [91, 119, 120], whereupon a change in velocity of at least 2 m/s with a frequency between 0.2 Hz and 10 Hz is regarded as significant in the following. An impact on the vertical velocity component w was not

observed throughout all measurements (compare Figure 2.4). Hence, a description of w is omitted in many parts of the subsequent crosswind gust analysis.
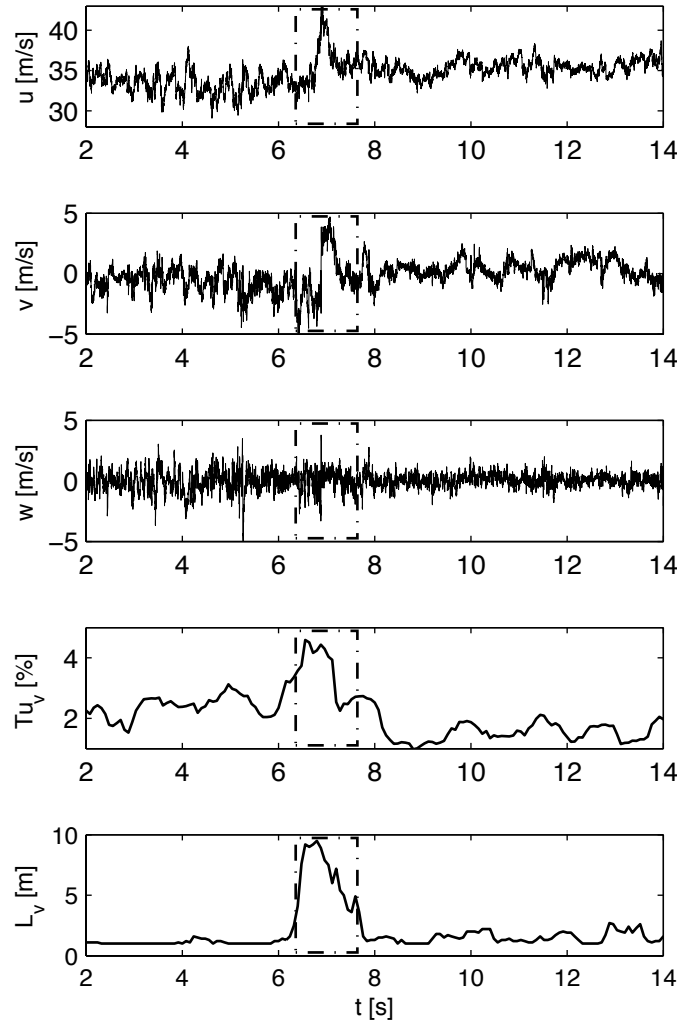
Figure 2.4: Measurement section with a gust event marked by a dashed rectangle.
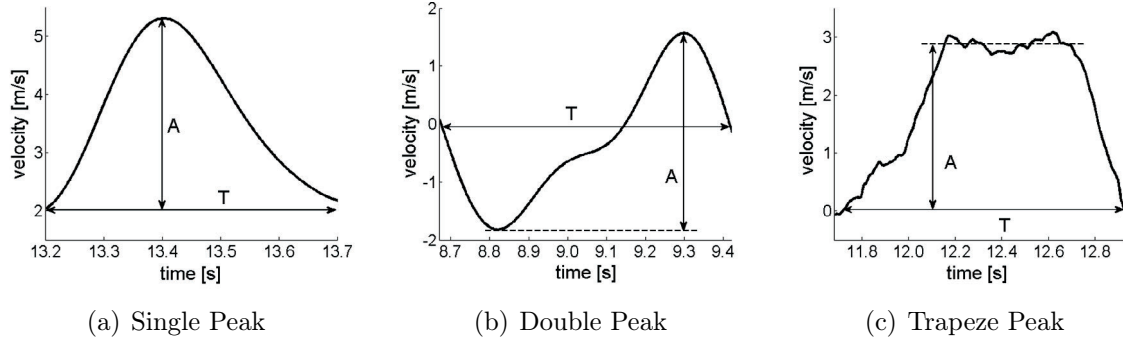
2.3.2 Gust profile

At first, the profiles of the gust peaks in u and v are investigated as they are of great interest for numerical and experimental modeling. Applying a low pass filter (6 Hz) or a moving average filter (length 0.1625 s) they can be classified into the categories *single peak*, *double peak*, i.e. two consecutive peaks with opposite directions, and *trapeze shaped peak*. Gust examples for each category are outlined in Figure 2.5.

The probability of occurrence of the three gust profiles is shown in Table 2.1. According to the results, the majority of the gusts captured are single peak gusts, the trapezoidal gusts count for almost every third gust and the number of double-peak gusts is almost negligible. So, modeling crosswind gusts as single peak gusts is most realistic, which has been intuitively assumed in many previous studies.

Table 2.1: Probability of occurrence of gust profiles.

Single Peak	Double Peak	Trapeze Peak
63%	9%	28%

According to the gust profiles presented in Figure 2.5(a), a sinusoidal change of yaw, which was for instance assumed by Demuth et al. [32], Theissen [107] or Schröck et al. [96], is fairly realistic in order to approximate single peak gusts. Trapeze gusts, as implemented for example by Favre et al. [38,39] or Tsubokura et al. [116], are less common, but realistic, as well.

| (a) Single Peak | (b) Double Peak | (c) Trapeze Peak |

Figure 2.5: Examples for different categories of gust profiles.

According to Theissen [107], the absence of a zero-crossing in a yaw angle change and, thus, the absence of a change of windward and leeward side significantly reduces unsteady phenomena. This is associated with a discontinuity in the integral loads versus yaw angle curve at $\beta = 0°$. Therefore, it is essential to know, how many gusts exhibit a change of sign in their yaw angle transient. According to the results, three gusts out of four statistically exhibit a zero crossing in their v evolution, see Table 2.2. As a consequence, reduced unsteady phenomena due to the absence of a yaw angle change are seldom on-road. In other words, a change of windward and leeward side must be taken into account when optimizing the crosswind sensitivity of a vehicle.

Table 2.2: Probability of occurrence of zero crossing of v.

Zero crossing	No zero crossing
72%	28%

2.3.3 Gust amplitude

The gust amplitude, as indicated with the letter "A" in Figure 2.5, is a decisive gust parameter, since it determines the general flow characteristics at the vehicle rear. As shown by Theissen [107], the rear surface pressure distribution is dominated by the wake flow for smaller yaw angles, whereas it is dominated by the oncoming flow for higher yaw angles. As a consequence, the appearance of unsteady phenomena strongly depends on the yaw angle amplitude of the oncoming flow.

Figure 2.6 summarizes the velocity and yaw angle amplitudes measured during the total of 163 gusts. By definition of the measurement procedure, these results are only valid for the investigated Beaufort number range. According to Figure 2.6, the velocity amplitudes vary between $1\,\mathrm{m/s}$ and $8\,\mathrm{m/s}$, whereas the majority lies in the range of $3\,\mathrm{m/s}$ to $5\,\mathrm{m/s}$. For a vehicle speed of $140\,\mathrm{km/h}$ this translates into a yaw angle change of $1°$ to $13°$ with the majority between $5°$ and $9°$. Note that an amplitude of $8°$ denotes for instance a change from $\beta = +4°$ to $\beta = -4°$ and back to $\beta = +4°$. It is also mentioned that for higher vehicle speeds, the corresponding yaw angle changes become smaller.
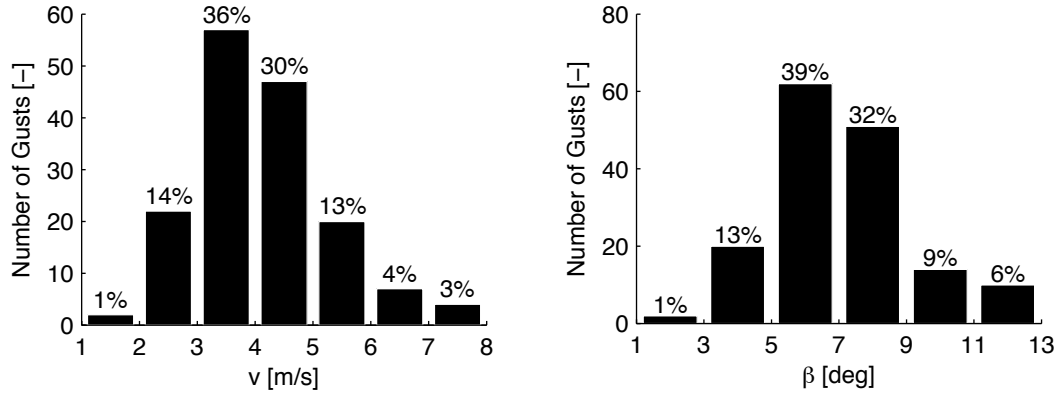
Figure 2.6: Histograms of v- and β-amplitudes at $U_{veh} = 140\,\mathrm{km/h}$.

From Figure 2.6 it has to be concluded that a yaw angle of $30°$, as for instance studied by Favre et al. [38] or Tsubokura et al. [116], is unrealistic. According to Theissen [107], such high yaw angles result in fully detached flow at the leeward side which alters the differences between unsteady and quasi-steady loads. Interestingly, Theissen's numerical investigations on gust amplitudes gave largest unsteady phenomena for gust amplitudes similar to the most frequent amplitudes in Figure 2.6. Higher velocity amplitudes than measured in this study may occur during even extremer weather conditions, where the driver presumably slows down intuitively.

2.3.4 Turbulence intensity

It is observed that a gust, i.e. a peak in the u or v transients, always coincides with a peak in turbulence intensity of the corresponding velocity component. This is exemplified in Figure 2.4 for Tu_v and holds generally true for all gusts. For the case of a double peak gust profile, two positive peaks in the turbulence intensity establish. However, Tu_w remains constant throughout the gust event.

Before and after the gust, i.e. during steady wind conditions, Tu_u, Tu_v and Tu_w are around $1\text{--}3\%$ (more detailed in [127]). The maximum peak value for Tu_u and Tu_v observed during gusts is around 7%, but in average the peak value is around 4%. The maximum turbulence intensity increase during a gust (denoted amplitude) is around 5%, the average increase is 2%. This is summarized in Table 2.3.

Table 2.3: Peak values and amplitudes of Tu_u and Tu_v during gusts.

	Peak value	Amplitude
Average	4%	2%
Maximum	7%	5%

It is often impossible to dynamically change small scale turbulence in experimental or numerical simulations of crosswind gusts. The turbulence intensity is usually set to constant values below 1%. However, Wordley et al. already proved that turbulence levels are higher on-road [126, 127]. Still, when assessing crosswind gusts, accurate modeling of small scale turbulence is certainly less significant as opposed to an accurate replication of the largest scales which contain most energy.

2.3.5 Gust frequency

The turbulence length scales obtained by spectral fitting considerably increase during a gust event. Figure 2.4 illustrates this behavior exemplarily for $\mathcal{L}_v$. However, these results are only qualitative due to deficiencies of the evaluation method, as discussed above. Since there is special interest in the largest time scales in the oncoming flow in order to set correct boundary conditions in future simulations, it is appropriate to approximate these scales by reading out the gust periods T as indicated in Figure 2.5. Any statements regarding time scales in this context are only valid for a vehicle speed of $U_{veh} = 140\,\text{km/h} = 38.9\,\text{m/s}$. The gust frequency shall be defined as the inverse of the gust period T and is presented in Figure 2.7. Following from this, the frequency of the aerodynamic excitation during a gust is between 0.5 Hz and 4 Hz, mostly between 1 Hz and 2 Hz. This implies that the largest length scales observed during gust events are in the order of 80 m. Most often the largest turbulence length scales are around 20–40 m.
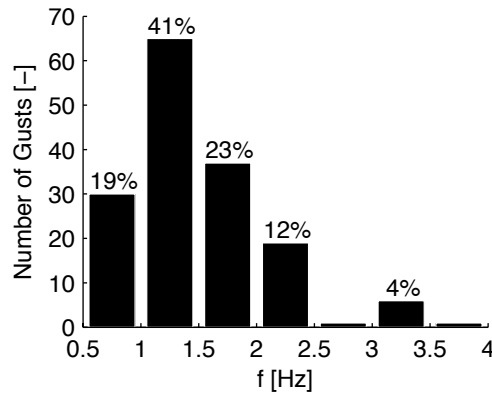
Figure 2.7: Gust frequencies.

According to these results, the major part of the excitation frequencies are within the range of typical eigenfrequencies of the vehicle dynamics of a mid-size passenger car. This is even true for vehicle speeds above 140 km/h, where the length scales translate

into higher excitation frequencies. In addition to that, the excitation frequencies coincide with the range of 0.5 Hz to 2 Hz, where the driver amplifies the vehicle motion (compare Schaible [91] and Wagner [119]). These facts underline the importance of assessing natural crosswind excitation and its impact on vehicle dynamics.

2.3.6 Spectral energy distribution
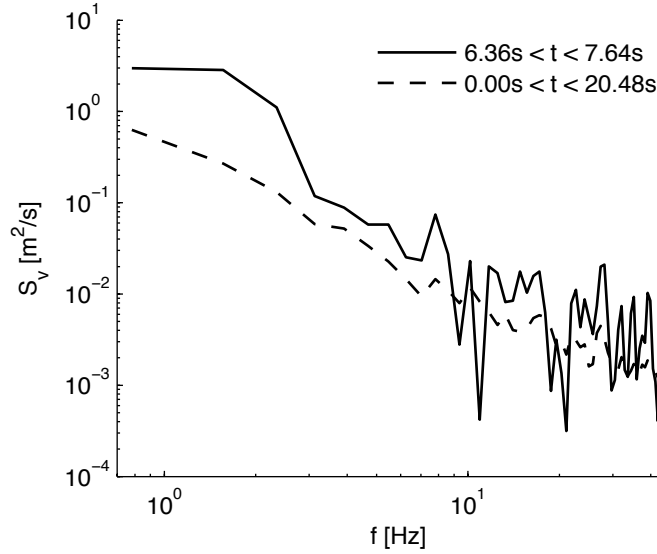
Figure 2.8: Power spectra of v as presented in Figure 2.4 for the whole measurement block (dashed line) and for the time of the gust event (solid line).

In order to summarize the development of turbulence characteristics during a gust event, the spectral energy distribution of the lateral velocity transient from Figure 2.4 is analyzed. In Figure 2.8 the power density of v calculated from the whole measurement set (20.48 s length) is opposed to the power density from a short time window covering the gust event (marked by a rectangle in Figure 2.4). While the slightly larger turbulence intensity mainly increases the entire energy level during the gust, the increased length scale shifts the roll-off position of the curve so that there is more energy contained in the low frequency range. From Figure 2.8, it is very obvious that energy spectra of the oncoming flow are significantly altered during gust events. Since large scales contain most energy, they must be replicated by numerical and experimental models in the first place. It is of secondary importance to correctly simulate small scale turbulence when assessing vehicle stability during gusty crosswind.

2.3.7 Boundary layer profile

In addition to the main probe at 500 mm above ground two more probes were mounted at 250 mm and 750 mm in order to study the boundary layer profile developing in case of a wind gust. It is known that the atmospheric boundary layer, being up to 1000 m thick in total, consists of a laminar sublayer which covers not more than a few millimeters,

followed by a turbulent boundary layer or Prandtl layer which is characterized by the turbulent exchange of momentum, and the upper layer or Ekman layer where the Coriolis forces become more important for the exchange of momentum [85]. For numerical and experimental modeling of vehicle aerodynamics it is essential to know how the velocity profile is shaped in a height up to 1.5 m above ground. This information is still missing [38], as available meteorological boundary layer profiles do not resolve this region accurately.
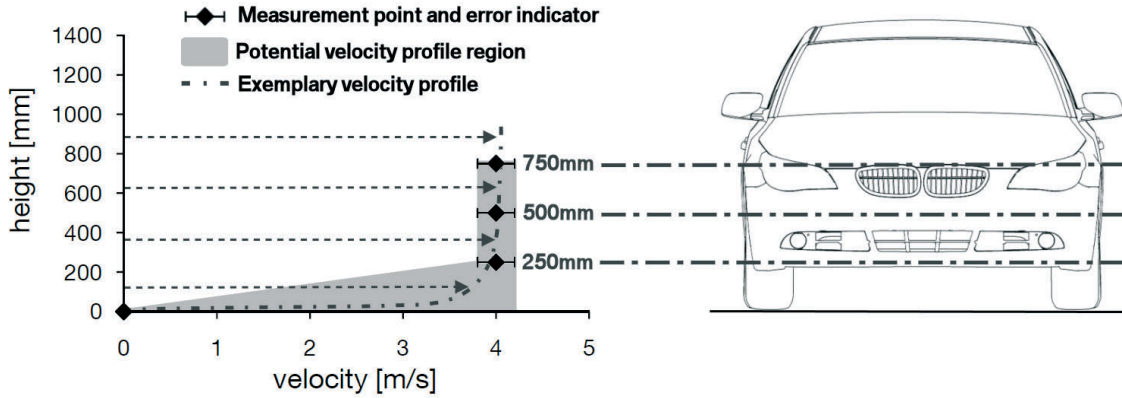
Figure 2.9: Exemplary velocity profile in the boundary layer for a gust amplitude of $v = 4\,\text{m/s}$.

According to the measurements, transient peaks in u and v are recorded likewise by the three probes: frequency and shape of the distortions are identical. The velocity peaks encountered at the three different heights are in a range of $\pm 0.2\,\text{m/s}$ in average and in a range of $\pm 0.4\,\text{m/s}$ maximum, which is only slightly more than the probe's inaccuracy. Regarding turbulence intensity, the values encountered at these different heights are within a range of 0.3% in average and 0.5% maximum for both cases with and without gust. In addition, the highest turbulent intensities are not consistently measured at a single height, which agrees with the findings of Wordley et al., who reported turbulence intensities Tu_u and Tu_v to be constant at 250 mm, 500 mm, 750 mm and 1000 mm above ground in stationary wind conditions [127].

In consequence, the velocity profile developing between 250 mm and 750 mm above ground, which covers a large part of a passenger vehicle body, can be assumed constant. Herewith, the assumption of highly skewed boundary layer profiles from e.g. Cairns [17] and Baker [4,5] is disproved. According to the experimental results, a certain, but unknown velocity profile establishes below 250 mm satisfying the requirement that the velocity is zero at ground and has a value between 1 m/s and 8 m/s (according to Figure 2.6) at 250 mm. This is sketched for an exemplary gust amplitude of 4 m/s in Figure 2.9. Therein, the potential region of the velocity profile is marked and an exemplary velocity profile is plotted. A further investigation of the boundary layer below 250 mm is beyond the scope of this study.

2.4 Conclusions

A gust is a turbulent structure which is transported in main wind direction, creating a three-dimensional, highly fluctuating velocity field. It contains eddies of various sizes and

various frequencies, where the maximum scales are limited by the spatial dimension of the gust and the minimum scales are determined by the viscous forces. So, numerical and experimental methods modeling a gust as a velocity distortion traveling through a numerical domain (e.g. using time-varying inlet boundary conditions or oscillating flaps) are more realistic than methods that impose the velocity distortion in the entire numerical domain at the same time. For small yaw angle changes, however, the differences between both simulation methods diminish and the principal unsteady mechanism is identical, as shown by Theissen and the author [111].

As a consequence of the on-road measurements presented, a gust should be modeled as a single peak or trapezoidal distortion in both axial and lateral velocity. The maximum variation measured for these velocities is 8 m/s. Crosswind facilities used in industry do not replicate realistic flow conditions during gusty crosswind, since the yaw angles modeled are generally around 30°. The amplitude of the velocity distortion has also been overestimated in many numerical and experimental investigations. According to Theissen, the flow characteristics are then significantly altered and the unsteady effects are weakened [107].

Variations of axial velocity are seldomly replicated in numerical and experimental simulations. Building on results of vehicle dynamics investigations on crosswind gusts, head- or tailwind excitation must not be regarded as major concern. So, this simplification of the oncoming flow is presumably acceptable. Besides, a change of sign is recorded for three out of four yaw angle transients. This fact might have been underestimated by many studies, since Theissen recently indicated the relevance of considering this when aiming for largest unsteady effects [107].

It is known from previous investigations that there is a limited range of turbulence scales, which are relevant when assessing crosswind gusts. This range is on the one hand determined by their occurrence in natural, gusty wind. On the other hand its relevance is coupled to the sensitive frequency range of the driver and the vehicle system. In 1983, Bearman and Morel already suggested a "classification into

1. large scale turbulences that can be considered to have quasi-static effects,

2. turbulence with scales approximately equal to the size of the vehicle interacting directly with the flow field and

3. small-scale turbulence which influences boundary layers on the vehicle and which may change separation points" [9].

A similar classification was presented by Sims-Williams [99]. Although it is known that the driver amplifies the vehicle motion between 0.5 Hz and 2 Hz [91, 119] and that the vehicle suspension system is most sensitive in the low frequency range around 1.5 Hz, the occurrence of gust frequencies was unknown until now. Therefore, the limits between the three ranges could not be quantified. The present study overcomes this deficiency, as it is possible to deduce the second range of scales mentioned above from the results presented. Given the vehicle speed of 38.9 m/s and the frequencies from Figure 2.7, the spatial dimension of scales found on-road are between 10 m and 80 m. Larger scales can be analyzed quasi steady, smaller scales carry less energy and are thus less relevant. This

classification of time and length scales is summarized in Figure 2.10 which originates from a joint publication of Theissen and the author [111].
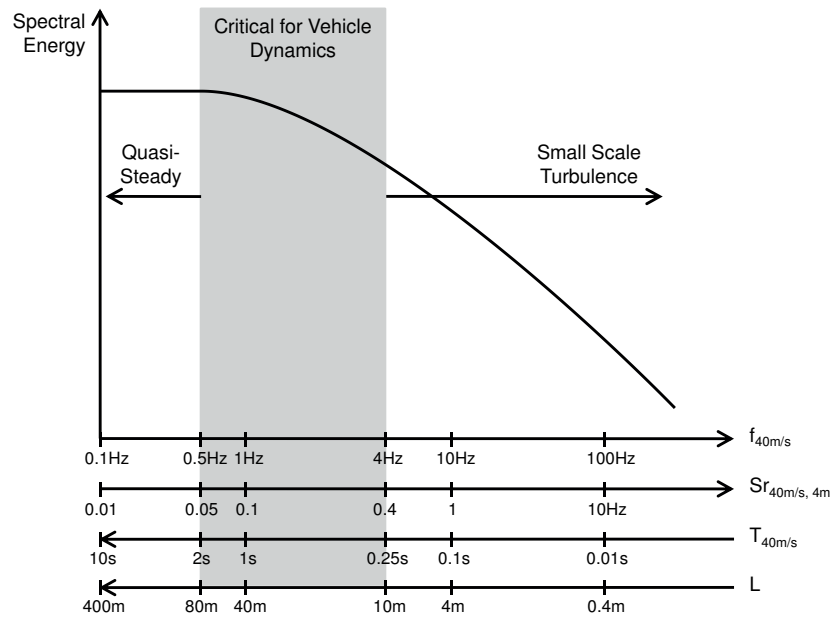
Figure 2.10: Range of relevant scales of crosswind gusts for vehicle aerodynamics.

These limits might be adopted in future unsteady aerodynamic crosswind investigations. Note that it is not known in advance which scales have the most severe impact on driving dynamics of a vehicle. Depending on its geometry, its dimensions and on its suspension system, the critical scales may vary and not be necessarily the largest ones. Therefore, the whole range should be considered when investigating the crosswind sensitivity of a vehicle.

3 Experimental investigation of unsteady aerodynamics under time-dependent flow conditions

This chapter deals with wind tunnel investigations of unsteady vehicle aerodynamics and builds on the boundary conditions worked out in the preceding chapter. An appropriate setup was jointly developed by Theissen and the author and already presented in chapter 1.3.4. In order to understand the results, the experimental setup is briefly summarized. A detailed description of the setup was already given by Theissen et al. [107, 111]. Information on surface pressure measurements are appended, which are not contained in the reference.

3.1 Experimental setup

3.1.1 Model

A slightly simplified but realistic passenger car geometry is used as vehicle model. Unsteady flow phenomena during crosswind gusts were found to strongly depend on the vehicle geometry [108], which requires a replication of realistic geometry details. The DrivAer notchback geometry fulfills these requirements, as illustrated in Figure 3.1.

Detailed information on the DrivAer model can be found in Heft et al. [51]. The DrivAer concept additionally offers a fastback and station wagon variant, which comprise a different rear module, but share the front and underfloor modules with the notchback. The two variants are illustrated in Figure 3.2, where the parting line of the rear module is indicated, as well. The default geometry in this work is, however, the notchback geometry. The model is completely closed, i.e. does not feature flow through the engine compartment. The model built up for the experiments is a 1:2 scale model, whose exact geometrical dimensions are as summarized in Table 3.1.

Table 3.1: Geometric data of DrivAer notchback in scale 1:2.

L_{veh}	H_{veh}	L_{wb}	A_x	A_y
$2.308\,\mathrm{m}$	$0.705\,\mathrm{m}$	$1.393\,\mathrm{m}$	$0.542\,\mathrm{m}^2$	$1.184\,\mathrm{m}^2$
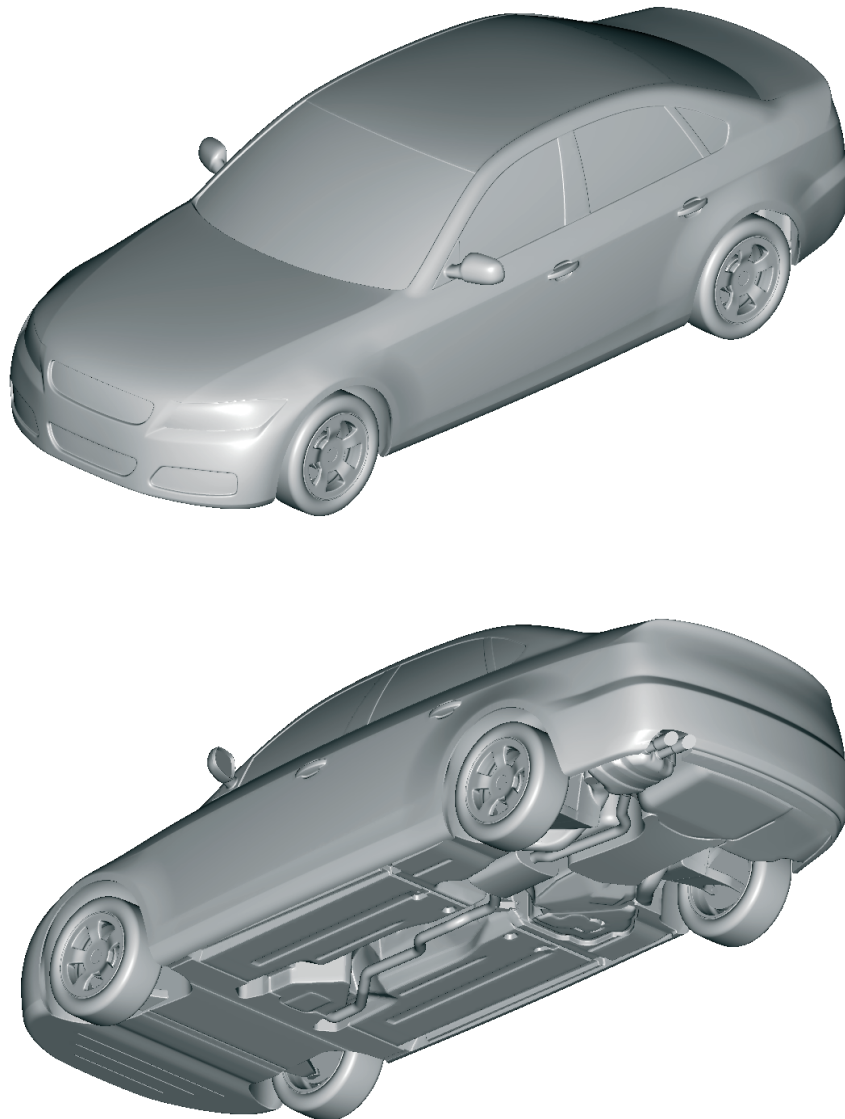
Figure 3.1: DrivAer notchback geometry.

3.1.2 Test facility

The test arrangement is set up in BMW's Aerolab wind tunnel facility. This is a closed-loop wind tunnel with a nozzle cross section of $14\,\mathrm{m}^2$ and an open test section exhibiting dimensions of $20\,\mathrm{m}$ x $14\,\mathrm{m}$ x $11\,\mathrm{m}$. The wind tunnel is equipped with a boundary layer scoop in the nozzle as well as an air suction and tangential blowing slot right in front of the single moving belt of $9\,\mathrm{m}$ length and $3.5\,\mathrm{m}$ width. More details about the facility can be found in [35]. Here, the speed of the moving belt is set equal to the wind speed. All boundary layer control settings were optimized to avoid boundary layer development until the flow reaches the test model. The vehicle model is mounted on a strut, which is connected to a hexapod, an hydraulic device to move the model and strut. The strut is a sting with its cross-section being shaped as a symmetric airfoil. Due to some cables fixed to the outside of the strut and a handmade cover around these cables, the strut profile

used in the experiments is slightly asymmetric. The experimental setup is sketched in Figure 1.8 and the strut is outlined in Figure 4.1.

3.1.3 Model motion

Time dependent oncoming flow conditions are generated by oscillating the vehicle model around its vertical axis, while it is exposed to constant oncoming flow. The vertical axis of rotation is at $x = 0.761\,\mathrm{m}$ and $y = 0\,\mathrm{m}$. The standard model motion investigated is a symmetric sinusoidal oscillation at $2\,\mathrm{Hz}$ frequency with $\pm 3.3°$ amplitude around zero yaw. The maximum deviation of the real model motion from the prescribed hexapod motion is only $0.2°$ for rotational and $4\,\mathrm{mm}$ for translational positioning. Since the moving belt is not capable of such fast oscillations, the model is lifted so that there is a gap between wheels and moving belt of $30\,\mathrm{mm}$. The wheels are fixed to the model and do not rotate. The moving belt is fixed at $\beta = 0°$ and the default wind speed is $58.3\,\mathrm{m/s}$. The corresponding Reynolds and Strouhal numbers during standard model oscillation are $\mathrm{Re} = 8.9 \cdot 10^6$ and $\mathrm{Sr} = 0.08$, based on the model length, the wind speed and the oscillation frequency. Additional test runs are performed at constant yaw positions $\beta = \pm 3.3°$ for a later comparison of unsteady with quasi-steady results. In this case, the model is also lifted and the moving belt is fixed at $\beta = 0°$.

3.1.4 Load measurements

The statement of Garry and Cooper that this "experimental technique is limited by the need to isolate inertial forces from total loads" [46] is addressed by a sophisticated approach using several acceleration sensors in addition to the model balance (see Figure 1.8). The setup is calibrated during model oscillation without wind. In this configuration a transfer function of acceleration to load signals is determined. Afterwards, the model is oscillated in constant flow and the unsteady loads are determined by subtracting inertial loads from the sum of inertial and aerodynamic loads as measured by the 6-component balance, which is mounted between the model and the strut. By averaging over more than 400 oscillations the accuracy is considerably increased such that maximum errors of aerodynamic loads are only $\Delta F_i = 1.6\,\mathrm{N}$ and $\Delta M_i = 0.7\,\mathrm{Nm}$ for $i = x, y, z$.

3.1.5 Surface pressure measurements

Locations   Pressure measurements are taken at a total of 96 positions distributed over the vehicle surface, as indicated in Figure 3.2. Surface pressures are measured at the co-driver side, i.e. on the right side of the model, only. The most relevant measurement positions for this work cover a square at the rear side of the vehicle. Other important pressure measurements are those at the a-pillar, the c-pillar, the front and side as well as along a z-slice from front to rear stagnation point at $z = 65mm$. These groups are indicated separately in Figure 3.2, where the parting line between the three rear modules is marked, as well. As opposed to the notchback model, all pressure tappings located

on the rear module are not recorded during measurements with the station wagon and fastback rear geometry. Hence their rear side measurement square reduces to the lower five by five pressure tappings and the tappings at the c-pillar are completely omitted.

(a) Notchback

(b) Fastback
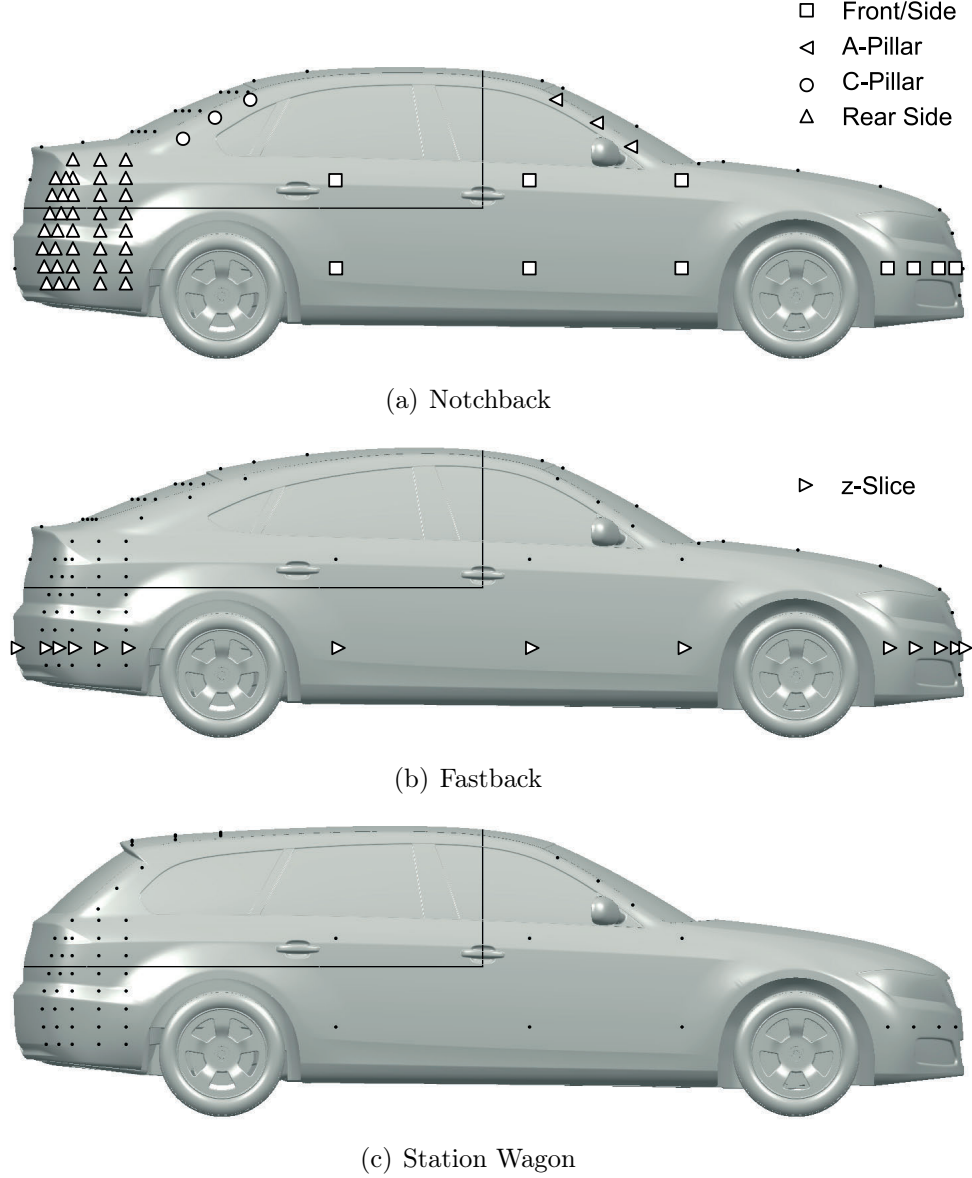
(c) Station Wagon

Figure 3.2: Notchback, fastback and station wagon geometries of DrivAer model with positions of surface pressure tappings.

Sensors   Miniature differential pressure transducers (Kulite XT-190 (M)) with a pressure range of $\pm6985\,$Pa are mounted inside the vehicle model featuring a typical error of $\pm0.1\%$ full scale output and a maximum error of $\pm0.5\%$ full scale output for combined non-linearity, hysteresis and repeatability [67]. They are screwed into a connector and linked with 40 mm flexible tubing to 20 mm long steel pipes (0.4 mm inner diameter), which are finally mounted as pressure tappings in the laminate surface. The frequency response of this setup is high enough to guarantee negligible signal damping and phase shifting for frequencies up to 15 Hz.

3.1.6 Data processing

At constant yaw, all measurement data acquired are averaged over 120 s. During model oscillation, measurement data are phase averaged over as many periods as recorded in 220 s. Forces and moments are non-dimensionalized according to Equation 1.6 and Equation 1.7 using the velocity in the undisturbed free flow at model position as reference velocity. Surface pressures are non-dimensionalized according to Equation 1.4 using the static plenum pressure measured at the test section wall aside the nozzle at $x = $ -4.3 m, $y = $ -3.1 m and $z = 1.5$ m as reference pressure. All measurement data are 11 Hz low-pass filtered. An oscillation period of phase-averaged measurement data is defined such that the positive yaw angle peak is at a quarter and the minimum yaw angle peak at three quarters of the full oscillation period, which is illustrated in Figure 3.3 for the standard test case. Quasi-steady surface pressure transients are derived by interpolating between minimum and maximum steady surface pressures according to the change of yaw angle.
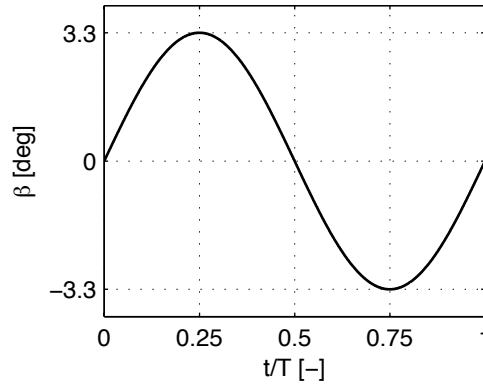
Figure 3.3: Definition of phase-averaged oscillation period.

3.2 Results and discussion

Using the setup presented above, Theissen found that the unsteady yaw moment exceeds the yaw moment in steady flow conditions, whereas the unsteady side force did not reach steady values [107], compare Figure 1.9. Eventually, Theissen proposed that a time delay of the wake flow relative to a change of the oncoming flow causes the differences between unsteady and quasi-steady loads.

The present work is inevitably associated with the setup and results presented by Theissen, since experiments were conducted together. Here, the focus is within the substantiation of the unsteady mechanism proposed by Theissen [107], which explains the differences between unsteady and quasi-steady loads. Therefore, surface pressure measurements at various positions around the vehicle are evaluated. In addition, this work aims to experimentally investigate unsteady aerodynamic loads at various oscillation amplitudes and frequencies as well as at varying wind speeds. Therewith, the dependency of unsteady phenomena on Reynolds and Strouhal number are studied. Another objective is to exam-

ine unsteady phenomena for different rear geometries and to explain potential differences by means of unsteady surface pressure measurements.

3.2.1 Analysis of unsteady mechanism by surface pressure measurements

3.2.1.1 Analysis of all pressure tappings

The surface pressure amplitudes found for a quasi-steady change from $\beta = +3.3°$ to $\beta = $ -3.3° are presented in Figure 3.4 versus the x-coordinate. Therein, *front/side*, *a-pillar*, *c-pillar* and *rear side* denote the pressure tapping groups as indicated in Figure 3.2. According to the results, surface pressure changes encountered during a change of yaw angle are largest at the front and particularly at the a-pillar of the vehicle. This indicates that a large part of the side force at constant yaw originates from the front part of a car, which is already known from previous investigations (e.g. [107]). Pressure changes at the side, the c-pillar and the rear side are of similar magnitude.
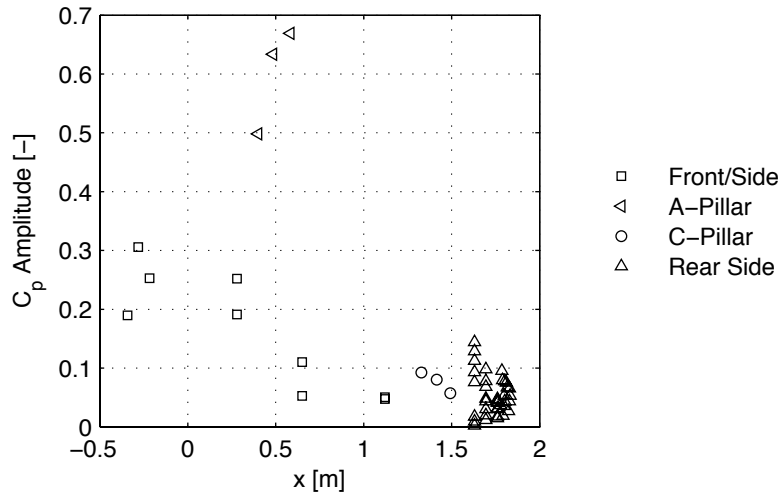
Figure 3.4: Steady pressure difference between $\beta = +3.3°$ and $\beta = $ -3.3° versus vehicle length.

During model oscillation the surface pressure exhibits periodic oscillations, as well. Calculating the phase lag between unsteady and quasi-steady pressure transients at each measurement position and evaluating their unsteady and quasi-steady peak-to-peak amplitudes leads to the results presented graphically in Figure 3.5 and Figure 3.6. The unsteady pressure amplitude denotes the amplitude of the pressure fluctuation during model oscillation. The quasi-steady pressure amplitude denotes the pressure change between maximum and minimum yaw position for steady flow conditions.
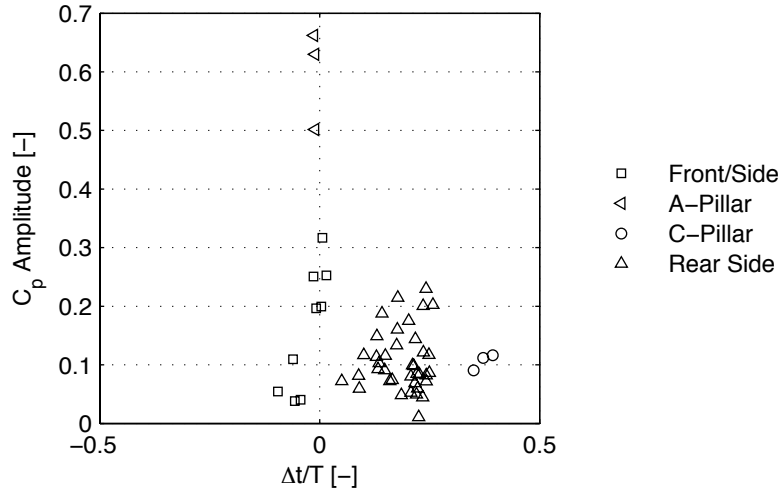
Figure 3.5: Unsteady pressure amplitude versus phase of unsteady against quasi-steady pressure transient.

According to Figure 3.5, the largest unsteady pressure fluctuations occur at the vehicle front and at the a-pillar, which agrees with the findings for steady pressure changes. As shown in Figure 3.6, surface pressure transients at the a-pillar show neither a significant phase lag nor a magnification of amplitude against a quasi-steady change of the oncoming flow. The same applies to the tappings located along the front bumper, who instantly react on a yaw angle change, as well. At the vehicle side, a slightly negative time lag appears, though unsteady pressure amplitudes are similar to quasi-steady amplitudes. Unsteady surface pressure amplitudes at the c-pillar are slightly larger than quasi-steady and exhibit a time shift of $\Delta t/T \approx +0.4$ relative to their quasi-steady developing.
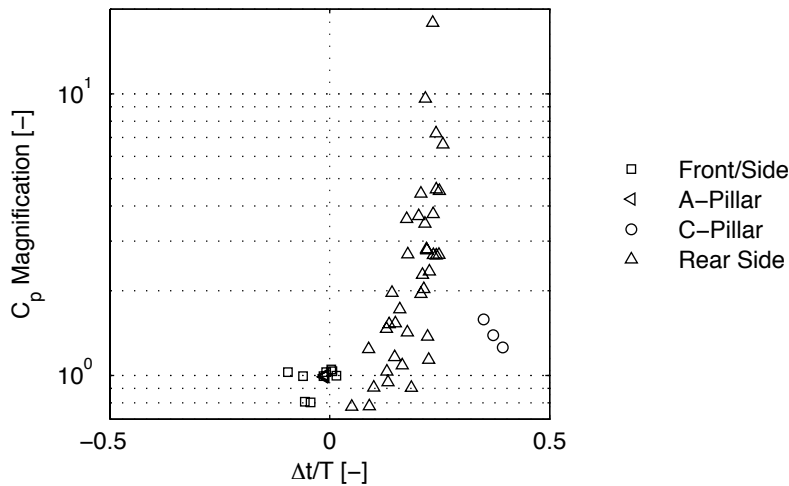
Figure 3.6: Ratio of unsteady to quasi-steady pressure amplitude versus phase of unsteady against quasi-steady pressure.

Most important, unsteady pressure amplitudes at the rear side of the vehicle exceed their quasi-steady amplitudes by up to ten times. Additionally, the phase lag of the unsteady pressure signals at the rear side against the model motion are between $\Delta t/T = +0.1$ and

$\Delta t/T = +0.3$. Hence, the pressure tappings with largest pressure magnifications also exhibit considerably larger phase lags than anywhere else except for the c-pillar.

To conclude, differences between unsteady and quasi-steady pressure developments are not observed at the vehicle front, but are most evident at the rear side. These findings agree with results of Theissen et al. [83, 108, 110] and Passmore et al. [83], who found unsteady surface pressures at the vehicle rear to be larger than expected from steady measurements. Passmore et al. [83] reported pressure phase lags at the side of a Davis model of maximum $\Delta t/T \approx 0.4$, whereupon the area of such high phase lags became restricted to the rear side of the model with increasing Strouhal number. Despite of different Strouhal and Reynolds numbers, the results of this study correspond fairly well to the findings of Passmore.

3.2.1.2 Analysis of pressure tappings in a z-slice

In order to gain further insight into the evolution of surface pressures along the vehicle, a z-slice at $z = 65\,\mathrm{mm}$ (in scale 1:2; indicated in Figure 3.2) is investigated. Figure 3.7 outlines differences between windward and leeward pressures at 13 positions between front and rear stagnation point for $\beta = \pm 3.3°$. Therein, unsteady pressure differences are derived from $t/T = 0.25$ and $t/T = 0.75$. Note that this is not identical with the unsteady pressure amplitude presented previously, but approximately corresponds to the times, where the yaw moment peaks (compare Figure 1.9). Measurements are only taken at the scatter marks in Figure 3.7, but are linearly interpolated in between for reasons of clarity and comprehensibility.
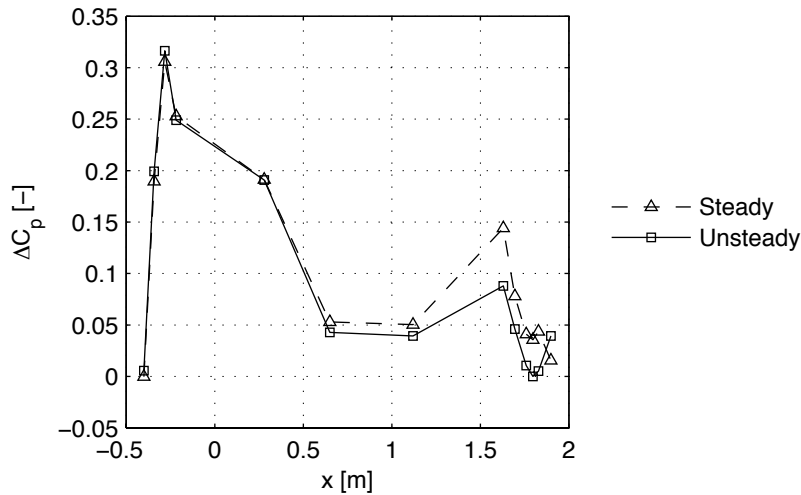
Figure 3.7: Steady and unsteady pressure differences between windward and leeward side at $\beta = 3.3°$.

As mentioned previously, the pressure differences between windward and leeward side are largest at the front, particularly where the front bumper migrates to the fender. There, pressure differences between windward and leeward side are three times as high compared

to locations at the rear. According to Figure 3.7, steady and unsteady pressure amplitudes are very similar at the front but differ most severely behind the rear wheel house.

In the following, surface pressure differences are translated into force contributions, which illustrates the impact they provoke. Assuming ideal measurement conditions and a totally symmetric setup, the pressure differences presented in Figure 3.7 correspond to the difference of right and left side surface pressures at maximum or minimum yaw. The resulting unsteady side forces and yaw moments are schematically presented in Figure 3.8 for $\beta = +3.3°$.

According to Figure 3.7, steady and unsteady surface pressures are higher at the windward than at the leeward side throughout the whole vehicle length. Hence, a negative total side force acts on the vehicle when being subjected to steady and unsteady crosswind at yaw=+3.3°. The side force of the front part is in any case larger than the side force of the rear part, since the pressure difference between windward and leeward side is bigger at the front than at the rear (compare Figures 3.5 and 3.7). As outlined in Figure 3.8 the sum of frontal and rear side force results in a positive yaw moment.

The frontal side force is equal for steady and unsteady flow conditions, since steady and unsteady surface pressure amplitudes are equal. However, at the rear, the unsteady pressure difference between windward and leeward side is smaller than in the steady case, see Figure 3.7. Therefore, the unsteady side force generated at the rear is smaller than the steady side force (see Figure 3.8). As a consequence, the unsteady yaw moment is larger than the steady yaw moment at $t/T = 0.25$ and $t/T = 0.75$. In contrast, the unsteady total side force is smaller than the steady total side force at those times.
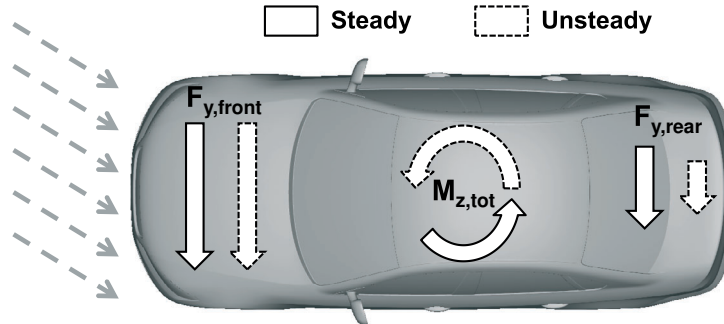
Figure 3.8: Schematic of yaw moment overshoot due to unsteady and quasi-steady pressure differences.

3.2.1.3 Conclusion

Thus, the analysis of surface pressure measurements at $z = 65\,\mathrm{mm}$ confirms the unsteady mechanism proposed by Theissen [107]. At the vehicle front, the flow instantly reacts on a change of the oncoming flow, whereas pressure oscillations at the rear vehicle side are amplified and delayed. Similar characteristics of unsteady pressure distributions have been found by Passmore et al. [83] and by Guilmineau and Chometon [50], who identified hysteresis effects for pressure tappings towards the rear of their models.

By the results presented, it is shown that the unsteady pressure differences at the rear generate a smaller unsteady side force component at the times, where the yaw moment peaks. This increases the total yaw moment and decreases the total side force compared to steady flow. As a consequence, the unsteady yaw moment transient exceeds and the unsteady side force transient undershoots its quasi-steady approximation, as shown in Figure 1.9 from Theissen [107].

3.2.2 Quantitative analysis of surface pressure distribution at the rear side

With the above, differences between unsteady and quasi-steady loads are proved to originate from the vehicle rear. In the following, surface pressure measurements on the rear side are studied in order to illustrate, why the unsteady rear side force is smaller than its quasi-steady approximation at the times of peak yaw moment. To this end, the non-dimensional pressure distribution in a square area at the right rear side of the notchback model is displayed in the following figures. Pressures were measured at the positions indicated with black points and interpolated in the area between.

3.2.2.1 Steady results
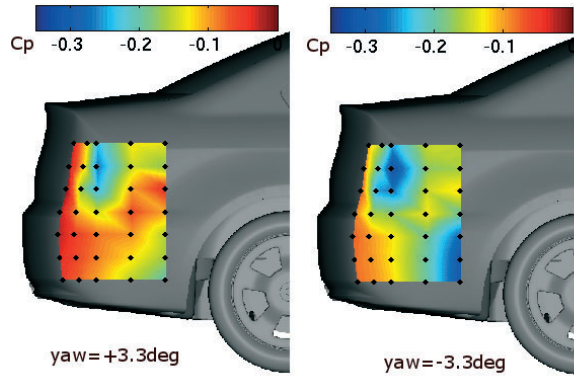
Figure 3.9: Steady pressure distribution at windward (left plot) and leeward (right plot) rear side at $\beta = 3.3°$.

Figure 3.9 shows the steady pressure distribution for $\beta = \pm 3.3°$. The pressure distribution within the measurement plane is not homogeneous. On the windward and the leeward side, the fluid is accelerated in the upper region towards the rear light until the flow separates and the pressure increases again. In the lower region of the measurement plane, the pressure is low close to the rear wheel housing, where the flow is still detached, and gradually increases towards the rear. The overall pressure level is significantly higher on the windward rear side. The acceleration of the flow in the upper mid region and the corresponding pressure drop are more intense on the leeward side, which corresponds well with the finding of leeward inflow in this height, as published by Gohlke et al. [48], Lemke [70] and Theissen et al. [107, 108, 110].
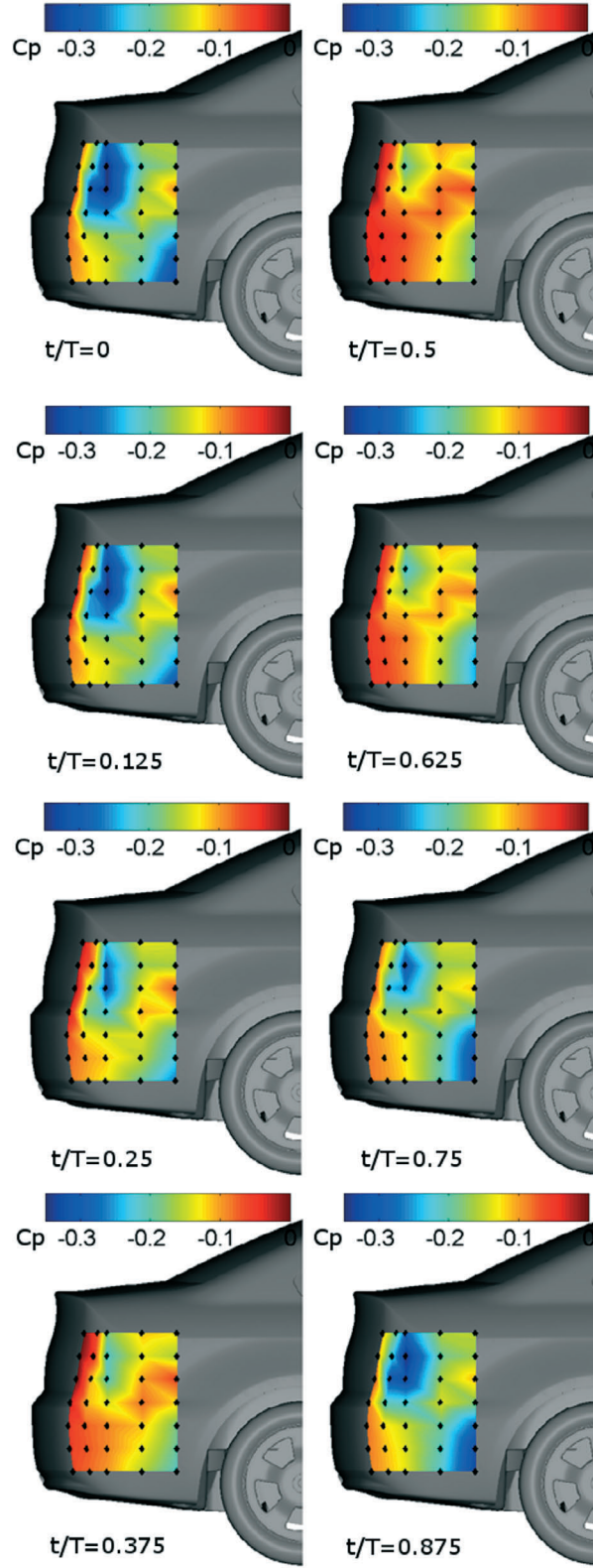
Figure 3.10: Unsteady periodically averaged pressure distribution for $f = 2\,\text{Hz}$, $\beta = \pm 3.3°$ at different instants of a full period.

3.2.2.2 Unsteady results

Figure 3.10 presents the periodically averaged pressure distribution on the rear side for the standard test case at discrete times of the oscillation period, where $\beta = +3.3°$ corresponds to $t/T = 0.25$ and $\beta = -3.3°$ to $t/T = 0.75$ (compare Figure 3.3). The unsteady pressure distribution at the rear side exhibits the same characteristics as during steady flow conditions, i.e. a low pressure spot in the upper region and behind the rear wheel housing. The size and strength of the low pressure spot show periodic behavior. Though such a periodic behavior is expected, the pressure distributions at $t/T = 0.25$ and $t/T = 0.75$ do not agree with the steady distributions at $\beta = \pm3.3°$ presented in Figure 3.9. The surface pressure distribution at $\beta = +3.3°$ corresponds rather to the unsteady surface pressure distribution between $t/T = 0.375$ and $t/T = 0.5$. Consequently, there must be a time lag between quasi-steady and unsteady pressure development within the area of the rear side measurement plane, which is also visible in Figure 3.6.

3.2.2.3 Differences between steady and unsteady results

To calculate forces, pressure distributions have to be integrated over the surface. Here, this is simplified by computing the average of all pressure signals at the rear side. The average pressure times the measurement square area serves as approximation for the side force generated at the rear. In Figure 3.11, the unsteady average pressure transient is illustrated together with its quasi-steady development. The quasi-steady minimum and maximum values are derived from steady measurements at $\beta = \pm3.3°$.
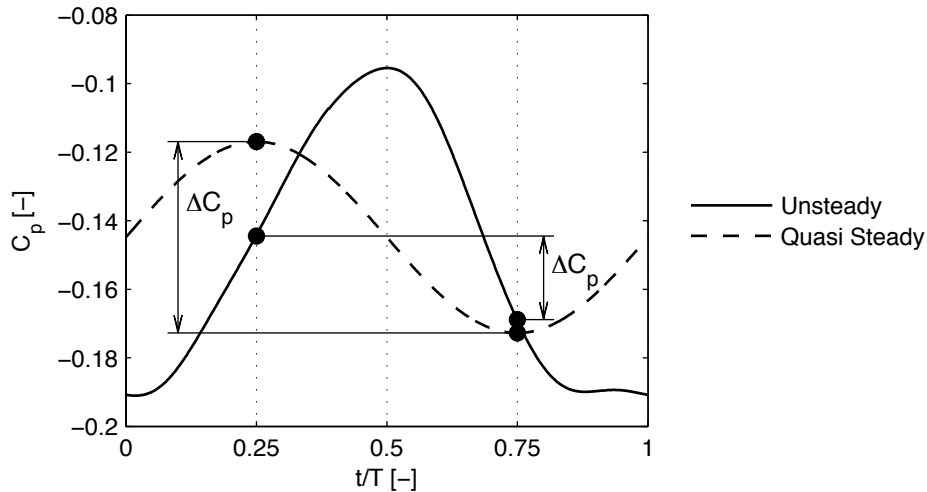
Figure 3.11: Mean of all periodically averaged pressure signals within the measurement plane at the rear side.

According to Figure 3.11, the mean unsteady pressure variation at the rear side is larger than the corresponding quasi-steady pressure variation. Hence, the maximum unsteady contribution of this area to the side force is larger than its quasi-steady approximation. However, this unsteady side force possesses a time lag of $\Delta t/T \approx +0.25$ relative to the

model motion. At $t/T = 0.25$ and $t/T = 0.75$, where the total yaw moment peaks in the the oscillation period (compare Figure 1.9), the unsteady side force at the rear is consequently smaller than the quasi-steady side force. This is indicated in Figure 3.11 by means of pressure differences between windward and leeward side or $t/T = 0.25$ and $t/T = 0.75$, respectively.

Summarizing these findings, the unsteady yaw moment exceeds its quasi-steady approximation due to a significant delay of pressure oscillations at the vehicle rear, which are actually magnified. Following from this, it is not only the unsteady and quasi-steady pressure amplitude, but particularly their phase lag, which is the crucial parameter with respect to their yaw moment contribution. In order to localize, where the amplitude and phase shift are maximum, their distribution upon the rear side is studied more in detail in the following.
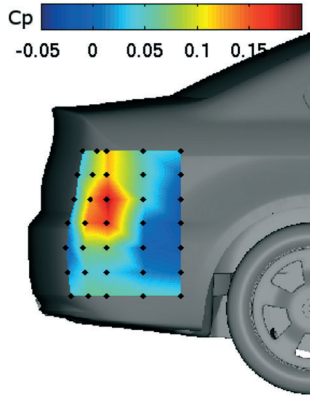
Figure 3.12: Difference in peak-to-peak amplitude between unsteady and quasi-steady pressures at $f = 2\,\mathrm{Hz}$, $\beta = \pm 3.3°$.
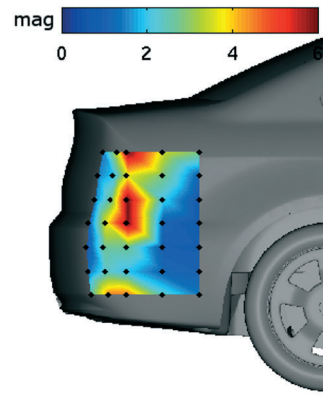
Figure 3.13: Unsteady magnification of quasi-steady pressure amplitudes at $f = 2\,\mathrm{Hz}$, $\beta = \pm 3.3°$.

Figure 3.12 illustrates the difference between unsteady and quasi-steady pressure amplitude within the rear side measurement plane for the standard oscillation case. According to Figure 3.12, unsteady pressure amplitudes exceed their quasi-steady values particularly within a region at mid length of the measurement surface, as colored red in Figure 3.12. There, the ratio of unsteady to quasi-steady amplitudes reaches values as high as 6, see Figure 3.13. It is worth mentioning that this ratio is rarely below 1 within the whole measurement surface.

Figure 3.14 shows the time lag between unsteady and quasi-steady pressure transients for all tappings in the measurement square. Interestingly, the regions of highest unsteady pressure amplitude magnification exhibit relatively large phase lags, as well. The phase lag is mainly between $\Delta t/T \approx +0.2$ and $\Delta t/T \approx +0.3$, except towards the rear wheel housing and behind the rear lights. As shown before, it is $\Delta t/T \approx +0.25$ in average.
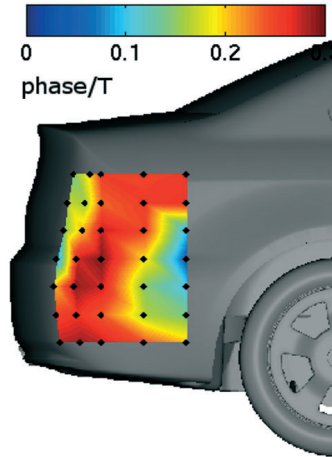
Figure 3.14: Phase lag between unsteady and quasi-steady pressures transients at $f = 2\,\mathrm{Hz}$, $\beta = \pm 3.3°$.

3.2.2.4 Summary

The surface pressure distribution at the rear side of the DrivAer notchback is characterized by low pressure regions behind the rear wheel house and around the rear lights, which are much more pronounced on the leeward side. During model rotation these low pressure spots exhibit periodic oscillations. The amplitude of these oscillations turns out to be larger than for a quasi-steady change of yaw and occur with a significant phase lag relative to the model motion. The magnification and delay is most prominent close to the rear lights, where the leeward inflow into the wake region was proved to occur [54].

So, the periodic behavior of the leeward inflow is shown to provoke periodic surface pressure oscillations on the rear side, which are enhanced and delayed against quasi-steady flow behavior. Thus, the unsteady lateral force generated at the rear side is amplified and delayed, as well. Due to this time delay, the rear side force at peak yaw is reduced compared to steady conditions, which explains the unsteady yaw moment overshoot reported by Theissen [107].

3.2.3 Dependency of unsteady phenomena on gust characteristics

Above, the physical mechanism is outlined which was observed during the standard oscillation at $f = 2\,\mathrm{Hz}$, $\beta = \pm 3.3°$. In the following, the described unsteady phenomena are discussed regarding their dependency on Strouhal number, Reynolds number and oscillation amplitude. To this end, aerodynamic load measurements are analyzed. Among the aerodynamic loads it is focused on the side force, roll and yaw moment, which turned out to feature largest variations. Hence, they are of major concern regarding driving stability under gusty crosswind conditions (compare Theissen [107] and Figure 1.9).

3.2.3.1 Amplitude dependency

First, the dependency on the oscillation amplitude is studied. In addition to the standard test case, measurements at $2\,\text{Hz}$ oscillation frequency and $210\,\text{km/h}$ wind speed are conducted for oscillation amplitudes $\beta = \pm 2.2°$ and $\beta = \pm 4.4°$. The resulting unsteady and quasi-steady amplitudes of side force, roll moment and yaw moment are plotted against the oscillation amplitudes in Figure 3.15. Therein, load amplitudes denote half of the peak-to-peak amplitudes. Measurements are only taken at the scattered marks, but linearly interpolated in between for reasons of clarity and comprehensibility of trends.
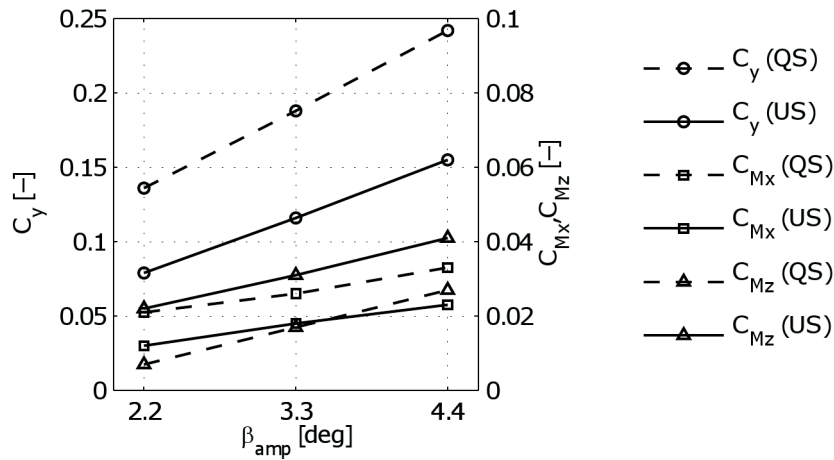
Figure 3.15: Unsteady (US) and quasi-steady (QS) load amplitudes for $f = 2\,\text{Hz}$, $u_{wind} = 210\,\text{km/h}$ and various oscillation amplitudes.

As expected, unsteady as well as quasi-steady side force, roll and yaw moment increase for larger oscillation amplitudes. This is physically reasonable, since the strength of an aerodynamic excitation magnifies for higher yaw angles. Within the investigated yaw angle range, unsteady side forces and roll moments are consistently smaller than quasi-steady side forces and roll moments, whereas unsteady yaw moments exceed their quasi-steady values. It can be concluded that the oscillation amplitude does not alter the standard characteristics of steady and unsteady aerodynamic loads, namely an overshoot of yaw moment and undershoot of side force and roll moment.

Figure 3.16 outlines the differences between unsteady and quasi-steady loads. Therein, force and moment axes ranges cover roughly three half of their quasi-steady changes, which is to facilitate relative comparison of load differences. According to Figure 3.16, the absolute difference between unsteady and quasi-steady side force increases slightly with increasing amplitude, whereas the differences between unsteady and quasi-steady roll and yaw moment remain rather constant within the investigated amplitude range. It is important to mention that only a very limited yaw amplitude range is considered here. In addition to that, Theissen presented numerical simulations for a yaw range of $\pm 3°$ to $\pm 9°$ [107]. He found that differences between unsteady and quasi-steady side force, roll moment and yaw moment were within 0.040 for ΔC_y and 0.005 for ΔC_{M_x} and ΔC_{M_z}. According to these findings, the slight change of side force in Figure 3.16 is not physical but created by hazard due to a limited amplitude range.
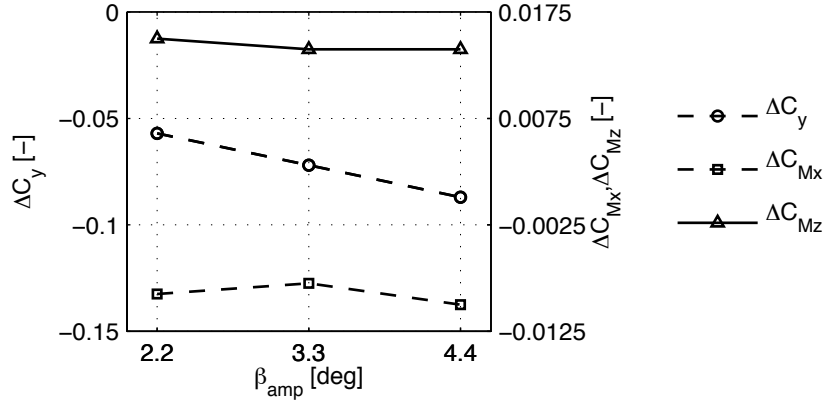
Figure 3.16: Difference between unsteady and quasi-steady load amplitudes at $f = 2\,\text{Hz}$, $u_{wind} = 210\,\text{km/h}$ and various oscillation amplitudes.

Following from the above, the yaw moment overshoot and side force undershoot appear to be constant regardless of the amplitude. According to Theissen, this conclusion is limited to yaw angles $-9° \leq \beta \leq +9°$ for a similar notchback, as the flow topology changes substantially for $|\beta| > 9°$. As a consequence, the ratio of unsteady to quasi-steady yaw moment is not constant, but largest for small yaw angle changes around zero, where quasi-steady values are smallest. This is outlined in Figure 3.17.
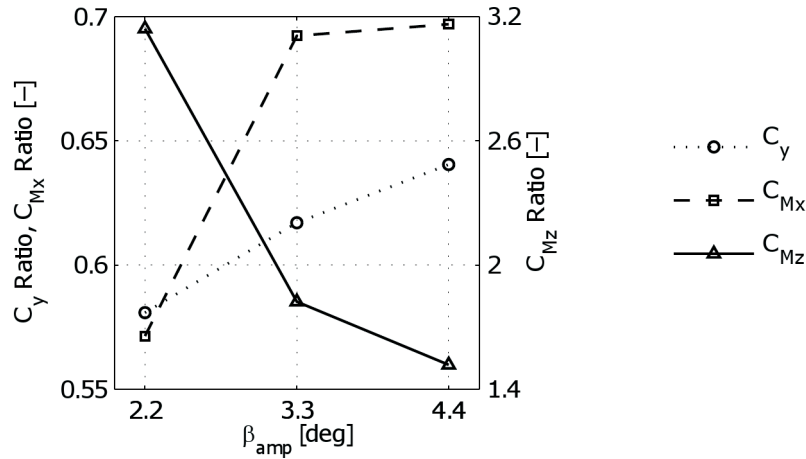
Figure 3.17: Ratio of unsteady to quasi-steady load amplitudes at $f = 2\,\text{Hz}$, $u_{wind} = 210\,\text{km/h}$ and various oscillation amplitudes.

Additionally, Figure 3.17 reveals that the ratio of unsteady to quasi-steady yaw moment is neither linear with respect to a change of the oscillation amplitude. Therefore, linear concepts such as aerodynamic admittance are doubtful. Aerodynamic admittance was introduced by Davenport [31] and applied in many investigations to unsteady vehicle aerodynamics. It is calculated as the ratio of the frequency spectrum of unsteady to quasi-steady loads. Per definition, this ratio only depends on the frequency and increases linearly with amplitude. According to Figure 3.17, the assumption of linear behavior is at least incorrect for yaw and roll moment in the investigated amplitude range. Simi-

lar observations and criticism on the concept of admittance were recently reported by Mankowski et al. [72].

3.2.3.2 Reynolds and Strouhal dependency

Next, the dependency of the unsteady mechanism on Strouhal and Reynolds number is investigated. The model is oscillated with $2\,\mathrm{Hz}$ frequency and $\pm 3.3°$ amplitude while the wind speed is increased in steps from $70\,\mathrm{km/h}$ up to $280\,\mathrm{km/h}$. In doing so, the Strouhal number decreases from 0.24 to 0.06 and the Reynolds number increases from $3.0 \cdot 10^6$ to $1.2 \cdot 10^7$. Reynolds and Strouhal number are defined according to Equations 1.1 and 1.2 using the frequency of the model oscillation, the vehicle length and the wind speed in the empty test section of the wind tunnel. Resulting unsteady and quasi-steady amplitudes of the non-dimensional load coefficients are illustrated in Figure 3.18. Measurements are again linearly interpolated in order to ease the visibility of trends.
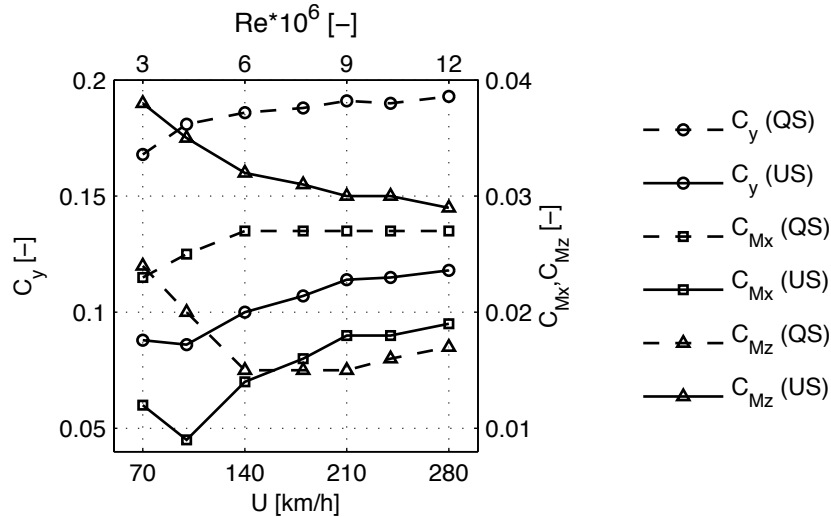
Figure 3.18: Unsteady (US) and quasi-steady (QS) load amplitudes at $f = 2\,\mathrm{Hz}$, $\beta = \pm 3.3°$ and varying wind speeds.

Quasi-steady measurements outline solely the influence of the Reynolds number, since $\mathrm{Sr} = 0$ without model rotation. According to Figure 3.18, Reynolds influence is observed for $\mathrm{Re} < 6 \cdot 10^6$ and quasi-steady load coefficients are approximately constant for higher Reynolds numbers. Unsteady measurements, however, depend on both Reynolds and Strouhal number. Unsteady side force and yaw moment are persistently smaller than the corresponding quasi-steady loads. Their unsteady values exhibit a small decrease from $70\,\mathrm{km/h}$ to $100\,\mathrm{km/h}$ before increasing again. The unsteady yaw moment coefficient decreases gradually with increasing wind speed, but consistently exceeds the quasi-steady yaw moment. So, the general characteristic, i.e. overshoot of yaw moment and undershoot of side force and roll moment, is observed throughout the investigated Reynolds and Strouhal number range.

When aiming for the largest effect of unsteady aerodynamic phenomena, the difference and the ratio of unsteady to quasi-steady yaw moment amplitude are of interest. The author assumes that this is determined by the interaction of the time scale generated by

the oscillation of the model and the time scale of the wake flow. The time scale of the wake flow is affected by the vehicle speed, the vehicle dimension and the vehicle shape. The Strouhal number changes with both, with a change of the oscillation time scale and a change of the wake flow time scale. Hence, it is appropriate to use the Strouhal number in order to characterize and estimate the effect of unsteady flow phenomena. Defined as in Equation 1.2, the Strouhal number implies the ratio of the two time scales mentioned,

$$\text{Sr} = \frac{f \cdot L_{veh}}{U} \sim \frac{\mathcal{T}_{wakeflow}}{\mathcal{T}_{oscillation}}.$$

Figure 3.19 displays the ratio of unsteady to quasi-steady side force, roll moment and yaw moment coefficients for various wind speeds. The yaw moment ratio shows a distinct behavior with a maximum at 140 km/h and a decrease towards lower and higher velocities. The peak corresponds to Sr = 0.12. It is pointed out that the peak ratio and peak Strouhal number depend on the vehicle shape and its dimensions. This means that the specific Strouhal peak presented in Figure 3.19 is only valid for the DrivAer notchback model.
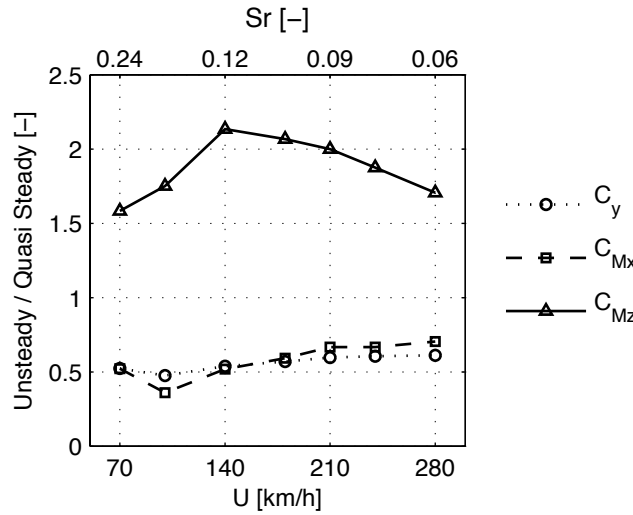
Figure 3.19: Ratio of unsteady to quasi-steady load amplitudes at $f = 2\,\text{Hz}$, $\beta = \pm 3.3°$ and varying wind speeds.

Applied to a full scale DrivAer notchback, which is driving at 140 km/h speed, the Strouhal number range investigated corresponds to a range of gust frequencies between 0.5 Hz and 2 Hz. Hence, almost the whole frequency spectrum measured on-road (see Figure 2.7) is covered. The results presented in Figure 3.19 imply that the largest aerodynamic impact for a full scale DrivAer notchback at 140 km/h speed would be expected for a gust with a frequency of 1 Hz. As mentioned previously, this excitation frequency is very close to typical frequencies of the first yawing mode of vehicle dynamics and is therefore particularly critical in terms of driving stability in gusty crosswind.

The findings presented in Figure 3.19 agree very well with numerical results from Theissen [107], which are shown in Figure 1.12. The yaw moment magnification curves are almost identical exhibiting a maximum of more than 2 at Sr $\approx$ 0.15 and a decrease towards lower and higher Strouhal numbers. The side force and roll moment magnification is similar, as well. Though Theissen's side force and roll moment curves start slightly higher and

feature slightly more pronounced and slightly shifted minima, they agree on ending at constant amplification factors around 0.5 with increasing Strouhal numbers.

The results of this work also match findings of Schröck et al. [96], who reported a maximum yaw moment magnification at Sr ≈ 0.12 for a generic 1:5 scale SAE model using oscillating airfoils. There, the Strouhal number was based on the wheelbase instead of the vehicle length. The value of the yaw moment magnification at Sr ≈ 0.12 was, however, significantly smaller compared to the results presented in this work.

3.2.4 Dependency of unsteady phenomena on rear geometry

Since the unsteady phenomena presented above are essentially attributed to flow phenomena at the rear of the DrivAer notchback, a variation of the rear geometry is studied in the following. For this purpose, three different rear variants of the DrivAer model, namely a notchback, fastback and station wagon (see Figure 3.2) vehicle, are compared. Their bodies are identical except for the different rear modules, which are enclosed by thin, black lines in Figure 3.2.

3.2.4.1 Load measurements

First, results of unsteady load measurements at standard oscillation ($f = 2\,\mathrm{Hz}$, $\beta = \pm 3.3°$) are presented for the three geometry variants. In this context, unsteady peak values denote half of the peak-to-peak amplitude. It is focused again on the side force, roll and yaw moment. Tables 3.2, 3.3, 3.4 and 3.5 compare unsteady and quasi-steady peak loads of the notchback, fastback and station wagon as well as the phase lag of unsteady load transients against the model oscillation.

Table 3.2: Half of unsteady (US) and quasi-steady (QS) peak-to-peak load amplitudes at $f = 2\,\mathrm{Hz}$, $\beta = \pm 3.3°$ for different rear geometries.

	C_y		C_{M_x}		C_{M_z}	
	US	QS	US	QS	US	QS
Notchback	0.116	0.188	0.018	0.026	0.031	0.017
Fastback	0.117	0.182	0.016	0.025	0.030	0.019
Station Wagon	0.129	0.191	0.017	0.026	0.020	0.014

Due to different lateral cross sections, the steady side force is commonly largest for a station wagon and smallest for a notchback (compare Hucho [58]). According to Table 3.2, however, the side force exhibits a similarly large peak of around 0.190 for all three variants. Numerical simulations showed that the strut influences the flow such that the pressure differences between windward and leeward c-pillar of notchback and fastback are reduced. Consequently the steady side forces of notchback and fastback are increased as opposed to a simulation setup without the strut. Due to this, only slightly different steady side forces are measured for the station wagon and the other two geometries. The unsteady

side force peaks are consistently smaller and have a positive phase lag. Among the three variants, the station wagon exhibits the largest unsteady side force and a slightly smaller phase lag compared to notchback and fastback. Thus, the difference between unsteady and quasi-steady side force is smallest and their ratio is largest for the station wagon.

Table 3.3: Difference between half of unsteady and quasi-steady peak-to-peak loads at $f = 2\,\text{Hz}$, $\beta = \pm 3.3°$ for different rear geometries.

US-QS	C_y	C_{M_x}	C_{M_z}
Notchback	-0.072	-0.008	+0.014
Fastback	-0.065	-0.009	+0.011
Station Wagon	-0.062	-0.009	+0.006

Table 3.4: Ratio of unsteady to quasi-steady peak loads at $f = 2\,\text{Hz}$, $\beta = \pm 3.3°$ for different rear geometries.

US/QS	C_y	C_{M_x}	C_{M_z}
Notchback	0.62	0.68	1.83
Fastback	0.64	0.66	1.59
Station Wagon	0.67	0.65	1.39

Table 3.5: Phase lag of unsteady against quasi-steady load transients at $f = 2\,\text{Hz}$, $\beta = \pm 3.3°$ for different rear geometries.

Δt/T	C_y	C_{M_x}	C_{M_z}
Notchback	0.06	0.11	-0.02
Fastback	0.06	0.10	-0.02
Station Wagon	0.04	0.08	-0.02

Steady and unsteady roll moment peaks are very similar for all geometry variants and differ by maximum 0.002. The ratio of unsteady to quasi-steady roll moment peaks is significantly below one. The phase lag is persistently positive, but largest for the notchback and smallest for the station wagon geometry.

Most interesting in this context is the yaw moment. As opposed to the side force and roll moment, steady yaw moments are considerably exceeded at unsteady flow conditions, as presented in Table 3.3 and Table 3.4. Though the steady yaw moments of the three variants differ by less than 0.005, their unsteady peak values diverge. The unsteady yaw moment of fastback and notchback are around 0.030, whereas the station wagon geometry exhibits only 0.020. A small negative phase lag is identically apparent between transient and quasi-steady developments for all three variants.

To sum up, the unsteady phenomena observed for the DrivAer notchback apply to all three rear geometries: The ratio of unsteady to quasi-steady yaw moment amplitudes

is larger than one, whereas this ratio is significantly below one for side force and roll moment. The side force undershoot is slightly less pronounced for the station wagon. More evident, however, is that the yaw moment overshoot is most pronounced for the notchback and least pronounced for the station wagon geometry.

These findings confirm numerical results of Theissen [107] using a different setup, but the same DrivAer geometries. Theissen found that his proposed unsteady mechanism applies to all three variants. According to Theissen, as well, differences between unsteady and quasi-steady loads are less pronounced for the DrivAer station wagon than for the notchback and fastback variants. Similar studies are documented using generic vehicle models. Relevant in this context is for instance the work of Favre et al. [40], who modeled a wind gust in numerical simulations and found larger unsteady side force for the station wagon variant of an Ahmed body than for fastback-like variants with 10° and 35° rear slant angles. Larger unsteady yaw moments were encountered for the fastback variants, which confirms the principal results of this study. Experimental results of Schröck et al. [96] using oscillating airfoils and a notchback and fastback variant of the SAE model showed similar side force magnifications, but higher yaw moment magnification for the notchback than for the fastback, as well.

3.2.4.2 Surface pressure measurements

In the following, the differences observed in unsteady load measurements between notchback and station wagon geometry are assessed by analyzing surface pressure signals. Repeating the above, steady loads are similar for notchback and station wagon, whereas the unsteady yaw moment is significantly smaller for the notchback, compare Table 3.2.
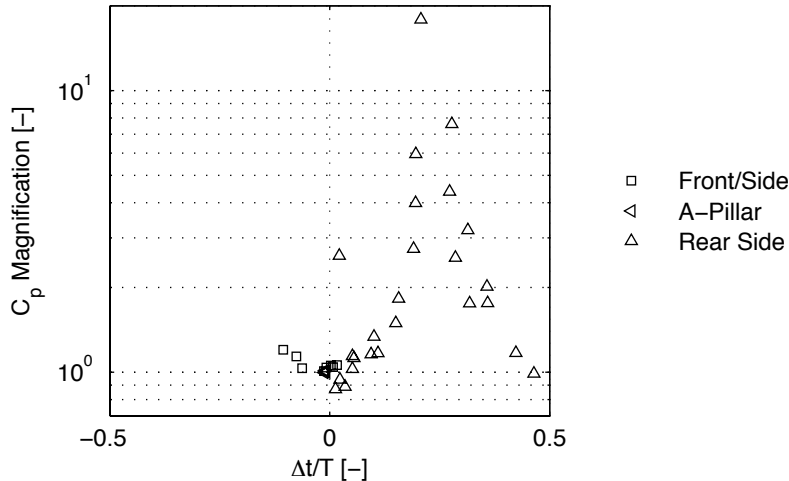
Figure 3.20: Unsteady magnification of quasi-steady pressure amplitudes versus phase of unsteady against quasi-steady pressure transients for the station wagon.

Figure 3.20 outlines the amplitude magnification versus phase of unsteady against quasi-steady pressure oscillations for all pressure tappings mounted in the station wagon model. The same plot is presented in Figure 3.6 for the notchback model. Though a comparison of these two figures is difficult due to the amount of measurement points, it provides

valuable indications for similarities and discrepancies. In particular, the unsteady pressure magnification and the phase lag encountered at the vehicle front are negligible for both notchback and station wagon. On the fullback side, unsteady pressures exceed their quasi-steady values slightly more compared to the notchback. The largest discrepancies are, however, found at the rear. There, the unsteady pressures exhibit for some parts considerably less magnification compared to the notchback. In addition, phase shifts are more diverse.

So, the general characteristics observed for the notchback, i.e. unsteady magnification and a significant phase lag at the rear, hold also true for the station wagon. In contrast to the rear, surface pressures at the front react instantaneously on a change of the oncoming flow. Finally, some pressure differences between station wagon and notchback are especially observed at the rear of the vehicle, which must be responsible for their different unsteady yaw moments.

To this end, the station wagon rear side is considered in the following. Figure 3.21 illustrates the difference between unsteady and quasi-steady pressure amplitude within the rear side measurement plane of the station wagon model at standard oscillation. Measurements are taken at the positions indicated with black dots and interpolated in-between. It is confirmed that there are significant unsteady to quasi-steady pressure differences, particularly within the upper left region of the measurement plane, being responsible for the unsteady phenomena observed in load measurements for the station wagon.
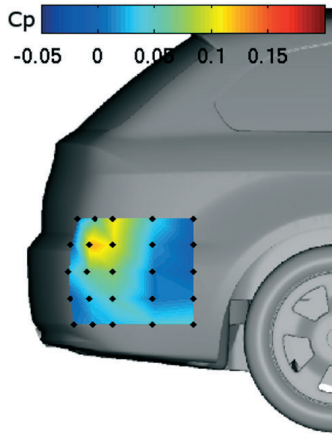
Figure 3.21: Difference in peak-to-peak amplitude between unsteady and quasi-steady pressures at $f = 2\,\text{Hz}$, $\beta = \pm 3.3°$ for the station wagon.
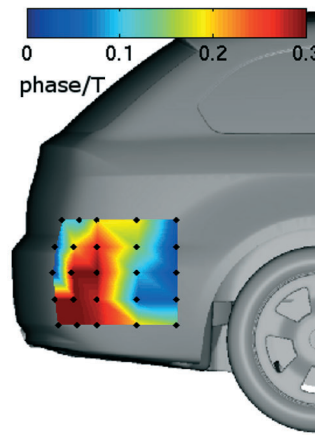
Figure 3.22: Phase lag between unsteady pressure transients and model motion at $f = 2\,\text{Hz}$, $\beta = \pm 3.3°$ for the station wagon.

The equivalent to Figure 3.21 was presented for the notchback in Figure 3.12. A comparison of Figure 3.12 and Figure 3.21 reveals that the differences between unsteady and quasi-steady pressures are apparently smaller for the station wagon. This becomes even more evident when comparing the mean of all 25 unsteady pressure transients measured at the lower rear side of station wagon and notchback, see Figure 3.23.

According to Figure 3.23, unsteady pressure variations are larger for the notchback geometry. Hence, the maximum unsteady pressure difference between windward and leeward measurement surface and thus the maximum unsteady side force at the rear are larger for the notchback. As mentioned before, it is, however, not sufficient to consider solely pressure amplitudes, but the phase lag has to be taken into account as well. From Figure 3.23 and a comparison of Figure 3.14 and Figure 3.22, it can be concluded that the transients of notchback and station wagon feature similar phase lags relative to their quasi-steady development.
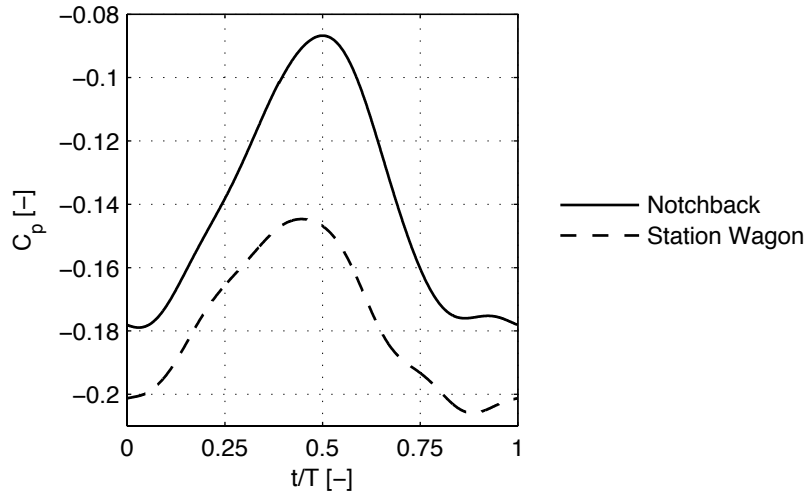
Figure 3.23: Unsteady periodically averaged pressure of the lowest 25 probes at the rear side for notchback and station wagon.

Given the lower unsteady pressure amplitude of the station wagon and similar phase lags, the unsteady yaw moment overshoot and the unsteady side force undershoot are expected to be less developed for the station wagon compared to the notchback geometry. This explains the unsteady loads presented in Table 3.3 and Table 3.4. Nevertheless, it could not be investigated to which extent the region further up than the measurements surface, which is captured by the pressure probes in this experimental study, attributes to the total yaw moment overshoot of the station wagon geometry. So, the explanation from the pressure distributions within the measurement square might be fragmentary. Theissen stated that differences between unsteady and quasi-steady yaw moments generally depend on the strength of the leeward inflow, the time delay of the wake flow and the size of the lateral impact area [107]. Hence, any variation of these parameters would influence the unsteady loads, which complicates the explanation of the observed differences.

3.3 Summary and conclusions

Unsteady aerodynamic flow phenomena are investigated in a wind tunnel by oscillating a realistic 1:2 scale vehicle around its vertical axis. Thus the vehicle is exposed to time-dependent flow conditions at realistic Reynolds and Strouhal numbers. Using this setup unsteady aerodynamic loads were observed by Theissen [107, 111] to differ significantly from quasi-steady loads. In particular, the unsteady yaw moment considerably exceeds

the quasi-steady approximation. On the other hand, side force and roll moment are overrated by quasi-steady approximation but exhibit a significant time delay.

The present work extends the characterization of the unsteady aerodynamic mechanism described by Theissen [107, 111]. The surface pressure distribution at the rear side of the DrivAer notchback is characterized by a low pressure regions around the rear lights. The low pressure region is more pronounced on the leeward side, where fluid with high lateral velocity enters the wake region according to several preceding studies [48–50, 54, 70, 107]. This low pressure spot exhibits periodic oscillations, which are enhanced and delayed relative to the model motion. Though an unsteady pressure magnification and delay appear all over the rear side measurement square, it is most prominent around the rear lights. In contrast, unsteady surface pressures at the vehicle front do not differ from their quasi-steady development. The described surface pressure development causes an unsteady side force at the rear, which increases the total yaw moment and decreases the total side force compared to their quasi-steady development. So, the unsteady mechanism proposed by Theissen [107] is confirmed and the amplitudes and phase lag of unsteady pressure oscillations at the rear are shown to be the crucial parameters with respect to unsteady load developments.

Besides, the dependency of the unsteady flow phenomena on the oscillation amplitude, the Reynolds and the Strouhal number is investigated. Unsteady overshoot of the yaw moment and undershoot of the side force and roll moment are encountered throughout all measurements. The differences between unsteady and quasi-steady loads remain within 0.005 for roll and yaw moment and within 0.030 for side force at oscillation amplitudes between $\pm 2.2°$ and $\pm 4.4°$. In turn, the ratio of unsteady to quasi-steady loads turns out neither to be constant, nor to behave linearly with respect to the oscillation amplitude. Therefore, linear concepts of aerodynamic load magnification are doubtful.

Measurements at various wind speeds enable to determine the dependency of aerodynamic loads on Reynolds and Strouhal number. At constant yaw Reynolds influence is small for $Re > 6 \cdot 10^6$. During model oscillation, it is assumed that the intensity of unsteady flow phenomena is determined by the interaction of the time scale of the model rotation and the time scale of the delayed wake flow, described by the Strouhal number. For the DirvAer notchback, the largest yaw moment magnification factors are found at $Sr = 0.12$.

Finally, the dependency of the unsteady phenomena on the rear geometry is studied. It is shown that the notchback, fastback and station wagon exhibit similar unsteady behavior, i.e. a decrease of side force and roll moment as well as an unsteady yaw moment overshoot. However, the yaw moment overshoot is less pronounced for the station wagon geometry, which is due to smaller unsteady pressure variations at the rear side of the station wagon.

As a last benefit from the experiments presented, a quantitative data base is created for a future validation of numerical tools for the simulation of unsteady vehicle aerodynamics. It has already been mentioned that an experimental approach using oscillating airfoils replicates a natural gust more realistically than an oscillating model approach, where the vehicle is not gradually captured by the lateral velocity distribution. For small yaw angle changes, however, the differences between both simulation methods diminish and the principal unsteady mechanism is identical, as shown by Theissen [107]. Working with oscillating models assures that the velocity distortion imposed on the vehicle is accurately

defined and limited to a single, discrete frequency. This is a major advantage compared to an experimental approach using oscillating airfoils and allows the validation of numerical solvers.

4 Validation of a numerical setup for aerodynamic simulations under time-dependent flow conditions

A reliable prediction of transient aerodynamic loads is indispensable when computing the dynamic response of a vehicle to crosswind gusts, which finally determines the perceived passenger's safety and comfort. Aerodynamic simulation tools are most promising in this context, since they can be applied at an early stage of the development process.

In the preceding chapter, valuable experimental data were acquired. They provide a quantitative understanding of the unsteady flow around a simplified passenger car model being subjected to realistic flow conditions during single crosswind gusts. In this chapter, the attempt to simulate the experiment numerically is presented. A detailed comparison of experimental and numerical results is performed to assess the capability and accuracy of the numerical simulation process. Regarding this process, the intention is to keep the computational effort as low as possible in order to prove the ability to apply such simulations in the industrial development process.

4.1 Numerical setup

Numerical simulations are carried out using Exa's commercial Lattice-Boltzmann solver PowerFLOW®, Version 4.2, whose physical approach and implementation is summarized in chapter 1.5.1.

4.1.1 Model and scale

The geometrical setup is, wherever possible, identical to the experimental setup. A surface mesh of the 1:2 scale DrivAer notchback, illustrated in Figure 3.1, is generated based on CAD data. Differences between the CAD geometry and the final, assembled geometry are regarded as negligible and are not accounted for. As mentioned in chapter 3.1, the strut geometry used in the experiments is slightly asymmetric. It was scanned during the experiments and a surface mesh was generated based on the scan data instead of the CAD data. However, the scan was not performed right after the test runs and thus differs minimally from the real test status. The vehicle model and strut geometry used for the numerical simulations are outlined in Figure 4.1.

Figure 4.1: Geometric setup for numerical simulation.

The simulation setup comprises only the components being located in the free jet of the wind tunnel experiment, i.e. the vehicle and the strut. The wind tunnel geometry is not reproduced. Recent investigations [3, 30] showed that this is necessary for small scale model wind tunnels with high blockage ratios. Since the nozzle cross-section of BMW's Aerolab wind tunnel is very large ($14\,\mathrm{m}^2$, blockage experiment 0.8%) and since experimental blockage corrections are not necessary in the Aerolab wind tunnel [90], it is correct to omit its replication in the simulation.

4.1.2 Domain and boundary conditions

The simulation volume is a box with 6 vehicle lengths in front, aside and behind the vehicle model and a height of 30 vehicles above each other. Hence, the blockage ratio calculates to less than 0.1%, whereas it is 0.8% in the experiment. At the inlet the velocity is $58.3\,\mathrm{m/s}$, the turbulence intensity is 0.5% and the turbulent length scale is set to $1.5\,\mathrm{mm}$. This is in line with the inlet conditions during the experiment. The same holds true for the static pressure prescribed at the outlet, which is the wind tunnel plenum pressure recorded during the experiments. The top of the simulation volume as well as the side

walls are defined as frictionless walls. The floor is a moving wall with the same velocity as the inlet velocity of the flow. The vehicle and strut surface are treated as normal walls. In line with the experiment, the wheels do not rotate.
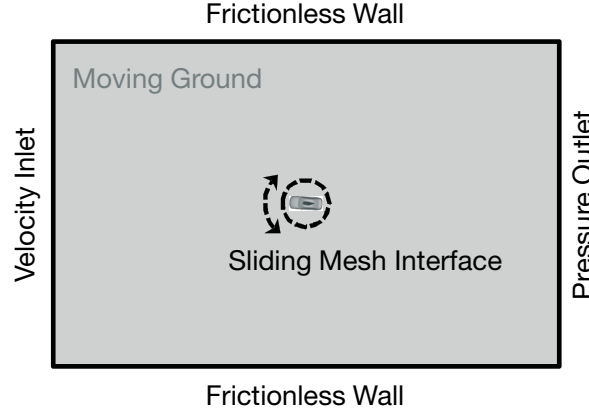
Figure 4.2: Top view of numerical domain with sliding mesh interface and boundary conditions.

4.1.3 Model motion

The oscillation of the vehicle in the experiment is modeled using a sliding mesh interface between rotating and non-rotating domain, see Figure 4.2. The mesh interface is set up on a cylinder with 1.8 m radius around the rotating axis and reaches from the moving belt up to the top of the strut. Amplitude and frequency of the rotation are identical to the standard test case of the experiment, i.e. $f = 2\,\mathrm{Hz}$ and $\beta = \pm 3.3°$. Additional simulations are performed at constant yaw for the approximations of quasi-steady load transients, to which the unsteady developments are compared.

As mentioned by Theissen [107], turbulent fluctuations of the flow field around bluff bodies as well as the non-deterministic nature of Lattice Boltzmann solvers result in slightly different aerodynamic peak loads when simulating several gust events consecutively. At a confidence level of 95%, the confidence interval is only 0.016 for C_y and 0.006 for C_{M_x} and C_{M_z} when simulating a single gust event or a single oscillation period. Therefore, five full oscillations are modeled and phase averaged. Then, the confidence interval improves to 0.006 for C_y and 0.002 for C_{M_x} and C_{M_z}. In other words, the probability that the phase averaged yaw moment peak is in a range of ± 0.002 around the phase-averaged peak value is 95%.

4.1.4 Numerical grid

The standard numerical grid has three layers with a cell size of 1.5 mm, which surround the whole vehicle. Nine layers with 3 mm cell size follow. Then, the cell size is coarsened using two offset regions of the vehicle geometry and five rectangular boxes, which are positioned one into another. The dimensions of the first offset region defining a local cell

size of 6 mm and the second offset region defining a local cell size of 12 mm are outlined in Table 4.1. An overview and a close view of a cut through the numerical grid at $y = 0$ are presented in Figure 4.3. Therein, the innermost layers, the two offset regions and the rectangular boxes are clearly distinguishable. The total number of cells of the standard numerical grid amounts to 37.8 million.
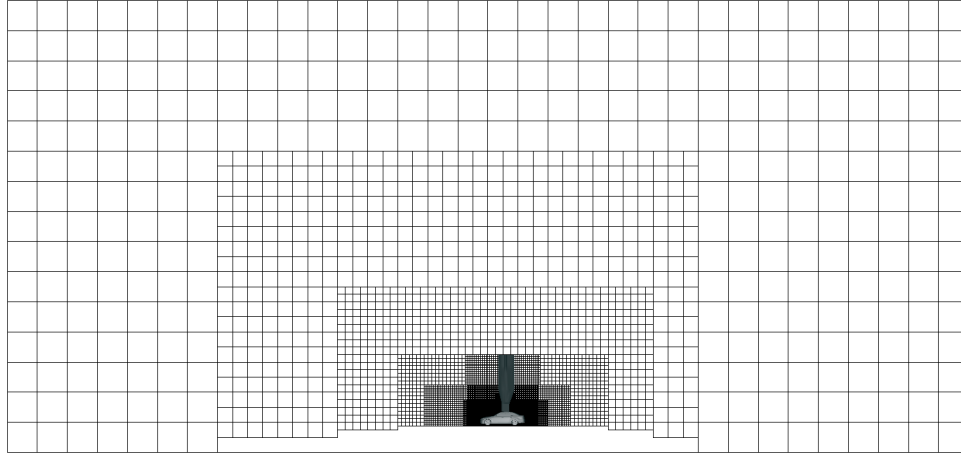
(a) Overview
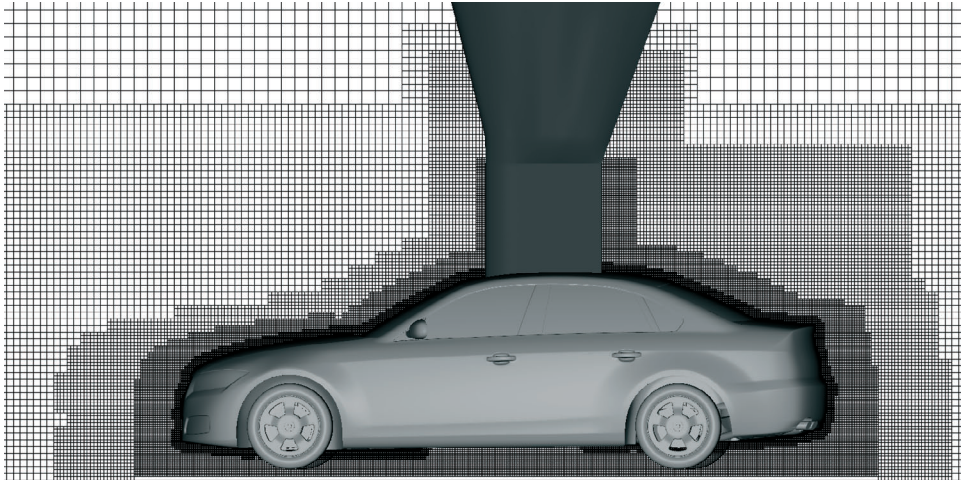
(b) Close View

Figure 4.3: Cut through the grid at $y = 0$ from far away and close up.

Table 4.1: Dimensions of offset regions for local refinement of standard numerical grid relative to model dimensions.

Cell Size	L/L_{veh}	B/B_{veh}	H/H_{veh}
6 mm	1.15	1.14	1.24
12 mm	1.36	1.44	1.34

4.1.5 Data processing

Fluid measurements are sampled with 50 Hz, force and surface pressure measurements even with 1000 Hz. At constant yaw, data are averaged over at least 0.8 s. According to Theissen [107], reproducibility of aerodynamic loads during constant yaw then varies by maximum ±0.003 for C_y and ±0.001 for C_{M_x} and C_{M_z}. During transient yaw, measurement data of all five oscillation periods are phase averaged. Eventually, data are 11 Hz low pass filtered in analogy to the experimental data processing. When comparing flow fields during model oscillation at maximum or minimum yaw with flow fields during constant yaw, fluid data are averaged over 0.1 s around maximum or minimum yaw position. Forces, moments and pressures are generally non-dimensionalized according to Equations 1.4, 1.5, 1.6 and 1.7.

4.1.6 Simulation performance

The combination of high Reynolds number and long physical simulation time put high demands on hardware resources. The total physical simulation time is 5.8 s for five oscillations and two constant yaw states. The numerical time step is $3.97 \cdot 10^{-6}$ s. With the numerical setup presented, the simulation run for about 300 h on 96 cores.

4.2 Grid study

The standard numerical grid is based on the methodology of Schäufele [90] and Theissen [107]. Still, the dependency of the numerical solution on the computational grid is investigated in the following for constant yaw.

4.2.1 Variation of grid resolution at vehicle surface

First, the resolution of the numerical grid is varied at the surface of the vehicle. To this end, the two finest local refinements around the vehicle surface used for the standard grid are omitted step by step. Thus, numerical grids with a finest resolution of 3 mm and 6 mm are generated in addition to the standard grid with 1.5 mm, which leads to the grid characteristics outlined in Table 4.2.

Conclusions on the quality of the numerical results for the three computational grids are based on aerodynamic loads at constant yaw β = -3.3°. Table 4.3 compares these loads with experimental reference data. According to the results, the differences between simulation and experiment are consistently smaller for grids with smaller cell size at the vehicle surface. In particular, the side force, roll moment and yaw moment increase with decreasing cell size. So, the standard numerical grid gives best results.

Table 4.2: Characteristics of numerical grids at model scale 1:2 for various resolutions at the vehicle surface.

Resolution	δt [s]	Cell Elements	Surface Elements
1.5 mm	$1.6 \cdot 10^{-5}$	37.8 M	7.4 M
3.0 mm	$8.0 \cdot 10^{-6}$	18.1 M	3.2 M
6.0 mm	$4.0 \cdot 10^{-6}$	7.8 M	1.7 M

Table 4.3: Aerodynamic loads at β = -3.3° using numerical grids with various resolutions at model scale 1:2.

Finest Resolution	C_x	C_y	C_z	C_{M_x}	C_{M_y}	C_{M_z}
6.0 mm	0.266	0.181	-0.129	-0.026	-0.163	-0.038
3.0 mm	0.279	0.207	-0.099	-0.033	-0.157	-0.028
1.5 mm	0.283	0.226	-0.097	-0.036	-0.141	-0.020
Experiment	0.298	0.214	-0.006	-0.035	-0.125	-0.020

It can be shown that flow separations at the a-pillar, the c-pillar, the wheel houses and above the back window strongly depend on the grid resolution at the vehicle surface. Better resolution persistently decreases the size of detached flow regions, which is illustrated in Figure 4.4 for the separation behind the leeward rear wheel house at $z = 0.14$ m.
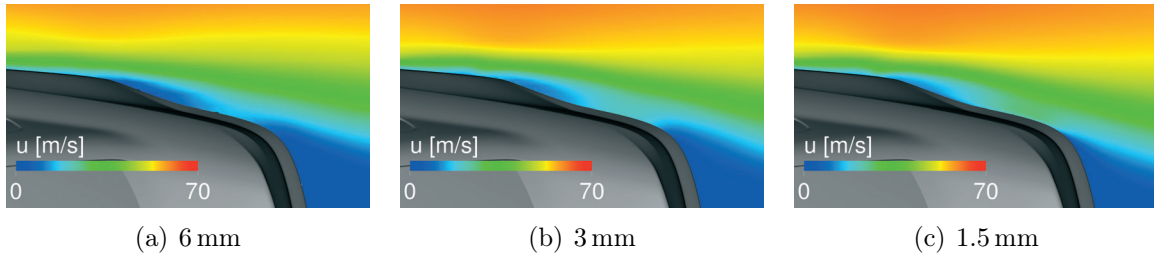
Figure 4.4: Axial velocity in a slice at $z = 0.14$ m for numerical grids with various surface resolutions.

Lateral inflow into the wake region around the leeward rear edge characterizes the flow around a realistic passenger car geometry at constant yaw according to previous investigations [48, 70, 107]. This establishes only in case of the standard grid with 1.5 mm resolution, compare Figure 4.5. For 3 mm and 6 mm resolution, the lateral flow into the wake is considerably less intense from the leeward side. In turn, surface pressures at the windward rear side of the vehicle increase with decreasing cell size of the numerical grid. As a result, the total side force increases and the absolute value of the yaw moment decreases, as shown in Table 4.3.

To conclude, numerical results are closest to experimental data for the highest investigated resolution of the boundary layer at the vehicle surface. Though this finding could be expected, it is shown that the coarse resolution is not even capable of qualitatively

(a) 6 mm   (b) 3 mm   (c) 1.5 mm
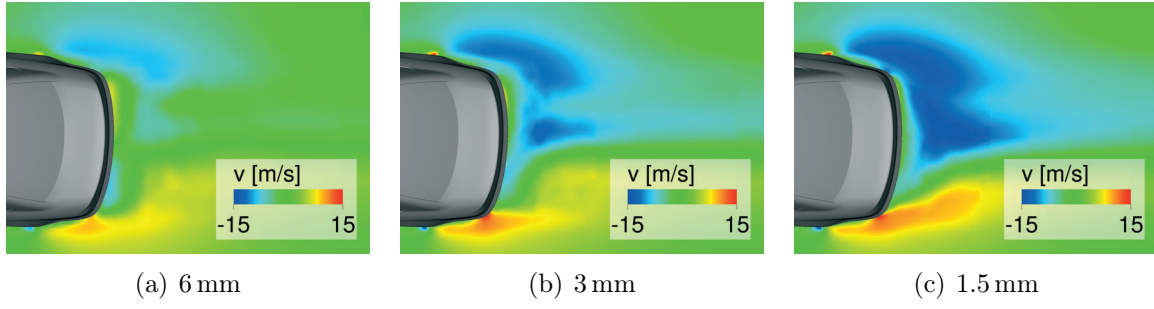
Figure 4.5: Lateral velocity in a slice at $z = 0.14$ m for numerical grids with various surface resolutions.

predicting the characteristic flow topology at constant yaw $\beta \neq 0$. At the same time, better resolution prolongs computation times. Using the standard numerical grid, non-dimensional wall distances of the first cell center in wall-normal direction are around 120 in average, compare Figure 4.6. Even for this grid, y^+ is fairly large regarding a correct application of wall models. A further reduction of the cell size at the surface is, however, not feasible, since the required computational power will not be industrially applicable within the next years. Thus, this approach is beyond the scope of this work.
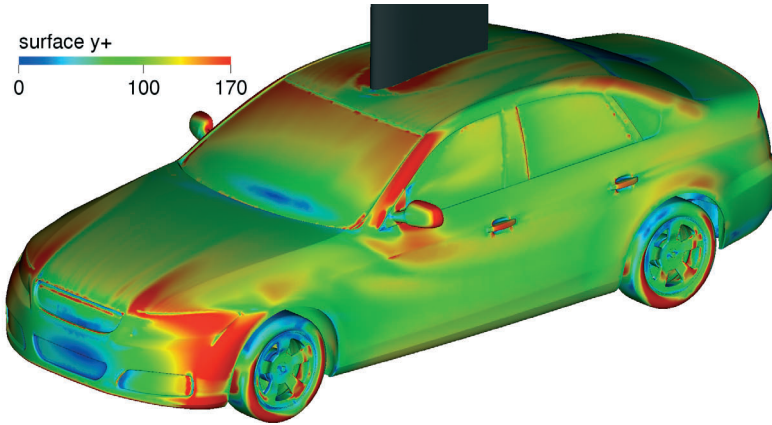
Figure 4.6: Non-dimensional wall distance for standard numerical grid at $\beta = $ -3.3°.

4.2.2 Variation of refinement zones

Next, local refinement zones of the standard numerical grid are varied. In order to decrease the computational effort, this study is performed in 1:1 scale at constant yaw $\beta = +3.3°$. As the Reynolds number has to be kept constant, the inlet velocity is reduced to U=105 km/h. A transfer simulation with identical numerical setups for 1:2 scale and 1:1 scale proved maximum differences of 0.004 for the three force coefficients and 0.002 for three the moment coefficients, which is within the interval of reproducibility errors of the numerical method. So, the validity of a transfer from model to full scale is attested.

In total, six variants of the standard numerical grid were tested, which are denoted as Grid 1 to Grid 6 in the following. The standard numerical grid has a minimum cell size of 3 mm at the vehicle surface in full scale. In accordance with the standard grid, Grid 1

has also three cell layers with 3 mm size around the vehicle surface. In contrast, the next nine cell layers with 6 mm size are replaced by a separately defined refinement region. This region basically corresponds to an offset of the vehicle surface, but it is enlarged in vertical direction to the ground. So, Grid 1 has in total three offset regions for the local definition of 6 mm, 12 mm and 24 mm cells. Compared to the standard grid, the length of these offset regions is increased for Grid 1 and Grid 2 and the width is additionally increased for Grid 3. The exact sizes of the offset regions of the grids are summarized in Table 4.4.

Table 4.4: Relative length L_{rel}, width B_{rel} and height H_{rel} of offset regions with respect to vehicle length, width and height for various grid variants.

Grid	6 mm Offset Region			12 mm Offset Region			24 mm Offset Region		
	L_{rel}	B_{rel}	H_{rel}	L_{rel}	B_{rel}	H_{rel}	L_{rel}	B_{rel}	H_{rel}
Standard	1.01	1.03	1.02	1.15	1.14	1.24	1.36	1.44	1.34
Grid 1	1.20	1.05	1.06	1.30	1.22	1.15	1.45	1.55	1.29
Grid 2	1.27	1.05	1.06	1.60	1.22	1.15	1.97	1.55	1.29
Grid 3	1.27	1.22	1.06	1.60	1.41	1.15	1.97	1.55	1.29

Grid 4, Grid 5 and Grid 6 are all based on Grid 3. Grid 4 locally resolves the strut surface and a certain volume downstream of strut with 6 mm cells. The lower, straight part of the strut is resolved with 3 mm cells in Grid 5. Finally, the complete volume between the vehicle and the ground is resolved with 3 mm cells in Grid 6. The resulting amounts of cell and surface elements are summarized in Table 4.5.

Table 4.5: Characteristics of various numerical grids at full scale.

	Cell Elements	Surface Elements
Standard Grid	37.8 M	7.4 M
Grid 1	78.6 M	7.5 M
Grid 2	83.8 M	7.5 M
Grid 3	94.2 M	7.6 M
Grid 4	120.7 M	7.7 M
Grid 5	94.0 M	8.5 M
Grid 6	125.4 M	8.0 M

In order to assess the dependency of numerical results on these computational grids, aerodynamic loads at $\beta = +3.3°$ are compared with experimental data in Table 4.6. According to the results, substantial discrepancies occur between experimental results and all grid variants for that yaw position. The reason therefore is more complex and is dealt with in the next chapter. Still, the side force, roll and yaw moment values computed for the standard grid are closest to experimental results. Drag force, down force and pitching moment are predicted similarly for all grid variants, which is of secondary relevance in

this context. So, the standard numerical grid is generally best suited according to these results.

Table 4.6: Aerodynamic loads at $\beta = +3.3°$ using various computational grids.

Grid	C_x	C_y	C_z	C_{M_x}	C_{M_y}	C_{M_z}
Experiment	0.291	-0.178	-0.003	0.021	-0.130	0.019
Standard Grid	0.270	-0.134	-0.117	0.011	-0.140	0.038
Grid 1	0.278	-0.110	-0.109	0.004	-0.149	0.047
Grid 2	0.278	-0.116	-0.110	0.006	-0.148	0.047
Grid 3	0.275	-0.111	-0.109	0.005	-0.146	0.050
Grid 4	0.260	-0.118	-0.106	0.007	-0.146	0.046
Grid 5	0.260	-0.118	-0.106	0.007	-0.146	0.046
Grid 6	0.277	-0.117	-0.098	0.006	-0.151	0.048

According to Table 4.6, side force and yaw moment significantly increase when comparing all other grid variants to the standard grid. Due to the differently resolved flow underneath the underfloor and behind the vehicle rear, the total and static pressure distribution in the wake flow field differ. Compared to the standard grid, the total pressure losses expand towards the ground for Grid 1, see Figure 4.7. This is similar for the other five grid variants. The result is an asymmetric static pressure distribution in the wake region, where a high pressure region tends to establish behind the windward, right rear corner. The one-sided pressure peak is more evident for Grid 1 through Grid 6 than for the standard grid (see Figure 4.7). The windward high pressure peak prohibits leeward inflow and provokes windward inflow, instead. Thus, the surface pressure is increased on the leeward and decreased on the windward rear side. As a result, the absolute value of the side force is decreased and the yaw moment is increased, which exactly matches the loads presented in Table 4.6.

Summing up, variations between Grid 1 and Grid 6 are of minor importance. Apparently, aerodynamic loads are insensitive to higher and spatially extended grid resolution of the wake flow and the flow around and behind the strut. In contrast, reducing the resolution between the underfloor and the ground from 12 mm to 6 mm changes the loads significantly. Surprisingly, a further refinement of the mesh in this area using a cell size of 3 mm (Grid 6) only changes little. In the end, the standard grid gives best results for side force, roll and yaw moment, since the windward high pressure peak in the wake flow is less distinct. Therefore, the results presented in the following chapter are based on the standard numerical grid.

(a) $C_{p,tot}$, Standard Grid

(b) $C_{p,tot}$, Grid 1

(c) C_p, Standard Grid

(d) C_p, Grid 1
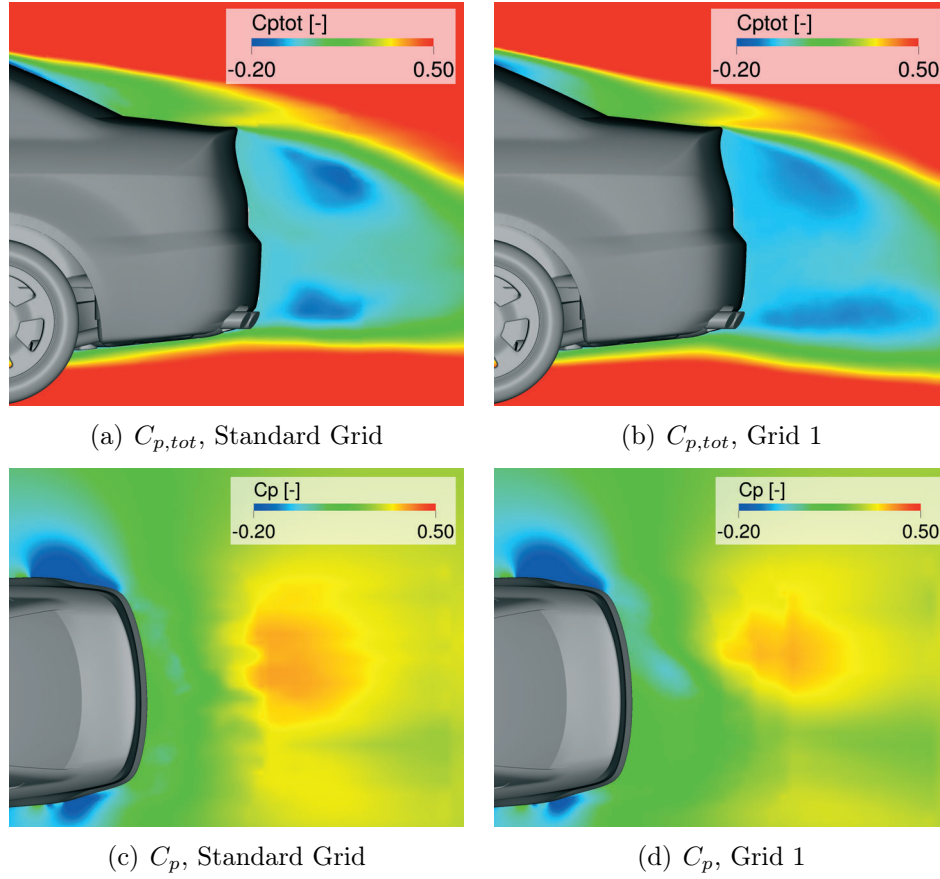
Figure 4.7: Total and static pressure in a slice at $y = 0$ and $z = 0.14\,\mathrm{m}$ for the standard numerical grid and Grid 1 at $\beta = +3.3°$.

4.3 Results

4.3.1 Constant yaw angle

4.3.1.1 Loads

The aerodynamic forces and moments acting on the vehicle during constant crossflow at $\beta = +3.3°$ and $\beta = $ -3.3° from experiment and simulation are summarized in Table 4.7. Table 4.8 shows the differences of aerodynamic loads from simulation and experiment on absolute scale, whereas relative differences are presented in Table 4.9.

Following from numerical and experimental results, drag force C_x, down force C_z and pitching moment C_{M_y} exhibit very small differences for a change from +3.3° to -3.3° yaw. The drag force is underrated by the simulation by around 6%. The down force is computed roughly 0.100 larger than measured in the experiment. So, the simulation completely failed in its attempt to predict the vertical force component. The pitching moments differ by 0.010 (8%) and 0.016 (13%) for $\beta = +3.3°$ and $\beta = $ -3.3°, respectively.

Table 4.7: Aerodynamic loads during constant yaw.

	+3.3°		-3.3°		Amplitude	
	Exp.	Sim.	Exp.	Sim.	Exp.	Sim.
C_x	0.291	0.270	0.298	0.283	-	-
C_y	-0.178	-0.134	0.214	0.226	0.196	0.181
C_z	-0.003	-0.117	-0.006	-0.096	-	-
C_{M_x}	0.021	0.011	-0.035	-0.036	0.028	0.024
C_{M_y}	-0.130	-0.140	-0.125	-0.141	-	-
C_{M_z}	0.019	0.038	-0.016	-0.020	0.018	0.029

Table 4.8: Difference between aerodynamic loads from simulation and experiment during constant yaw.

Sim.-Exp.	+3.3°	-3.3°	Amplitude
C_y	+0.044	+0.012	-0.015
C_{M_x}	+0.010	-0.001	-0.004
C_{M_z}	+0.019	-0.004	+0.011

The changes of side force C_y, roll moment C_{M_x} and yaw moment C_{M_z}, however, are much larger on absolute scale and hence much more important regarding vehicle dynamics during crosswind gusts. Therefore, it is focused on these parameters. According to Tables 4.8 and 4.9, these loads are fairly well predicted at β = -3.3°, whereas the numerical results deviate largely from experimental data at β = +3.3°. Surprisingly, the wrong numerical prediction at β = +3.3° affects the yaw moment to a larger extent than the side force.

Table 4.9: Relative difference between aerodynamic loads from simulation and experiment during constant yaw.

(Sim.-Exp.)/Exp.	+3.3°	-3.3°	Amplitude
C_y	+25%	+6%	-8%
C_{M_x}	+48%	-3%	-14%
C_{M_z}	+100%	-25%	+61%

Besides, the absolute values of aerodynamic loads from numerical simulations at β = +3.3° and β = -3.3° differ. In other words, the curve of numerical loads versus positive and negative yaw angles exhibits a significant asymmetry. Such an asymmetric behavior is also found in the experiment – however, to a smaller extent.

4.3.1.2 Characterization of wake flow field

The wake topology at constant cross flow was characterized in detail by Theissen et al. [108], whose findings are schematically illustrated in Figure 1.10. According to their results, the wake topology is mainly characterized by a region with high lateral velocity entering from the leeward rear side approximately at the height of the rear lights. Therefore, Figure 4.8 shows iso-surfaces of the lateral velocity $v = \pm 10\,\text{m/s}$ behind the vehicle rear.

(a) $\beta = +3.3°$

(b) $\beta = $ -3.3°
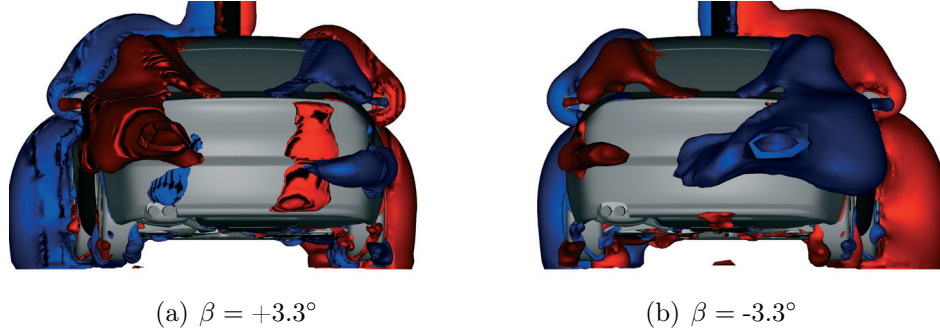
Figure 4.8: Iso-surfaces of $v = +10\,\text{m/s}$ (red) and $v = $ -10 m/s(*blue*).

According to Figure 4.8(b), significant leeward inflow into the wake region is found in the simulation at -3.3° yaw. In contrast, the leeward inflow is less evident at +3.3° yaw, see Figure 4.8(a). This becomes even more obvious by investigating a horizontal slice at $z = 0.2\,\text{m}$, presented in Figure 4.9. Strong leeward inflow appears at $\beta = $ -3.3° stretching out to the windward rear corner. Thus, windward flow is prevented from entering the wake region close to the surface, compare Figure 4.9(b). At $\beta = +3.3°$, however, windward and leeward inflow are similarly strong and are not directly attached to the vehicle back surface. At $z = 0.2\,\text{m}$ fluid at the vehicle back surface is actually moving laterally from the center towards both rear corners.

(a) $\beta = +3.3°$

(b) $\beta = $ -3.3°
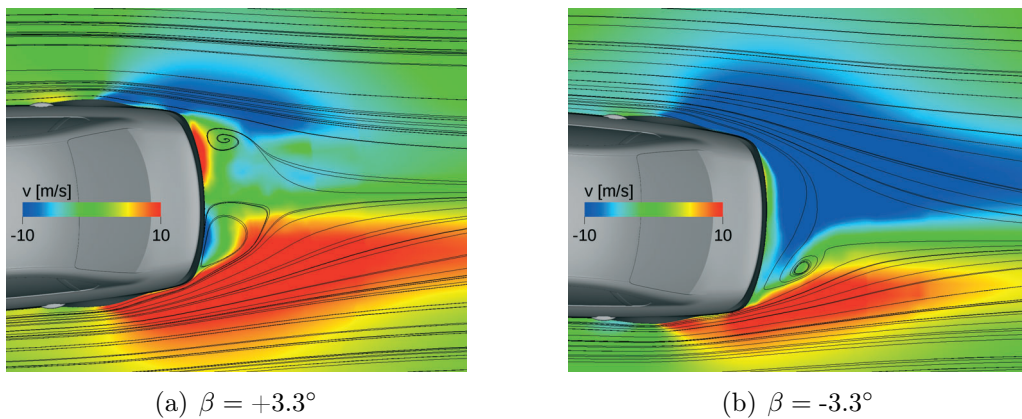
Figure 4.9: Lateral velocity in a slice at $z = 0.2\,\text{m}$.

Summing up, lateral flow entering the wake region from the leeward side appears. However, different intensities of the leeward inflow at +3.3° and -3.3° yaw are observed in the numerical simulation. Experimental fluid data do not exist, which may be used to validate the intensity of the leeward inflow into the wake region at constant yaw $\beta = \pm 3.3°$. Still,

these results serve as a first evidence for the asymmetric load behavior at positive and negative yaw angles found in the previous section from numerical simulations.

4.3.1.3 Surface pressures

Next, surface pressures from experiment and simulation are analyzed in order to study the background of steady aerodynamic loads as they appear in the simulation and in the experiment. Unfortunately, pressure tappings were mounted only at the right vehicle side, which does not allow to validate pressure differences between left and right vehicle side.
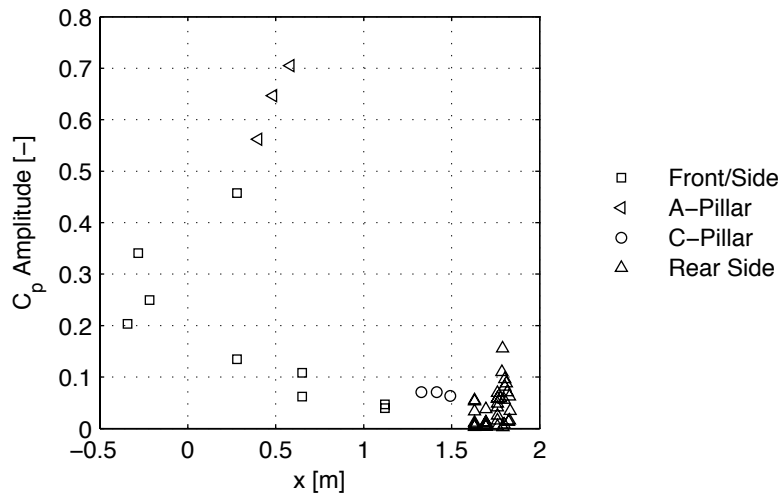
Figure 4.10: Steady pressure difference between $\beta = +3.3°$ and $\beta = $ -3.3° versus vehicle length from simulation.

Figure 4.10 shows surface pressure amplitudes for a quasi-steady change from $\beta = +3.3°$ to $\beta = $ -3.3° from the numerical simulation. In accordance to the experimental results presented in Figure 3.4, surface pressure changes are largest at the front and particularly at the a-pillar of the vehicle. The pressure changes at the rear are very small. In Figure 4.11, the pressure amplitude predicted by the simulation for a quasi-steady change from $\beta = +3.3°$ to $\beta = $ -3.3° is subtracted from the experimental pressure amplitude. So, deviations from zero denote differences between numerical and experimental results. Positive values indicate underestimation, negative values overestimation of the pressure amplitude by the numerical simulation. According to Figure 4.11, surface pressure amplitudes at the right rear side deviate most severely from experimental results. In average, pressure amplitudes are underestimated there, which will be discussed in detail later in this section. In contrast, pressure amplitudes at the vehicle front tend to be overestimated by the simulation – except at $x \approx 0.3\,\mathrm{m}$, which is also explained separately. All other surface pressure measurements agree fairly well with experimental data.

Pressure changes at the right vehicle side during a change of yaw from +3.3° to -3.3° are now interpreted as a change from windward to leeward side. This is certainly true at the front of the vehicle, where the flow instantaneously reacts to a change of the oncoming flow. According to Figure 4.11, the pressure difference between windward and leeward side is overrated at the front of the vehicle and at the a-pillar, which pushes the vehicle

from windward to leeward thus increasing the total yaw moment in the simulation. This occurs at negative and positive yaw and is a first evidence for a numerical exaggeration of the yaw moments at $\beta = +3.3°$ and $\beta = -3.3°$ observed (see Table 4.7). However, these findings at the vehicle front cannot explain why the numerical exaggeration is more pronounced at $\beta = +3.3°$.
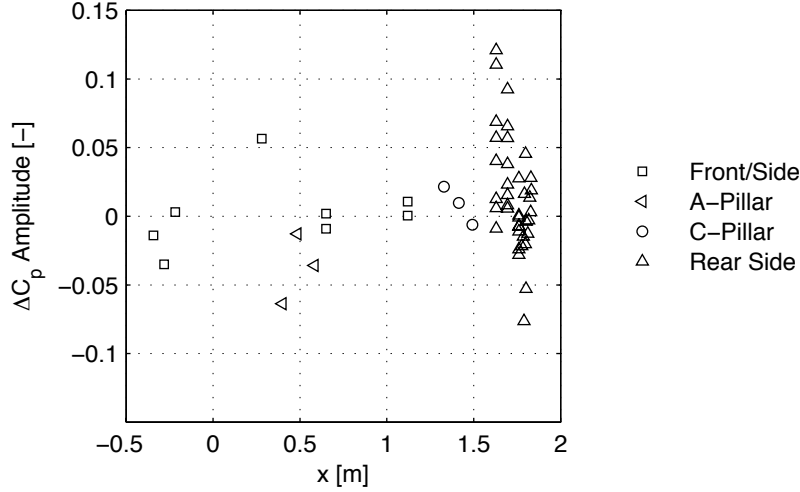
Figure 4.11: Difference between quasi-steady pressure amplitudes from experiment and simulation versus vehicle length.

(a) $\beta = +3.3°$, Windward Side   (b) $\beta = -3.3°$, Leeward Side
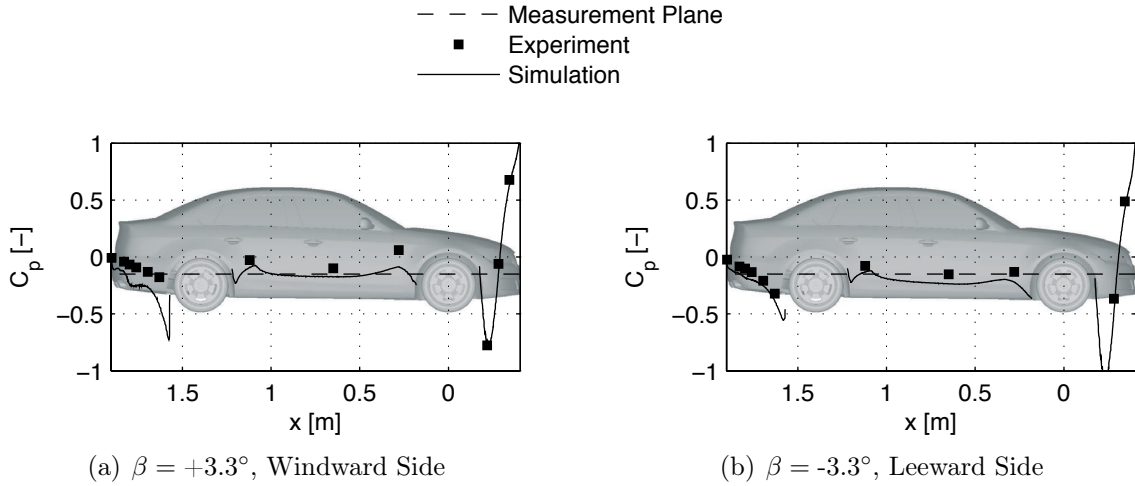
Figure 4.12: Steady pressures at windward (a) and leeward (b) right vehicle side at $z = 65\,\text{mm}$.

The underestimated pressure amplitude at the vehicle front at $x \approx 0.3\,\text{m}$ in Figure 4.11 corresponds to a probe behind the front wheel house at $z = 65\,\text{mm}$. Figure 4.12 confronts the static pressure distribution along the right vehicle side at $z = 65\,\text{mm}$ (outlined in Figure 3.2 and in the background of Figure 4.12) from simulation with single experimental pressure measurements for $\beta = \pm 3.3°$. Obviously, the surface pressure right behind the front wheel house is underestimated by the simulation for both yaw positions, which is due to a lack of momentum in this flow area and hence a delayed flow reattachment in the simulation. Behind the rear wheel house, the pressure recovery is captured in good

agreement with experimental data for β = -3.3°, whereas the pressure recovery is largely underestimated for β = +3.3°.

Figure 4.13 outlines the surface pressure distribution on the rear vehicle side at +3.3° and -3.3° yaw. According to the experimental procedure, pressure measurements in the simulation are taken at the positions indicated with black points and interpolated in the area between. It is confirmed that the flow separation and hence the pressure recovery behind the rear wheel house at the windward side is not captured correctly for +3.3° yaw, whereas it is predicted fairly well at the leeward side for -3.3° yaw. At -3.3° yaw, the numerical results display similar surface pressure characteristics as in the experiment, namely a distinct low pressure region around the rear lights, where leeward inflow decreases static pressure. The average surface pressure level within the measurement square also matches experimental results for β = -3.3°. On the other hand, the average pressure within the measurement square is predicted incorrectly by the simulation for the windward side at β = +3.3°. There, the average pressure measured in the experiments is much higher, whereas the average pressure in the numerical simulation is similar to β = -3.3°.

(a) β = +3.3°   (b) β = -3.3°
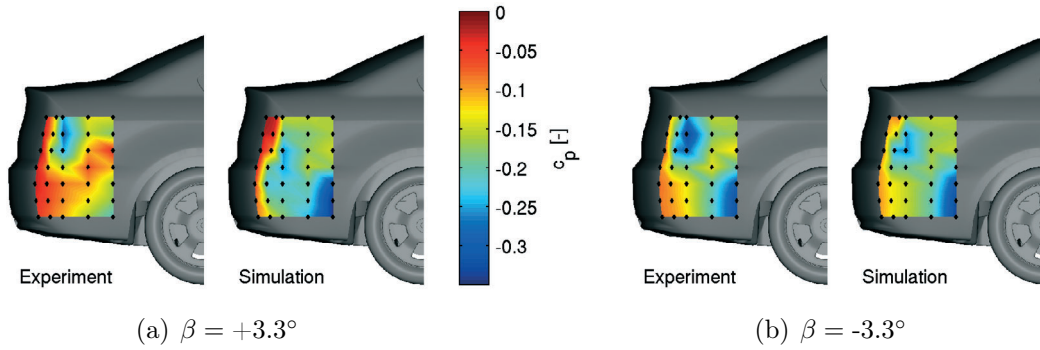
Figure 4.13: Steady pressure distributions on windward (a) and leeward (b) rear side of the vehicle from experiment and simulation.

From this, it cannot be concluded, if the failed prediction of surface pressures at the rear is generally attributed to the windward side or to the position at +3.3° yaw. To this end, a comparison of surface pressure distributions on right and left rear side follows in Figure 4.14. Data are taken from numerical results, since pressure tappings were only mounted on the right vehicle side in the experiments. Most interesting in this context is a comparison of left and right vehicle rear side at each yaw position. Apparently, windward surface pressures are higher than leeward pressures at β = -3.3°, which is inverted at β = +3.3°. The difference between windward and leeward pressure is, however, not only negative at β = +3.3°, but its absolute value even increases compared to at β = -3.3°. Consequently, the behavior at β = +3.3° is in contrast to experimental findings (compare Figure 4.13) and to the unsteady mechanism proposed by Theissen [107] (compare Figure **??**).

Following these findings, the direction of the lateral force due to pressure differences at the rear at β = +3.3° is calculated incorrectly. The total yaw moment thus increases and the absolute value of the side force decreases. Together with the above mentioned overestimated yaw moment contribution from the front this explains the substantial deviations from experimental steady loads presented in Table 4.7.

(a) Leeward (+3.3°)   (b) Windward (+3.3°)

Static Pressure [Cp]

-0.3000   -0.2500   -0.2000   -0.1500

(c) Windward (-3.3°)   (d) Leeward (-3.3°)
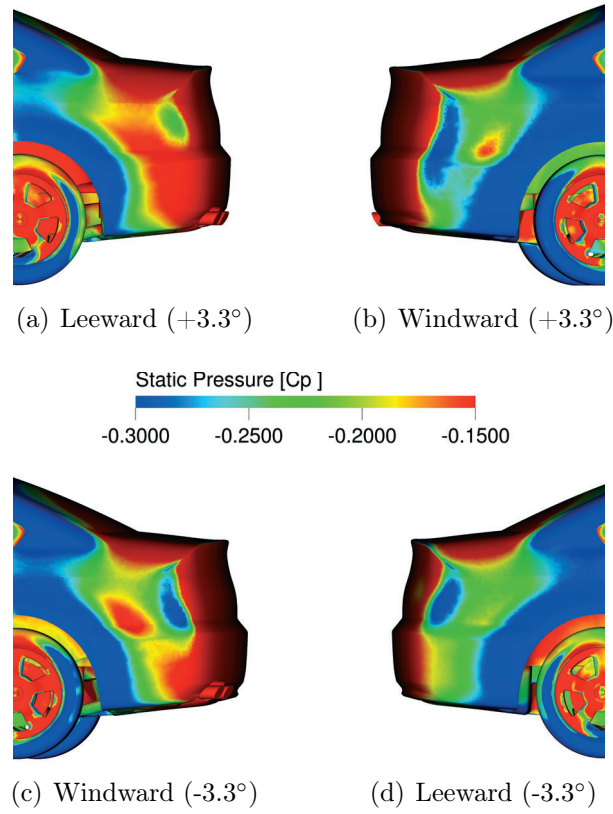
Figure 4.14: Surface pressure distributions on windward and leeward rear side of the vehicle for $\beta = \pm 3.3°$ from numerical simulation.

4.3.1.4 Summary of steady results

According to the results presented, leeward inflow is predicted by the numerical simulation to be less intense at $\beta = +3.3°$ than at $\beta = $ -3.3°, whereas it is similarly intense in the experiment. As a result, the surface pressure difference between left and right rear side at $\beta = +3.3°$ is inverted compared to the experiment. Hence, steady loads at $\beta = +3.3°$ are computed erroneously. In contrast, aerodynamic loads at $\beta = $ -3.3° are much closer to experimental data. Finally, the yaw moment amplitude for a quasi-steady change from +3.3° to -3.3° yaw is overestimated by 61% and the side force amplitude is underestimated by 8%.

4.3.2 Transient change of yaw angle

4.3.2.1 Loads

In the following, unsteady aerodynamic loads from simulation and experiment are compared. Figure 4.15 outlines their developments for the standard oscillation case. Quasi-steady transients are added for side force, roll and yaw moment, derived by fitting a sinusoidal curve to the peak values encountered during steady measurements. The axis scaling covers identical ranges within the force and the moment plots. It is reminded that

experimental results are averaged over more than 400 oscillations, whereas numerical results are only averaged over five oscillations. The oscillation period for phase-averaged results is defined according to Figure 3.3.
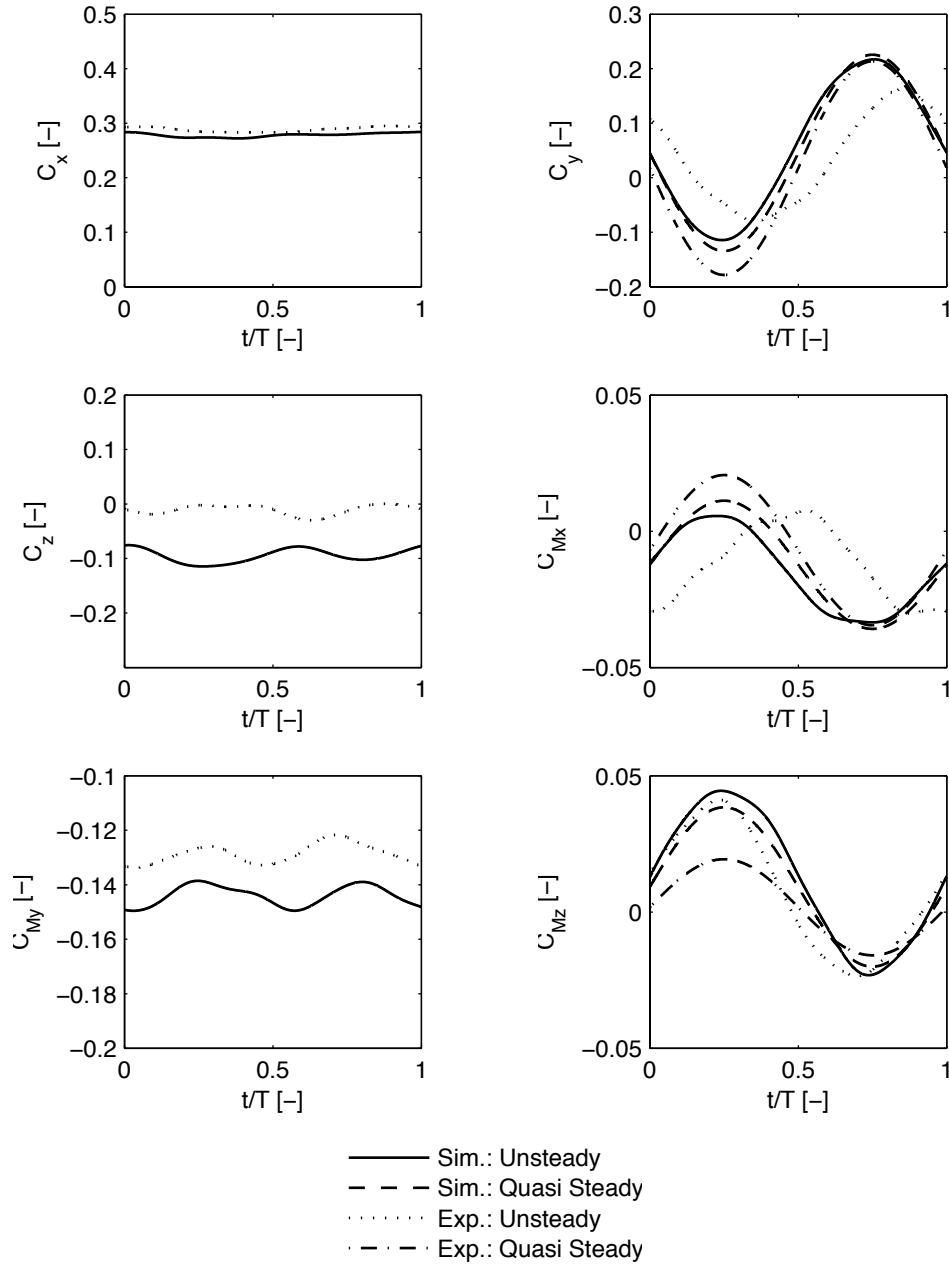
Figure 4.15: Quasi steady and unsteady aerodynamic loads from experiment and simulation at $f = 2\,\text{Hz}$, $\beta = \pm 3.3°$.

In accordance with quasi-steady developments, the changes of drag force, lift force and pitching moment are marginal compared to the changes of side force, roll moment and yaw moment during an unsteady change of yaw between $\pm 3.3°$. By absolute numbers, maximum changes are ΔC_x=0.018, ΔC_z=0.060 and ΔC_{M_y}=0.022. The different levels of their unsteady experimental and numerical transients correspond to the numerical miscalculation at steady flow conditions.

First, the focus is within unsteady load amplitudes. Table 4.10 outlines half peak-to-peak amplitudes of unsteady load transients and opposes quasi-steady amplitudes presented in the previous section. Table 4.11 and Table 4.12 give absolute and relative differences between aerodynamic load amplitudes from simulation and experiment. According to the results, the unsteady side force amplitude is overestimated by 0.045 or 37%, whereas the unsteady amplitudes of roll moment and yaw moment are predicted very accurately.

Table 4.10: Half of peak-to-peak load amplitudes during unsteady and quasi-steady change of yaw.

	Unsteady		Quasi Steady	
Amp.	Exp.	Sim.	Exp.	Sim.
C_y	0.121	0.166	0.196	0.181
C_{M_x}	0.019	0.020	0.028	0.024
C_{M_z}	0.032	0.034	0.018	0.029

Table 4.11: Difference between unsteady load amplitudes from simulation and experiment.

Sim.-Exp.	Unsteady	Quasi Steady
C_y	+0.045	-0.015
C_{M_x}	+0.001	-0.004
C_{M_z}	+0.002	+0.011

Table 4.12: Relative difference between unsteady load amplitudes from simulation and experiment.

(Sim.-Exp.)/Exp.	Unsteady	Quasi Steady
C_y	+37%	-8%
C_{M_x}	+5%	-14%
C_{M_z}	+6%	+61%

The ratios of unsteady to quasi-steady amplitudes are outlined in Table 4.13. The ratio is below one for side force and roll moment, and above one for the yaw moment. Hence, the general characteristics of unsteady phenomena are captured likewise by the experiment and the numerical simulation: The unsteady yaw moment exceeds its quasi-steady approximation, whereas the unsteady side force and roll moment are smaller than their quasi-steady counterparts. However, quantitative discrepancies occur. According to Table 4.13, the side force ratio is overestimated by the numerical simulation, which is predominantly due to a wrong numerical prediction of the unsteady amplitude, see Table 4.12. As opposed to this, the yaw moment ratio is underestimated due to a wrong numerical prediction of the steady amplitude.

Table 4.13: Ratio of unsteady to quasi-steady load amplitudes.

Amp. Ratio	Exp.	Sim.
C_y	0.62	0.92
C_{M_x}	0.68	0.83
C_{M_z}	1.83	1.16

Table 4.14: Phase lag of unsteady against quasi-steady load amplitudes.

Phase $\Delta t/T$	Exp.	Sim.
C_y	0.06	-0.01
C_{M_x}	0.11	-0.03
C_{M_z}	-0.02	0.00

Besides, numerical and experimental results exhibit discrepancies regarding the phase lag of unsteady to quasi-steady load transients. In the experiment, the unsteady yaw moment is slightly lagging behind the model motion. The side force and particularly the roll moment, however, are running ahead of the vehicle motion and thus their quasi-steady developing. These characteristic phase lags are not reproduced adequately by the numerical simulation, as outlined in Figure 4.15 and summarized in Table 4.14.

4.3.2.2 Wake flow field

(a) $\beta = +3.3°$ (b) $\beta = -3.3°$
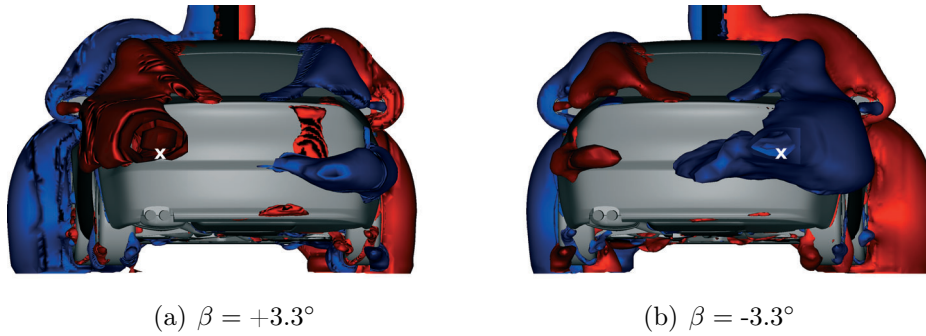
Figure 4.16: Iso-surfaces of $v = +10\,\text{m/s}$ (red) and $v = -10\,\text{m/s}$ (blue) at $t/T = 0.25$ (a) and $t/T = 0.75$ (b). White crosses indicate probe positions.

Next, the wake flow field is investigated following the analysis at constant yaw. Figure 4.16 illustrates the iso-surfaces of lateral velocity at t/T=0.25 and t/T=0.75, where $\beta = +3.3°$ and $\beta = -3.3°$, respectively. At these instants the wake flow field exhibits similar characteristics as for constant yaw (compare Figure 4.8). At $\beta = -3.3°$ dominant lateral inflow into the wake region around the leeward rear corner appears, whereas at $\beta = +3.3°$ the leeward inflow is considerably less intense and a certain amount of windward inflow appears, instead. From previous investigations of Theissen [107] and from experimental results, it is rather expected that differences appear between steady and unsteady conditions, since the wake flow was proved to react with a significant time delay to a change of the oncoming flow.

In order to gain further insight into the unsteady development of the wake flow field, the lateral velocity at a single point just downstream of the right rear corner is assessed. In the experiment a hot wire probe was positioned at $x = 1.926\,\text{m}$, $y = 0.248\,\text{m}$, $z = 0.220\,\text{m}$, indicated with a white cross in Figure 4.16(b). A periodic behavior of the lateral velocity that exhibits a time delay $\Delta t/T \approx 0.15$ relative to the model motion was reported by

Theissen et al. [107, 111]. The same measurement is taken from numerical results and plotted together with its quasi-steady evolution and the experimental unsteady development in Figure 4.17(b). In the simulation, the lateral velocity at the right rear corner exhibits also periodic behavior and similar amplitude. However, the unsteady velocity change predicted by the simulation has a smaller time lag relative to the model motion ($\Delta t/T \approx 0.064$). Besides, the mean lateral velocity is only half of the experimental value, which means that the lateral inflow into the wake region is less developed at this location.

(a) Left Rear Corner (b) Right Rear Corner
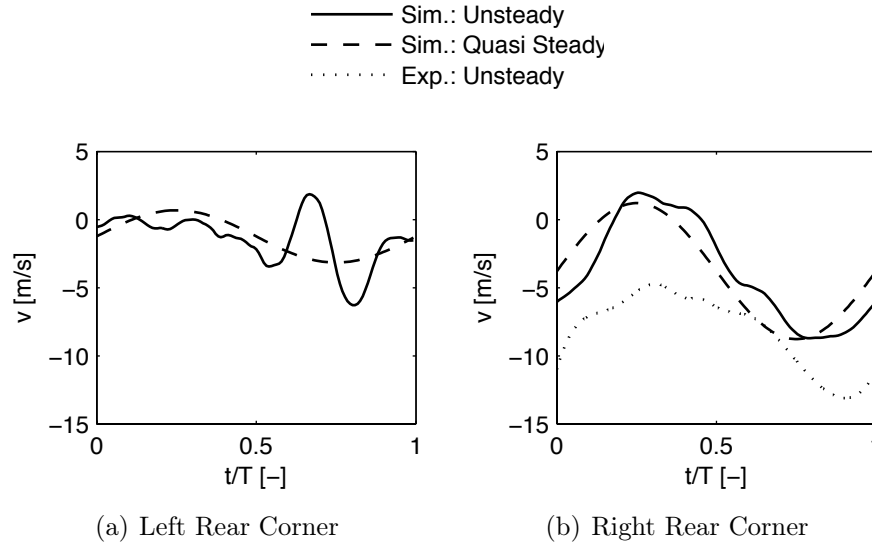
Figure 4.17: Evolution of lateral velocity at $x = 1.926 \, \text{m}$, $y = \pm 0.248 \, \text{m}$, $z = 0.220 \, \text{m}$ during oscillation with $f = 2 \, \text{Hz}$ and $\beta = \pm 3.3°$.

The situation changes when mirroring the probe to the left rear corner (see Figure 4.16(a)) in the simulation. There, the periodicity of the lateral velocity is weak and the mean value of the lateral velocity is small, even negative. From previous findings and experimental results, a positive mean value and a distinct positive maximum at t/T=0.25 would be expected. Unfortunately, experimental reference data are not available for the mirrored probe position.

The discrepancy between the development of left and right inflow into the wake region in the numerical results proves that the lateral inflow is only established at one rear side. In the numerical simulation the leeward inflow is well apparent at $\beta = +3.3°$ at the right rear, whereas it is weak at $\beta = -3.3°$ at the left rear. Experimental results indicate that the strength and the phase lag of the inflow at the right rear is underestimated by the simulation, but exhibits realistic oscillation amplitudes. At the left rear, however, the lateral inflow is even weaker and thus has negligible unsteady impact. All in all, a one-sided and hence asymmetric, but fluctuating lateral inflow into the wake flow field erroneously establishes in the numerical simulation.

Although the findings of Figure 4.17 are limited to a single point, they give an appropriate answer to the question, why the iso-surfaces of lateral velocity are similar in Figure 4.8 and Figure 4.16. Due to similar amplitudes and the small phase lags between unsteady and quasi-steady lateral velocity developments in the simulation, presented in Figure 4.17(a) and Figure 4.17(b), the wake flow characteristics at $\beta = +3.3°$ and $\beta = -3.3°$ are very similar for unsteady and quasi-steady conditions.

4.3.2.3 Surface pressures

For a deeper understanding of the discrepancies between unsteady aerodynamic loads from experiment and simulation, unsteady surface pressure developments are analyzed in the following. From experimental results it is known that unsteady pressure amplitudes encountered at the vehicle front are largest on absolute scale. This is confirmed by numerical results, see Figure 4.18.
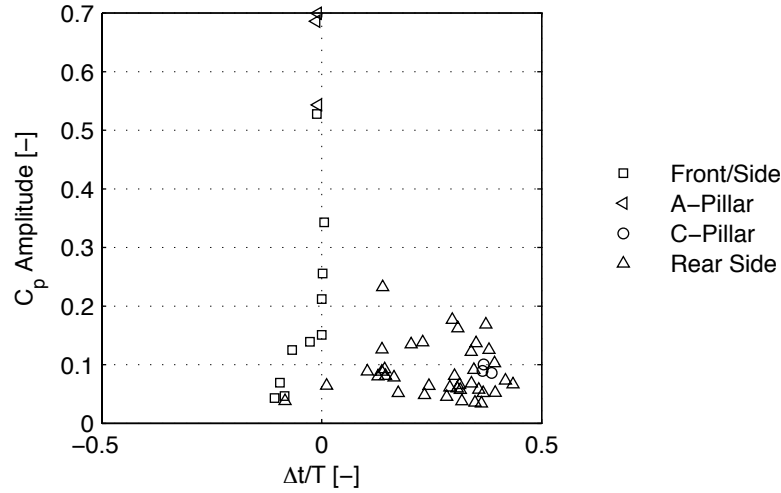
Figure 4.18: Unsteady pressure amplitude versus phase of unsteady against quasi-steady pressure transients.
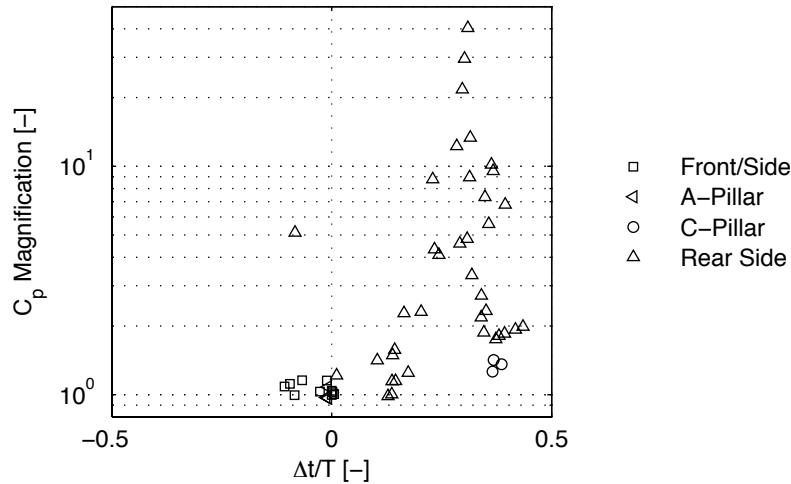
Figure 4.19: Unsteady magnification of quasi-steady pressure amplitude versus phase of unsteady against quasi-steady pressure transients.

Figure 4.19 outlines the ratio of unsteady to quasi-steady pressure amplitudes. According to Figure 4.19, pressure fluctuations at the rear of the vehicle are enhanced during transient yaw, whereas they are similar to quasi-steady flow conditions at the front. Besides, pressure changes at the vehicle front instantaneously follow the oncoming flow, whereas

pressure fluctuations at the rear of the vehicle feature a significant positive time lag. These results are in line with experimental findings outlined in Figure 3.6. So, the unsteady mechanism causing unsteady yaw moment overshoot is generally captured by the simulation, as well. However, some differences appear, which are assessed by subtracting unsteady pressure amplitudes and phase lags computed by the numerical simulation from the corresponding experimental values, see Figure 4.20.
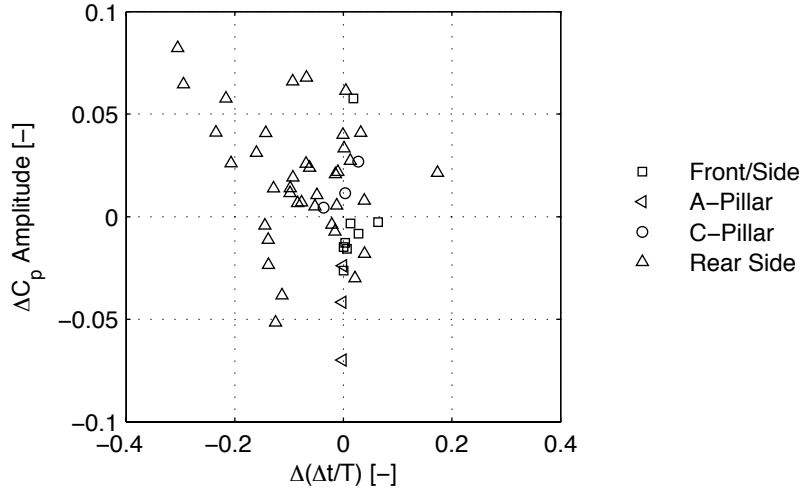
Figure 4.20: Difference between unsteady pressure amplitude and phase lag from experiment and simulation for various probe locations.

According to Figure 4.20, unsteady pressure amplitudes at the a-pillar, front and side are overestimated by the simulation. This coincides with numerical deficiencies during steady cross flow presented in Figure 4.11. As a consequence, the lateral force predicted by the simulation for the vehicle front overrates the total side force and yaw moment with respect to experimental results. At the rear, pressure amplitudes are underestimated and phase lags are predominantly overestimated by the simulation. Since the differences between unsteady experimental and numerical surface pressure signals are most distinct at the rear, these are studied more detailed in the following.
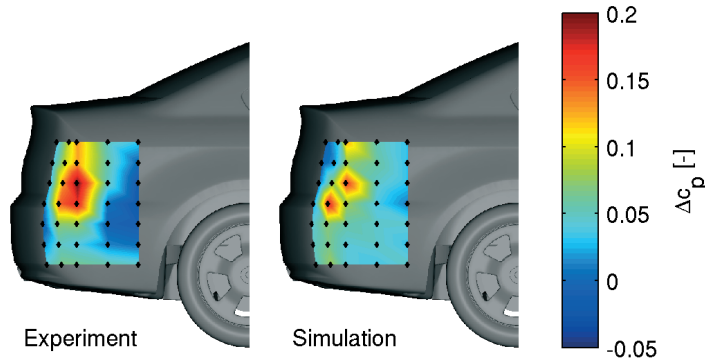
Figure 4.21: Difference between unsteady and quasi-steady pressure amplitude.

Figure 4.21 compares experimental and numerical results for differences between unsteady and quasi-steady surface pressure amplitudes at the rear. Positive differences denote larger unsteady pressure amplitudes. In the experiment, unsteady pressure amplitudes generally

exceed quasi-steady amplitudes, particularly close to the rear lights. The simulation predicts larger unsteady than quasi-steady pressure amplitudes on the vehicle rear side, as well, however, to a smaller extent than in the experiment.
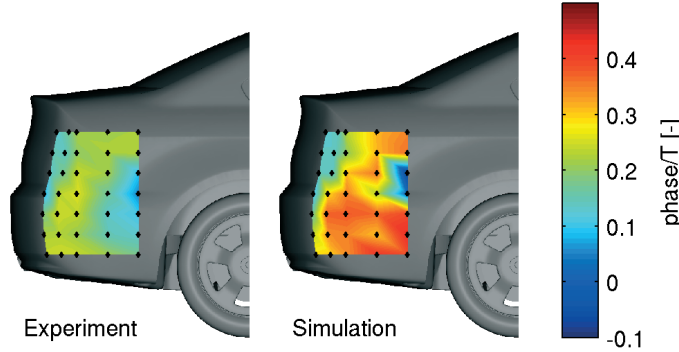
Figure 4.22: Phase lag of unsteady against quasi-steady pressure signal.

The phase lag of the unsteady to the quasi-steady pressure signals differ considerably from the experimental results, which is addressed in Figure 4.22. While the phase lags are relatively uniform in the experiment, they are more diverse in the simulation. To a large degree, the pressure transients are opposite in phase to their quasi-steady development.
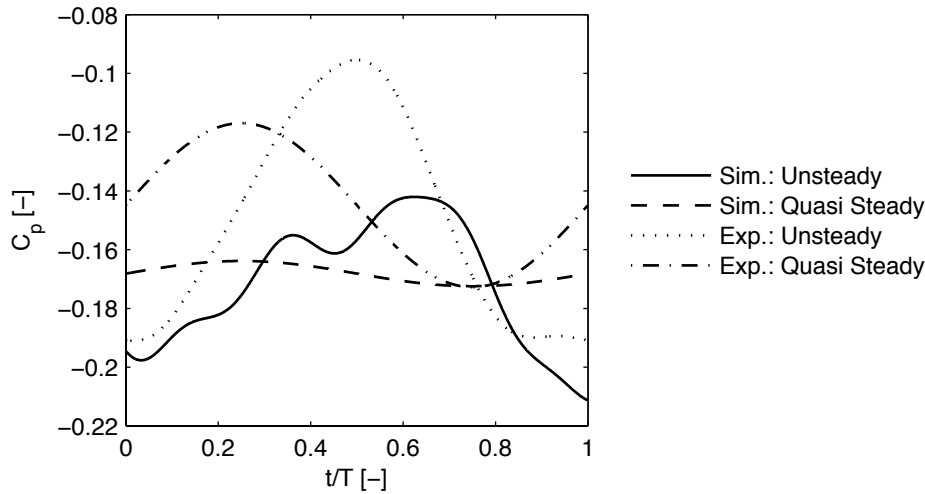
Figure 4.23: Mean of all periodic averaged pressure signals within the measurement plane at the rear side from experiment and simulation.

In order to assess the side force contribution of the vehicle rear, the average pressure signal of all probe locations at the rear side is analyzed. Figure 4.23 shows unsteady and quasi-steady transients from the experiment and the simulation. As mentioned previously, the quasi-steady mean pressure is well estimated at $\beta = $ -3.3° or $t/T = 0.75$, but strongly underestimated at $\beta = +3.3$° or $t/T = 0.25$. Hence, the quasi-steady pressure amplitude computed at the vehicle rear is very small. The unsteady pressure change in the simulation is, however, much larger and delayed. Still, it is significantly smaller than recorded in the experiments. In particular, the maximum is truncated compared to the experimental mean pressure signal. Although the mean phase lag is predicted correctly, the smaller unsteady amplitude indicates a smaller impact of unsteady pressure changes at the rear side in the numerical simulation.

4.3.2.4 Summary of results

Summing up, unsteady and steady pressure amplitudes are overestimated by the simulation at the vehicle front, which generally increases the total yaw moment with respect to experimental results. At the rear, leeward inflow into the wake field is sparse at $\beta = +3.3°$, since it is irrespective of the yaw position more distinct on the right side in the simulation. This does not correspond with the experiment. The steady pressure difference between left and right is thus inverted at the rear at $\beta = +3.3°$ compared to experimental results. For a quasi-steady change between $+3.3°$ and $-3.3°$ yaw, pressure changes at the rear are then underrated by the simulation, which results in an overestimation of the quasi-steady yaw moment amplitude of 61%.

During transient change of yaw, the lateral inflow around the right rear corner exhibits significant oscillations, which lead to pressure fluctuations at the rear vehicle surface. Since the magnitude of theses pressure fluctuations in the simulation is less than in the experiment and since oscillating lateral inflow around the left rear corner is mostly missing in the simulation, the overall unsteady impact at the vehicle rear is underestimated by the simulation. This means that the unsteady mechanism is considerably weakened.

Following from this, the unsteady yaw moment overshoot is less intense compared to the experiment. However, as the steady yaw moment was overestimated, the unsteady yaw moment finally predicted by the simulation is incidentally correct. As another consequence of the underestimated unsteady impact at the rear, the unsteady reduction of side force amplitude is less distinct in the simulation. Since the steady side force was calculated correctly, the unsteady side force is finally overestimated by the simulation. This corresponds exactly to the discrepancies between unsteady aerodynamic loads from experiment and simulation as presented in Table 4.12. So, the characteristics of unsteady loads as initially presented by Theissen [107] are qualitatively confirmed, but the unsteady impact is underestimated by the simulation.

4.3.3 Influence of geometric changes

From the above, deficiencies of the numerical simulation are mainly attributed to a different extent of lateral inflow into the wake region at $+3.3°$ and $-3.3°$ yaw. This deficit is most prominently expressed by diverging absolute values of steady yaw moments at these two yaw positions (see Table 4.9). Discrepancies between experimental and numerical loads prove that this asymmetric behavior only appears in the simulation. From the grid study presented in chapter 4.2, it is known that the asymmetry is not caused by a coarse grid resolution of the wake flow, of the flow around and downstream of the strut nor of the underfloor flow. Considering geometric asymmetries, the asymmetric behavior of the flow at $\beta = +3.3°$ and $\beta = -3.3°$ may only originate from the asymmetric strut or the asymmetric underfloor. All other geometry parts are fully symmetric to a plane at $y = 0$. Therefore, the sensitivity of the numerical simulation to changes of the asymmetric geometry parts is investigated. To this end, several simulations are performed in full scale at constant yaw $\beta = \pm 3.3°$.

4.3.3.1 Asymmetric and symmetric Strut

First, the asymmetric strut geometry is investigated. The scanned strut from the experiment is fully symmetric from the top of the vehicle roof up to $z = 939\,\text{mm}$, where its cross-section starts to grow (compare Figure 4.1). Further upward, the strut is asymmetric and exhibits maximum lateral deviations of $7\,\text{mm}$ between left and right surface. In total, the geometric asymmetry of the scanned strut geometry is weak and most prominent apart from the vehicle surface. In order to quantify the contribution of the asymmetric strut geometry to the asymmetric flow behavior in the wake field, a fully symmetric strut geometry is investigated in addition to the original strut. The fully symmetric strut corresponds to the original strut without the experimental casing and cables at the outside.

Table 4.15 compares the aerodynamic yaw moments computed for the two different strut geometries based on Grid 2. Yaw moments from the experiment are appended, whose absolute values differ only by 0.003 for $\beta = +3.3°$ and $\beta = $-3.3°. With the fully symmetric as well as the real, slightly asymmetric strut geometry, the absolute values of the steady yaw moments differ to a larger extent. Hence, asymmetric aerodynamic loads at +3.3° and -3.3° yaw are only fractionally caused by the slightly asymmetric shape of the strut above $z = 939\,\text{mm}$.

Table 4.15: Yaw moment coefficient C_{M_z} for symmetric and asymmetric strut geometry.

Method	Strut	+3.3°	-3.3°
Sim.	Symmetric	0.045	-0.024
Sim.	Asymmetric	0.047	-0.020
Exp.	Asymmetric	0.019	-0.016

These findings are confirmed by the representation of the lateral inflow into the wake region, see Figure 4.24. The flow topology is very similar for both strut geometries. A dominant inflow from the right vehicle rear establishes irrespective of the strut asymmetry. Leeward inflow from the left side at +3.3° yaw is missing in both simulations.

4.3.3.2 Flat and detailed underfloor

As a consequence of the preceding investigation, the asymmetric underfloor of the DrivAer notchback must be responsible for the discrepancies between aerodynamic loads at +3.3° and -3.3° yaw in the simulation. For this reason, simulations with a fully symmetric and a flat underfloor are compared with the standard underfloor simulation. All three underfloor geometries are displayed in Figure 4.25. The symmetric underfloor is generated by mirroring the original, asymmetric DrivAer underfloor from $y \geq 0$ to $y < 0$ omitting the exhaust system.

(a) Symmetric Strut, $\beta = +3.3°$ (b) Symmetric Strut, $\beta = $ -3.3°

(c) Asymmetric Strut, $\beta = +3.3°$ (d) Asymmetric Strut, $\beta = $ -3.3°
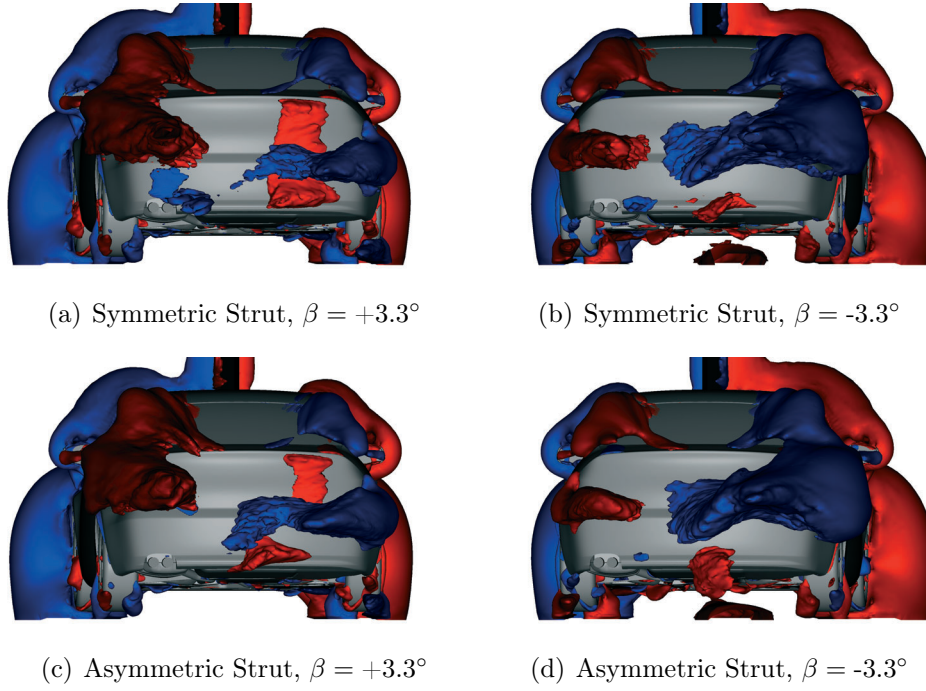
Figure 4.24: Iso-surfaces of $v = +5\,\text{m/s}$ (red) and $v = $ -5 m/s (blue) for a fully symmetric and an asymmetric strut geometry.

(a) Asymmetric Underfloor   (b) Symmetric Underfloor   (c) Flat Underfloor
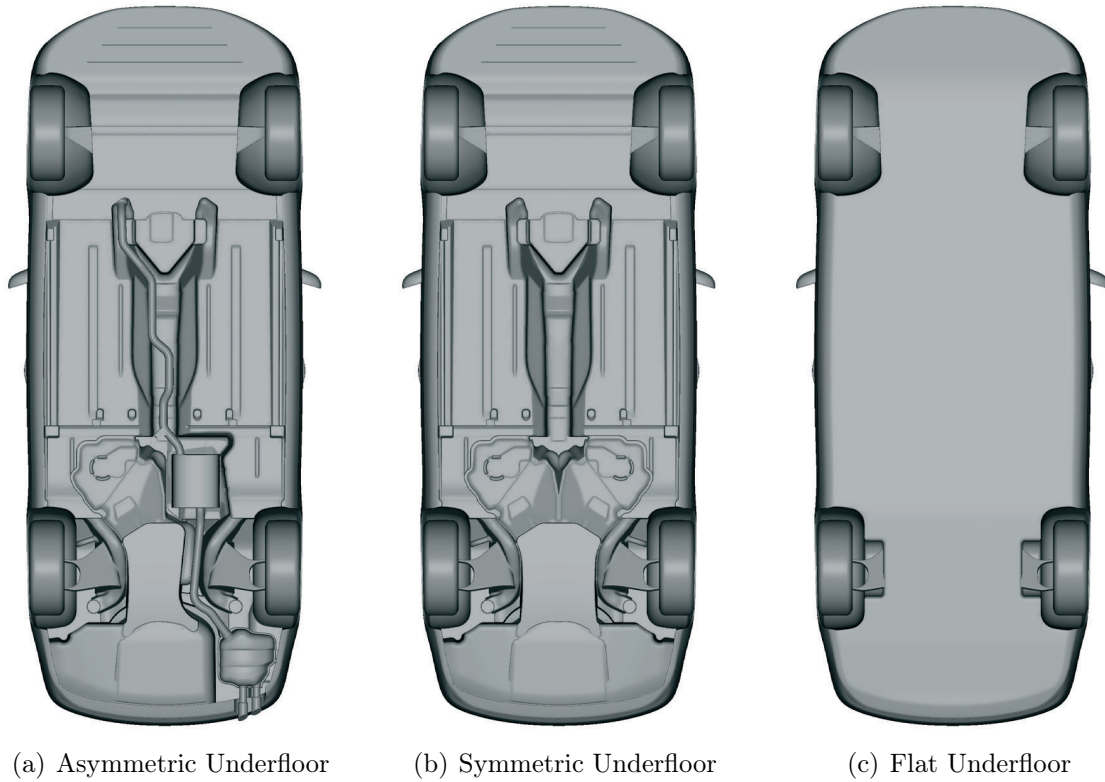
Figure 4.25: Asymmetric, symmetric and flat underfloor geometries.

The aerodynamic side force, roll and yaw moment for $+3.3°$ and $-3.3°$ yaw, derived from simulations with various underfloor geometries and computed on Grid 3, are summarized in Table 4.16. These data are confronted with experimental reference data for the real, asymmetric underfloor. As presented previously, experimental side force, roll and yaw moment are not absolutely symmetric for positive and negative yaw angles. However, this asymmetry of loads is heavily exaggerated by numerical results for the asymmetric underfloor. Simulations with symmetric and flat underfloor exhibit less asymmetric behavior and rather confirm with experimental data for the asymmetric underfloor. Obviously, significant discrepancies only appear at $\beta = +3.3°$, whereas loads at $\beta = -3.3°$ are less affected by a substitution of the underfloor geometry. Summing up, the asymmetric underfloor geometry leads to unrealistic loads at $\beta = +3.3°$ in the numerical simulation.

Table 4.16: Aerodynamic loads at constant yaw for various underfloor geometries.

Method	Underbody	C_y		C_{M_x}		C_{M_z}	
		$+3.3°$	$-3.3°$	$+3.3°$	$-3.3°$	$+3.3°$	$-3.3°$
Exp.	Asymmetric	-0.178	0.214	0.021	-0.035	0.019	-0.016
Sim.	Asymmetric	-0.111	0.225	0.005	-0.036	0.050	-0.020
Sim.	Symmetric	-0.173	0.216	0.023	-0.032	0.027	-0.025
Sim.	Flat	-0.195	0.221	0.027	-0.030	0.019	-0.021

To improve the physical understanding of the discrepancies between asymmetric and flat underfloor, the flow field at $\beta = +3.3°$ is intensively studied. Figure 4.26 shows iso-surfaces of the lateral velocity v at $\beta = +3.3°$. Surprisingly, the flow characteristics are inverted for flat and asymmetric underfloor. Although the flow enters from windward and leeward side for the asymmetric underfloor, it only enters from leeward for the flat underfloor geometry. The latter is qualitatively expected from experimental results for the asymmetric underfloor, as well.

(a) Asymmetric Underfloor   (b) Flat Underfloor
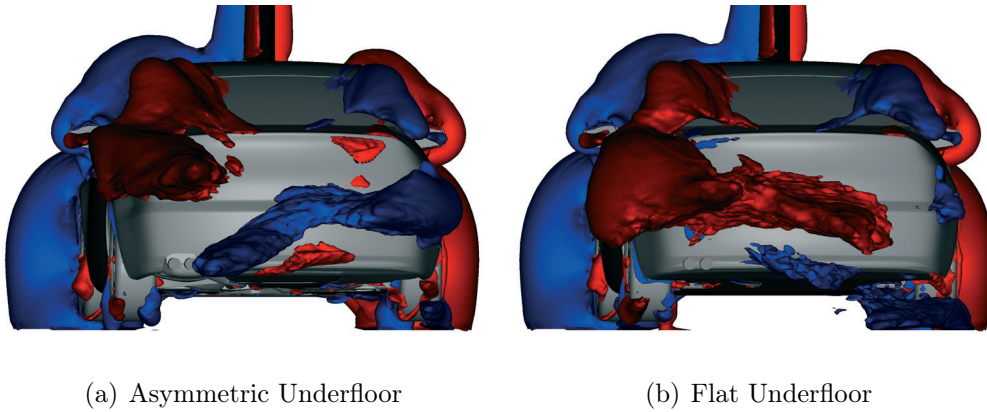
Figure 4.26: Iso-surfaces of $v = +5\,\text{m/s}$ (red) and $v = -5\,\text{m/s}$ (blue) for asymmetric and flat underfloor geometry at $\beta = +3.3°$.

Regions with $C_{p,tot} = 0$ in the wake flow field are outlined in Figure 4.27. In accordance to Figure 4.26, the total pressure losses are inverted for asymmetric and flat underfloor. Though the total pressure losses are largest behind the left vehicle rear for the asymmetric underfloor, they are largest behind the right vehicle rear for the flat underfloor.

(a) Asymmetric Underfloor ⠀⠀⠀⠀⠀⠀⠀⠀⠀ (b) Flat Underfloor
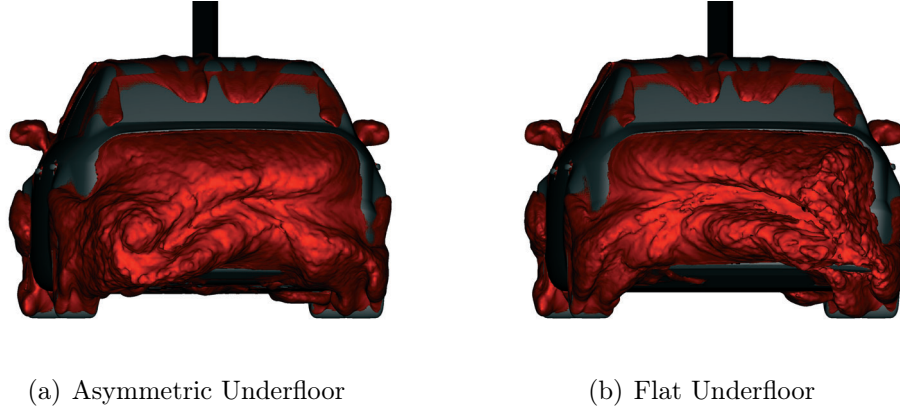
Figure 4.27: Iso-surface of $C_{p,tot} = 0$ for asymmetric and flat underfloor geometry at $\beta = +3.3°$.

In consequence, the static pressure distribution on the vehicle rear is inverted, as well. Figure 4.28 proves that the static high pressure region shifts from leeward to windward side when replacing the asymmetric by a flat underfloor. Logically, this increases surfaces pressures on the windward vehicle rear side and decreases pressures on the leeward rear side. Hence, the pressure difference between left and right rear is inverted and, in case of the flat underfloor, tends to counteract and reduce the total yaw moment as opposed to the asymmetric underfloor, where it is even increased. So, the estimation of the total yaw moment and the side force at $\beta = +3.3°$ is much more realistic for the flat underfloor due to the different flow characteristics in the wake field.

(a) Asymmetric Underfloor ⠀⠀⠀⠀⠀⠀⠀⠀⠀ (b) Flat Underfloor
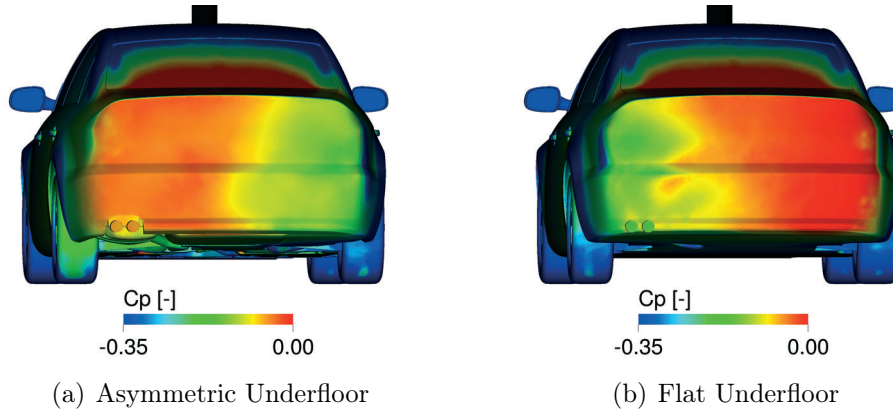
Figure 4.28: Static surface pressure at the vehicle rear for asymmetric and flat underfloor geometry at $\beta = +3.3°$.

The question arises, where the inversion of the lateral inflow into the wake flow originates from. Therefore, Figure 4.29 shows the total pressure distribution in a slice at $z = 0\,\text{m}$. With the asymmetric underfloor, the largest total pressure losses appear regardless of the yaw position behind the left rear (from the driver's perspective) of the vehicle. That coincides with the location of the exhaust system. With the flat underfloor, the main

pressure losses are consistently behind the windward vehicle rear. It can be concluded that the total pressure losses, which are numerically generated along the exhaust duct and exhaust system on the left side of the asymmetric underfloor, replace the main pressure losses at $\beta = +3.3°$, which are usually located behind the windward rear corner. At $\beta = $ -3.3°, exhaust and windward losses coincide. Due to this, numerical results at $\beta = $ -3.3° yield smaller discrepancies to experimental data than at $\beta = +3.3°$.

(a) Asymmetric Underfloor, $\beta = +3.3°$ (b) Flat Underfloor, $\beta = +3.3°$

(c) Asymmetric Underfloor, $\beta = $ -3.3°   (d) Flat Underfloor, $\beta = $ -3.3°
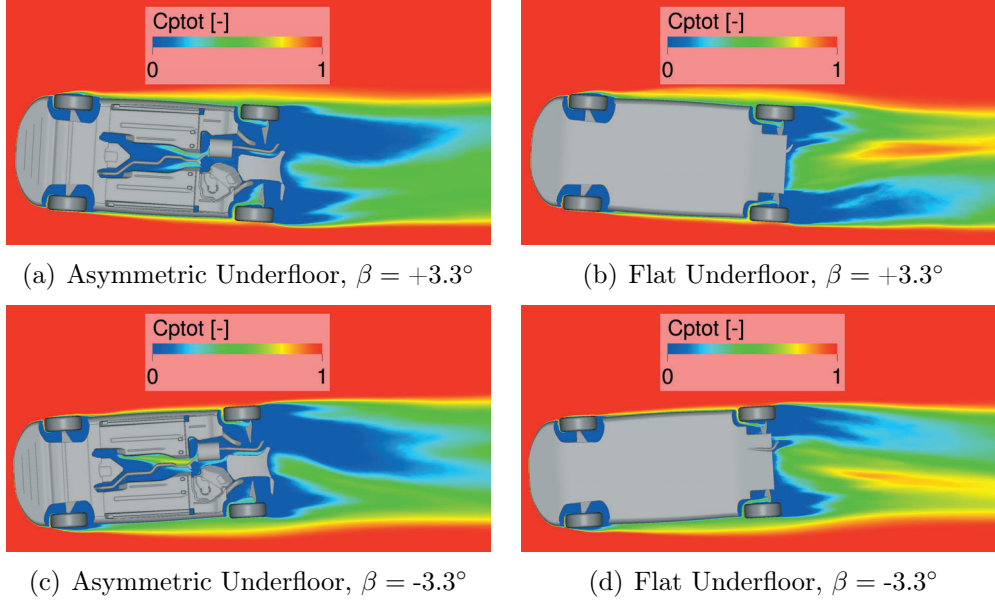
Figure 4.29: Total pressure in a slize at $z = 0$ m for asymmetric and flat underfloor geometry.

Losses of velocity magnitude are qualitatively identical to total pressure losses, though not shown in a separate plot. Since pressure and velocity losses at $\beta = +3.3°$ are located at opposite rear sides for flat and asymmetric underfloor, their static pressure distribution in the wake flow is inverted, as well. As presented in Figure 4.30, a region of high static pressure establishes behind the windward right corner for the asymmetric underfloor, whereas it is located behind the the leeward left corner for the flat underfloor. Surprisingly, this is not limited to the underfloor height but appears in any height between 0 m and 0.5 m. Since the fluid generally tends to avoid high pressure regions and tends to flow to regions of low static pressure, windward lateral inflow into the wake region is provoked for the asymmetric underfloor instead of leeward inflow at $\beta = +3.3°$. This is schematically sketched in Figure 4.30(c) and 4.30(d). In contrast, a region of high static pressure establishes behind the leeward rear corner for both underfloor geometries at $\beta = $ -3.3°, which provokes leeward inflow regardless of the underfloor.

Summing up, the largest total pressure loss in the simulation with asymmetric underfloor always occurs on the left rear back – regardless of the yaw position. With the flat underfloor, however, the dominating total pressure loss consistently appears at the windward side, i.e. the dominating total pressure loss changes between left and right with a change of yaw angle. This explains why the deficiencies of the simulation with asymmetric underfloor are most evident at $\beta = +3.3°$, where the position of the total pressure loss is inverted compared to experimental results. As opposed to that, the total pressure losses of the exhaust system and at the windward rear coincide at $\beta = $ -3.3°.

(a) Asymmetric Underfloor, z=0.00 m

(b) Flat Underfloor, z=0.00 m

(c) Asymmetric Underfloor, z=0.25 m

(d) Flat Underfloor, z=0.25 m

(e) Asymmetric Underfloor, z=0.50 m

(f) Flat Underfloor, z=0.50 m
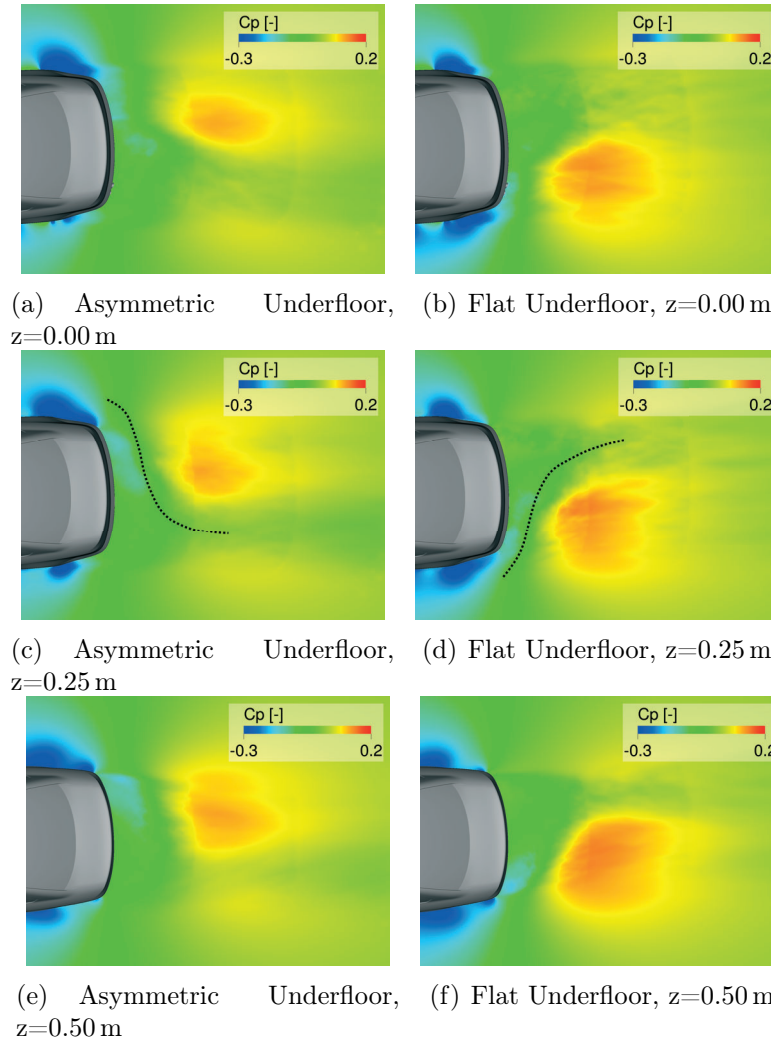
Figure 4.30: Static pressure in several slices at $z = 0$ m, $z = 0.25$ m and $z = 0.50$ m for asymmetric and flat underfloor geometry at $\beta = +3.3°$ with schematic sketch of flow path in (c) and (d).

4.3.3.3 Variation of ground clearance

Another attempt to investigate the asymmetric behavior of aerodynamic loads derived from simulations at positive and negative yaw angle, is to reduce the ground clearance. It is mentioned previously that the model is lifted off the ground, since the experimental setup was not capable of turning the moving belt as rapidly as the vehicle model. The resulting gap between the moving ground and the lowest point of the wheels is 30 mm. Now, the ground clearance is reduced step-by-step in the simulation using the original setup with asymmetric underfloor and the computational mesh Grid 3. Simulations are run in full scale at $\beta = +3.3°$, which turned out to be most critical in the preceding investigation. The moving ground is lifted in 3 steps of 20 mm in full scale. This corresponds to ground clearances of 30 mm, 20 mm, 10 mm and 0 mm in 1:2 scale for comparison with the experiment. Ground clearances are denoted in model scale in the following.

Table 4.17 outlines aerodynamic loads at $\beta = +3.3°$ from experiment and simulations for various ground clearances. According to the results, the absolute values of the side force

and the roll moment increase, whereas the yaw moment decreases with reduced ground clearance. In the simulation, changes of aerodynamic loads are small for ground clearances larger than 10 mm, but are most evident for a reduction from 10 mm to 0 mm. Finally, the values for 0 mm ground clearance agree best with experimental data for 30 mm ground clearance.

Table 4.17: Aerodynamic loads at $\beta = +3.3°$ for various ground clearances.

Method	Ground Clearance	C_y	C_{M_x}	C_{M_z}
Exp.	30 mm	-0.178	0.021	0.019
Sim.	0 mm	-0.194	0.028	0.024
Sim.	10 mm	-0.125	0.009	0.047
Sim.	20 mm	-0.125	0.009	0.045
Sim.	30 mm	-0.111	0.005	0.050

Figure 4.31 presents iso-surfaces of the lateral velocity component for the ground clearances studied. In agreement with the aerodynamic loads presented in Table 4.17, the wake flow is dominated by windward lateral inflow into the wake region for ground clearances above 10 mm. This changes significantly at 0 mm ground clearance, where leeward inflow occurs.

(a) Ground Clearance = 30 mm   (b) Ground Clearance = 20 mm

(c) Ground Clearance = 10 mm   (d) Ground Clearance = 0 mm
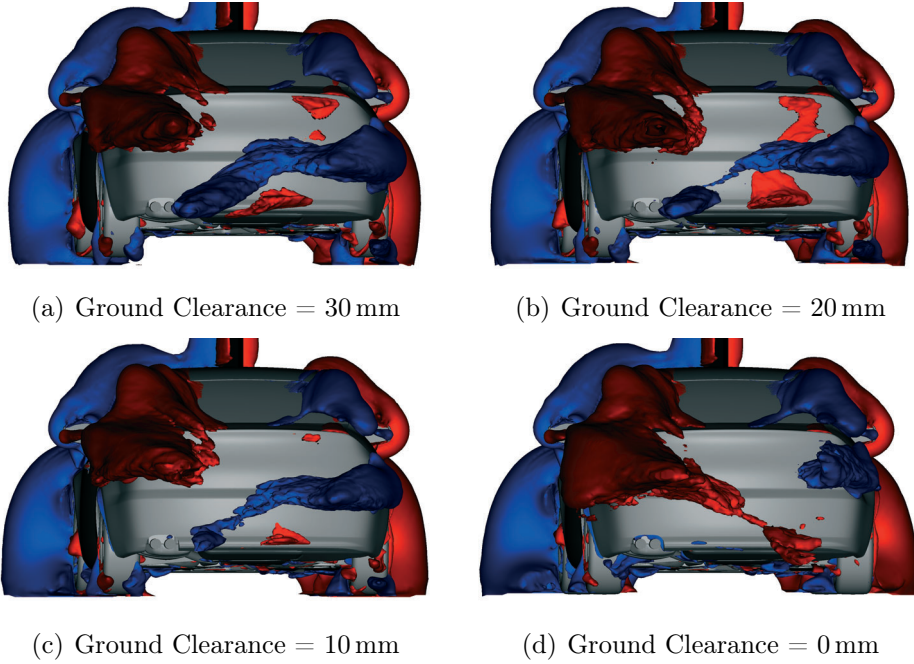
Figure 4.31: Iso-surfaces of $v = +5$ m/s (red) and $v = -5$ m/s (blue) for various ground clearances at $\beta = +3.3°$.

(a) Ground Clearance = 30 mm

(b) Ground Clearance = 20 mm

(c) Ground Clearance = 10 mm

(d) Ground Clearance = 0 mm
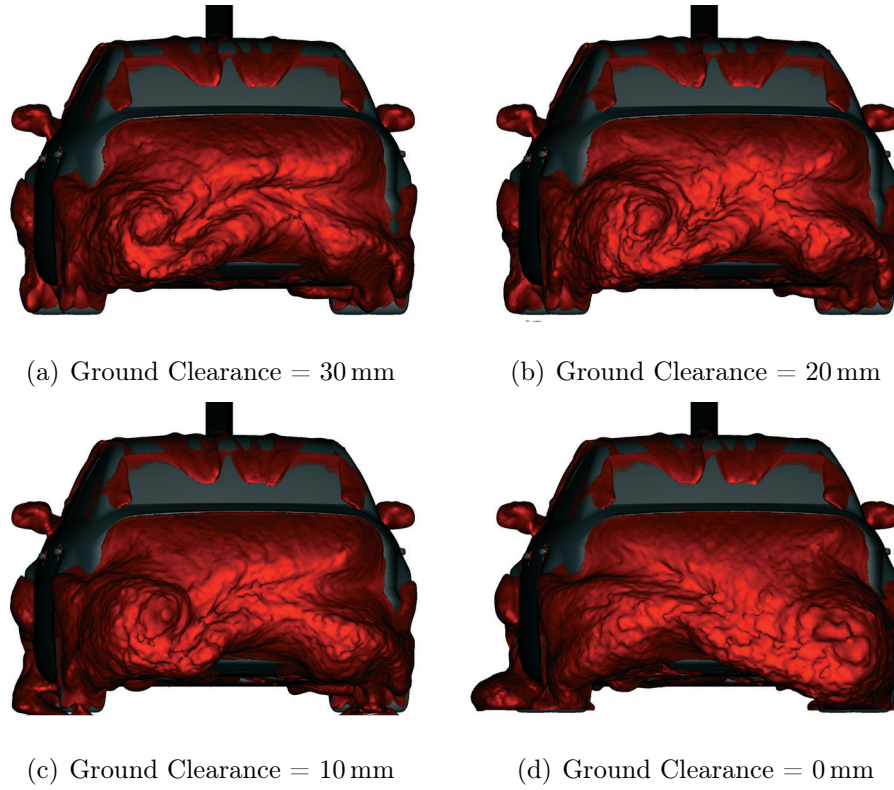
Figure 4.32: Iso-surface of $C_{p,tot} = 0$ for various ground clearances at $\beta = +3.3°$.

A similar observation is made when investigating the total pressure losses in the wake region of the vehicle, see Figure 4.32. Total pressure losses are most evident at the leeward, right rear side of the vehicle at $\beta = +3.3$ mm and ground clearances above 10 mm. Only at 0 mm ground clearance the pressure losses are most significant at the windward, left rear side of the vehicle.

(a) Ground Clearance = 30 mm

(b) Ground Clearance = 0 mm
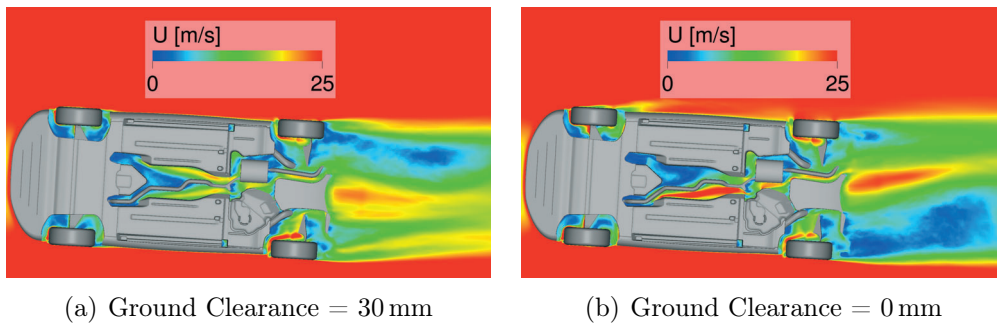
Figure 4.33: Velocity magnitude in a slice at z = -0.1 m for various ground clearances at $\beta = +3.3°$.

Generally, a reduction of ground clearance results in a decreased mass flow between ground and underfloor. As a consequence of reducing ground clearance to 0 mm at $\beta = +3.3°$, the static pressure at the exhaust pot and the leeward rear corner of the underfloor is decreased in the simulation. Hence, cross-flow from windward to leeward side in the underfloor region is not deflected any longer towards the windward rear corner of the underfloor, but flows directly towards the leeward rear corner. There, the velocity loss is then reduced. Instead, a velocity deficit occurs behind the windward right rear of the

vehicle in the simulations with 10 mm to 30 mm ground clearance. The velocity deficits are outlined in Figure 4.33.

As a consequence of the inverted total pressure and velocity losses for 0 mm and 30 mm ground clearance, the static pressure distribution in the wake flow is inverted, as well. In analogy to the comparison of flat and asymmetric underfloor (see Figure 4.30) a region of high static pressure establishes at either the windward or the leeward side at $\beta = +3.3°$. For 0 mm ground clearance the high pressure region is located leeward behind the vehicle, which finally provokes leeward inflow. Thus, the effect of ground clearance reduction to 0 mm is similar to a substitution of the asymmetric underfloor by a flat or fully symmetric underfloor geometry.

4.4 Summary and discussion

The experiment of chapter 3 is simulated using the Lattice Boltzmann solver PowerFLOW®. A 1:2 scale DrivAer notchback is oscillated around its vertical axis at realistic Reynolds and Strouhal numbers. Thus, the vehicle is exposed to unsteady flow conditions relevant in terms of driving stability during crosswind gusts. The numerical solver is capable of such a complex and demanding simulation setup and the performance of the numerical simulation is acceptable for industrial application.

It turns out that the surface pressure at the front of the vehicle instantaneously reacts on a change of the oncoming flow. At the rear, however, the surface pressure reacts with a delay and exhibits larger oscillation amplitudes compared to quasi-steady flow conditions. In turn, unsteady aerodynamic loads are observed to differ significantly from quasi-steady loads. In particular, the unsteady yaw moment exceeds the maximum value encountered during steady flow conditions. The numerical simulation generally captures the unsteady mechanism occurring at transient oncoming flow conditions. However, quantitative discrepancies between experimental data and numerical results occur.

It is known from previous investigations and from the experiment that the wake flow of a vehicle being subjected to constant crosswind is characterized by a region of high lateral velocity entering the wake region from the leeward side. In the simulation, however, the lateral inflow does not appear leeward but consistently at the right rear side for positive and negative yaw angles. This happens due to a one-sided, numerically overestimated total pressure loss at the asymmetric underfloor geometry of the DrivAer body. Consequently, the pressure difference between left and right vehicle rear side is inverted compared to experimental data at positive yaw angles. During transient yaw, unsteady surface pressure changes at the rear side are then underestimated. Finally, unsteady as well as steady loads are computed incorrectly.

Numerical results cannot be improved by modifications of the computational mesh. Instead, by reducing the ground clearance or substituting the asymmetric underfloor with a symmetric shaped underfloor, flow characteristics in the wake region are inverted at $\beta = +3.3°$, which provokes leeward inflow and increases windward rear surface pressures. Thus, aerodynamic loads are computed in close proximity to experimental data. It is suspicious that these geometric changes completely invert the flow characteristics at that

position. The sensitivity reveals that the numerical method exhibits significant errors for that specific setup, where a vehicle with complex underfloor geometry is lifted off the ground. Therein, momentum losses at the underfloor, which characterize and influence the wake flow field, turn out to be qualitatively wrong. Unfortunately, the solver does not allow for an adaption or selection of alternative wall and turbulence models, which might estimate the momentum losses differently. To this end, numerical results using a different numerical approach are presented in the following chapter.

4.5 Comparison with results from another numerical approach

Alternatively to the Lattice Boltzmann (LB) approach presented above, the experiment is modeled using a RANS approach implemented in the CFD package OpenFOAM® described in chapter 1.5.2. This was primarily done in order to assess the capability and accuracy of that open-source simulation tool and was published in detail by the author in [123]. Here, solely steady results are presented in order to investigate, if the discrepancies between numerical and experimental loads at $\beta = +3.3°$ observed with the LB approach can be reduced by using a different numerical method.

4.5.1 Numerical setup

The geometric setup and triangulated surface data are identical to the LB approach presented in the preceding chapter. The model scale is 1:2 according to the experiment. Here, the simulation volume is a box with 3 vehicle lengths in front and 5 vehicle lengths behind the model. The height of the simulation domain is 6 m and the width is 20 m. Hence, the blockage ratio calculates to 1%, whereas it is 0.8% in the experiment.

At the inlet the velocity is set to $u = 58.3\,\mathrm{m/s}$, the kinetic turbulent energy to $k = 0.082\,\mathrm{m^2/s^2}$ and the dissipation to $\varepsilon = 0.0387\,\mathrm{m^2/s^3}$. At the outlet a static pressure is prescribed. The top of the simulation volume as well as the side walls are defined as frictionless walls. The floor is defined as a moving wall with the same velocity as the inlet velocity of the flow. In accordance with the experiment, the wheels do not rotate. So, the boundary conditions are in line with the numerical setup presented in chapter 4.1.

The generation of volume meshes is performed using the third party software Spider [63,64]. In its finest areas the numerical grid exhibits two prism-layers with 3 mm length and 1.5 mm height in wall-normal direction followed by one prism-layer with 3 mm length and 3 mm height in wall-normal direction. Figure 4.34 illustrates the refinement regions used within the meshing process. The finest resolution is applied to those areas marked orange as well as to the wheels and mirrors. The remaining vehicle surface is resolved at half the resolution. There are two additional boxes presented in Figure 4.34 defining locally 6 mm and 12 mm cells. The total number of cell elements amounts to 10.9 million and the dimensionless distance between the first cell center and the wall in wall-normal direction is on average less than 50.
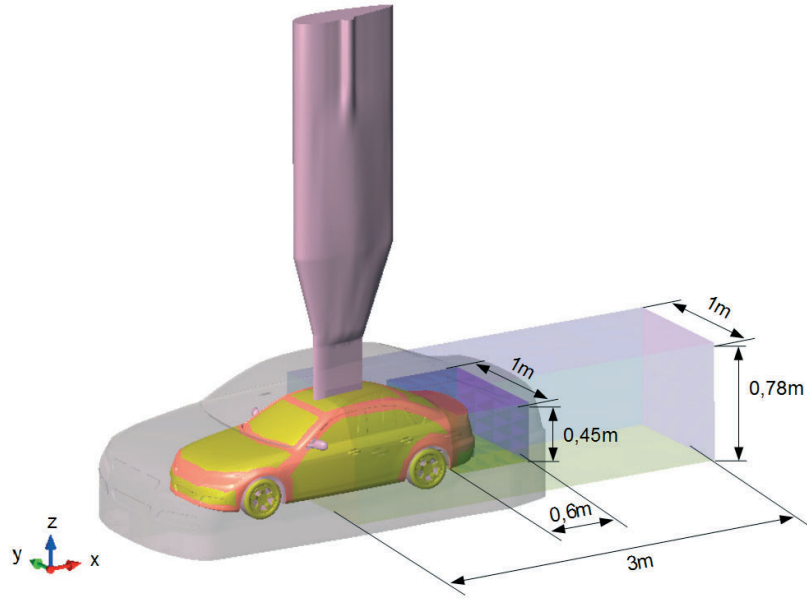
Figure 4.34: Vehicle geometry and local refinement zones for RANS simulation.
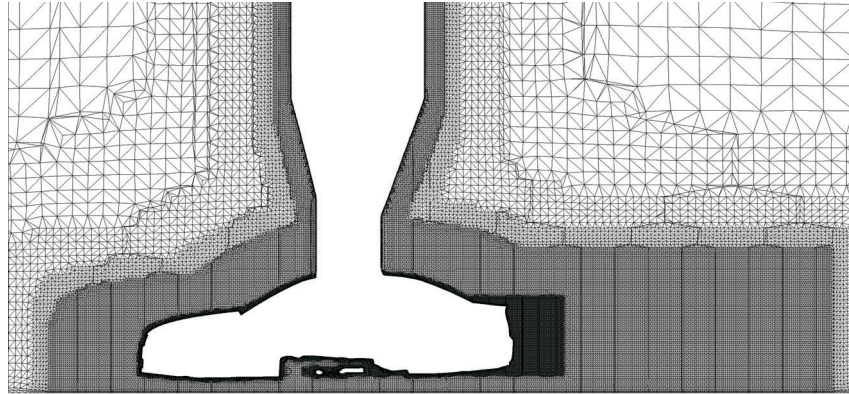
Figure 4.35: Cut through the volume mesh for RANS simulation at $y = 0$.

4.5.2 Results

Different turbulence models were tested among which the realizable k-ε model turned out as the most promising (compare [123]). Using this, the steady simulations ran approximately 15000 iterations and the results were averaged over the last 5000 iterations in order to account for high-frequent oscillations in the load signals. The simulation took 47 h on 64 cores.

Table 4.18 compares aerodynamic loads at constant yaw from experiment, from the simulation with RANS approach and realizable k-ε model and from the LB approach with k-ε RNG model as described in chapter 1.5.1. According to Table 4.18, both simulation methods predict aerodynamic loads at $\beta = $ -3.3° with similar accuracy. At $\beta = +3.3°$, the side force and yaw moment are slightly underestimated by the RANS approach, whereas they are overestimated by the LB approach. However, the RANS approach with realizable k-ε model predicts the side force and yaw moment much better.

Table 4.18: Aerodynamic loads during constant yaw from experiment and from simulations with different numerical models.

Method	Turb. Model	C_y +3.3°	C_y -3.3°	C_{M_x} +3.3°	C_{M_x} -3.3°	C_{M_z} +3.3°	C_{M_z} -3.3°
Experiment		-0.178	0.214	0.021	-0.035	0.019	-0.016
LB	k-ε RNG	-0.134	0.226	0.011	-0.036	0.038	-0.020
RANS	realizable k-ε	-0.199	0.222	0.033	-0.039	0.013	-0.012

Even though the focus of this study is not on lift forces, it is worth mentioning that the RANS approach predicts the down force with a maximum deviation of as little as 0.002, whereas the down force is overrated by the LB approach by around 0.100 (see Table 4.7).

Figure 4.36 outlines fluid regions with high lateral velocity components entering the wake flow field, as derived from the RANS approach with realizable k-ε model. The wake flow topology differs significantly from the topology predicted by the LB approach with k-ε RNG model presented in Figure 4.8. Apparently, the flow field computed with the RANS approach exhibits similar strong inflow from leeward and windward side. Thus, a symmetric lateral inflow appears for +3.3° and -3.3° yaw. This is in very good agreement with qualitative investigations of Theissen [107, 110] and with experimental results of Theissen et al. [107, 111] and their basic assumptions of the wake flow.

(a) $\beta = +3.3°$ 　　　　　　　　　　　　　　(b) $\beta = $ -3.3°
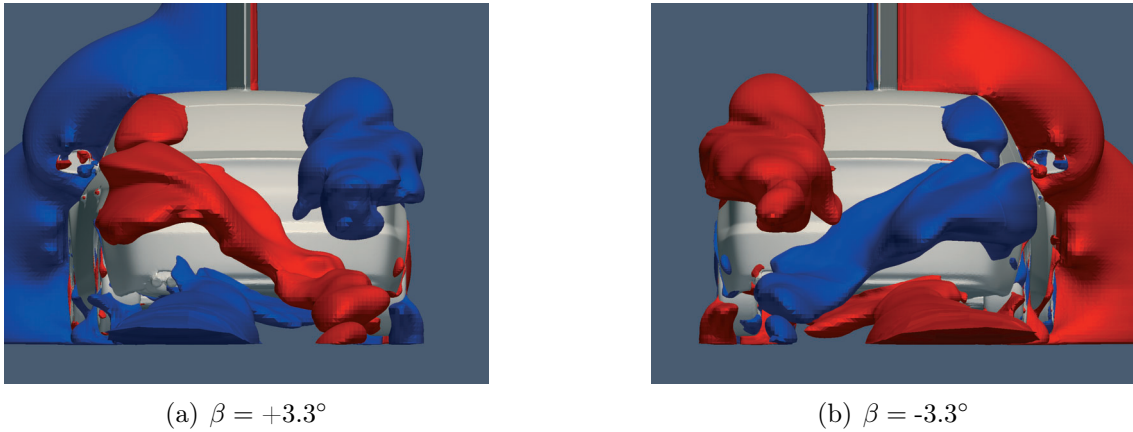
Figure 4.36: Iso-surfaces of $v = +10\,\text{m/s}$ (red) and $v = $ -10 m/s (blue) at $\beta = \pm 3.3°$ for RANS simulation with realizable k-ε turbulence model.

Hence, the RANS approach with realizable k-ε turbulence model overcomes the deficiencies of the LB approach, where lateral inflow from the vehicle right rear side dominated the wake flow regardless of the yaw position. Using the RANS approach the surface pressure at the windward vehicle rear is consequently increased for $\beta = +3.3°$. Thus, the direction of the side force component at the vehicle rear is predicted correctly. Since the rear side force then counteracts the total yaw moment, the yaw moment is finally decreased, whereas it was largely exaggerated by the LB approach, compare Table 4.18. In the end, the absolute values of the yaw moments encountered at $\beta = \pm 3.3°$ are almost identical for the RANS approach, whereas they diverge for the LB approach (see Table 4.18).

4.5.3 Discussion

Steady calculations at constant yaw using a RANS approach with realizable k-ε model deliver more accurate results than the LB approach with k-ε RNG model. In particular, the computed total pressure losses from the asymmetric underfloor at $\beta = +3.3°$ and hence the static pressure distribution in the wake field result in a lateral inflow like in the experiment.

At the same time, the physical accuracy of the RANS approach is limited when working with coarser grids and other turbulence models, which is not shown here, but can be taken from [123]. It turned out that a realizable k-ε model estimates the wake flow more accurately than for instance the nonlinear k-ε model from Zhu et al. [128] or the k-ω-SST model from Menter [75]. A dominating leeward inflow at the rear lights at $\beta = +3.3°$ only occurs using the realizable k-ε model. The other two turbulence models investigated lead to flow characteristics closer to the results of the LB approach with k-ε RNG model (compare [123]). Besides, the accuracy of the RANS prediction strongly depends on the mesh quality and its number of cells. Good agreement with experimental results is achieved for the numerical grid with 10.9 million cells. In contrast, results from another numerical grid with 6.2 million cells did not lead to reasonable estimations of aerodynamic loads (compare [123]).

Simulations at transient yaw with the setup, which gives good results at constant yaw, were not performed. Considering the computational resources needed this was not achievable. Instead, an unsteady RANS simulation with OpenFOAM® was accomplished for a coarse grid. The results are not valuable enough to be presented in this work, but its performance can be applied as a benchmark. Using the sliding mesh interface of OpenFOAM® between rotating and non-rotating numerical domain, called generalized grid interface (GGI, compare [11]), a transient simulation for 3 s physical time comprising two full oscillations and 1 s each at $\beta = \pm3.3°$ was computed. The time step was $\delta t = 1 \cdot 10^{-5}$ s and the computational grid consisted of 6.2 million cell elements. Finally, the simulation ran for 500 h on 64 cores. The performance was 6.1 s per time step without mesh rotation and 9.7 s per time step with mesh rotation.

A transient simulation with the grid presented in chapter 4.5.1 with almost twice as many cell elements would require half of the time step and, hence, roughly estimate to 40 days simulation time for two oscillation periods. Unfortunately, the simulation times cannot be reduced by parallelization, since scalability is very much limited when using the GGI of OpenFOAM®, where the data transfer is implemented in series. Though the performance of the steady solver is sufficient, the performance of the transient solver plus the GGI is poor compared to the commercial LB solver, where 5 s physical time on a grid with 37.8 million cell elements are computed in roughly 300 h on 96 cores. So, transient simulations on sufficiently resolved computational grids using the open source software package OpenFOAM® are beyond the limit of industrially tolerable simulation times and do not meet the standards set by commercial CFD solvers. Admittedly, the complexity of the setup combined with a high Reynolds number and a long physical simulation time set hard test conditions for that numerical process.

4.6 Conclusions

The experiment presented in chapter 3 is numerically simulated using PowerFLOW®, which is based on the Lattice Boltzmann method. Qualitatively, load transients recorded in the experiment during model oscillation with $f = 2\,\mathrm{Hz}$ and $\beta = \pm3.3°$ agree with numerical results. Still, significant quantitative deficiencies occur even at constant yaw position of the DrivAer body with asymmetric underfloor due to overrated total pressure losses along the exhaust system and behind the right vehicle rear. As a consequence, lateral inflow into the wake region from the leeward side at $\beta = +3.3°$ appears to a considerably smaller extent in the simulation than in the experiment. Thus, the numerical prediction of surface distributions at the vehicle rear fails, which negatively affects the estimation of aerodynamic loads. Most evident, the side force amplitude for a quasi-steady change of yaw from +3.3° to -3.3° is overestimated by 37% and the unsteady yaw moment amplitude is overestimated by 61%.

That behavior disappears by decreasing the ground clearance to realistic values of vehicles on-road or by replacing the asymmetric underfloor with a flat or a symmetric underfloor geometry. So, the numerical method exhibits significant errors limited to a setup, where a vehicle with complex underfloor geometry is lifted off the ground. Since the solver does not allow for an adaption or selection of alternative wall and turbulence models, a different numerical method was tested, instead. A RANS method with realizable k-ε turbulence model finally proved to predict total pressure losses and hence lateral inflow into the wake field much more accurately for the ground clearance and underfloor geometry actually used in the experiment. The performance of the unsteady RANS solver and the sliding mesh interface implemented in OpenFOAM®, which permits modeling an oscillating vehicle, is, however, not yet sufficient for industrial application in a development process.

5 Summary and outlook

Summary

With the results documented in this work an important step is taken towards a quantitative understanding of unsteady vehicle aerodynamics during crosswind gusts. As a prerequisite for numerical and experimental investigations, the oncoming flow facing a vehicle during crosswind gusts was experimentally studied. According to the results, it should be modeled as a velocity distortion traveling with main wind speed through a simulation domain. In particular, the velocity distortion should be a single or trapezoidal peak that naturally appears in axial and lateral direction. Most often it exhibits a change from positive to negative yaw and vice versa. The amplitude of the velocity distortions recorded at Beaufort 4–7 is bounded by maximum $8\,\mathrm{m/s}$, which proves that yaw angle changes have been overestimated by most experimental and numerical investigations so far. Based on the presented on-road tests and information on the sensitivity of the driver and of vehicle dynamics, turbulence scales occurring in natural crosswind gusts can be classified into

- ▶ large turbulence scales that have a quasi-steady effect
- ▶ medium turbulence scales that have a relevant effect and
- ▶ small turbulence scales that have an irrelevant effect

on driving stability during crosswind gusts. Although the classification was already proposed in the past, the limits between the three classes have never been quantified. According to the results of this work, scales between $0.5\,\mathrm{Hz}$ and $4\,\mathrm{Hz}$ at aerodynamic standard vehicle speed $U_{veh} = 140\,\mathrm{km/h}$ should be considered when analyzing the crosswind sensitivity of future vehicles.

As a second step, unsteady vehicle aerodynamics were studied experimentally under time-dependent oncoming flow conditions. To this end, a 1:2 scale generic, but realistic vehicle model was oscillated around its vertical axis at $f = 2\,\mathrm{Hz}$ and $\beta = \pm 3.3°$ whilst being subjected to $u_{wind} = 210\,\mathrm{km/h}$ in a wind tunnel. Thus, the vehicle was exposed to realistic Reynolds ($\mathrm{Re} = 9 \cdot 10^6$) and Strouhal numbers ($\mathrm{Sr} = 0.08$) characterizing natural crosswind gusts. Using this setup, it was shown by Theissen [107] that the yaw moment exhibits larger unsteady than quasi-steady oscillations, whereas unsteady side force and roll moment amplitudes do not reach steady values. Here, the physical mechanism leading to the differences between unsteady and quasi-steady load transients was revealed by means of surface pressure measurements. A low pressure region around the rear lights dominates the surface pressure distribution at the rear side of the DrivAer notchback. This is more pronounced at the leeward side, where fluid with high lateral velocity enters the wake region. During model oscillation the pressure changes at the rear are magnified and

delayed compared to quasi-steady changes. Interestingly, the magnification and delay are most prominent around the rear lights. Pressure fluctuations at the vehicle front, however, react instantaneously on a change of the oncoming flow. The time delay at the rear causes a smaller unsteady than quasi-steady rear side force at peak yaw. Since the rear side force counteracts the overall yaw moment, the total unsteady yaw moment finally exceeds the total quasi-steady yaw moment. So, the unsteady mechanism proposed by Theissen [107] was confirmed and the phase lag of unsteady pressure oscillations at the rear was shown to be a crucial parameter with respect to unsteady load developments.

Unsteady overshoot of yaw moment and undershoot of side force and roll moment was shown to happen for oscillation amplitudes between $\pm 2.2°$ and $\pm 4.4°$. Thereby, the ratio of unsteady to quasi-steady loads turned out neither to be constant nor to behave linearly with respect to the oscillation amplitude. Instead, the difference between unsteady and quasi-steady amplitudes was fairly constant. Measurements at various wind speeds proved that Reynolds influence is weak for $Re > 6 \cdot 10^6$. During model oscillation, the largest yaw moment magnification was found for $Sr = 0.12$. From this, it was assumed that the intensity of unsteady flow phenomena is determined by the interaction of the time scale of the model rotation and the time scale of the delayed wake flow, described by the Strouhal number. Notchback, fastback and station wagon variants of the DrivAer body exhibited similar unsteady load behavior. However, the unsteady yaw moment overshoot turned out to be smallest for the station wagon, which could be attributed to smaller unsteady pressure variations at the rear side.

Those experimental results created a valuable data base for the unsteady validation of the numerical simulation tool PowerFLOW®, which is based on the Lattice Boltzmann method with fixedly implemented k-ϵ RNG turbulence model. Its capability to simulate the complex experiment was proved and qualitative agreement was observed, as yaw moment overshoot as well as side force and roll moment undershoot were predicted by the simulation. However, considerable quantitative discrepancies occurred even at constant yaw position of the DrivAer body with asymmetric underfloor due to overrated total pressure losses along the exhaust system and behind the right vehicle rear. As a result, lateral inflow into the wake region from the leeward side at $\beta = +3.3°$ was significantly weakened by the numerical simulation. Hence, the prediction of surface pressure distributions at the vehicle rear was erroneous, which negatively affected the estimation of aerodynamic loads. In total, the side force amplitude for a quasi-steady change of yaw from $+3.3°$ to $-3.3°$ was overestimated by 37% and the unsteady yaw moment amplitude was overestimated by 61%.

The numerical exaggeration of total pressure losses disappeared by reducing the ground clearance to realistic on-road values or by replacing the asymmetric underfloor with flat or symmetric underfloor geometries. Following from this, significant numerical errors were limited to a setup, where a vehicle with complex underfloor geometry is lifted off the ground. In a last step, a different numerical simulation tool (OpenFOAM®) was tested, which is based on the RANS method and allows for an adaption or selection of alternative wall and turbulence models. A realizable k-ϵ turbulence model finally proved to predict total pressure losses and hence lateral inflow into the wake field much more accurate for the ground clearance and underfloor geometry actually used in the experiment. The performance of the unsteady solver and the sliding mesh interface implemented in OpenFOAM® are, however, not sufficient for proper industrial application.

Outlook

A car manufacturer's main goal is to optimize the safety and comfort perceived by the customer. Having future vehicle trends in mind, this optimization should be expanded to the vehicle performance during crosswind gusts. Since corrective actions include geometric changes that affect the overall vehicle architecture, the driving stability of vehicle designs must be tested at an early stage of the development process. For that reason it is indispensable to correctly predict the vehicle response during crosswind gusts by numerical simulation. However, the vehicle response is the result of a complex and coupled procedure, as it involves vehicle aerodynamics, vehicle dynamics and the driver's reaction. Hence, only coupled simulation models will be suitable for a correct estimation of the real vehicle response. Making that effort, a virtual crosswind gust analysis covering the complete event chain is feasible. Such a fully coupled analysis was recently demonstrated exemplarily by Nakashima and Tsubokura et al. [78]. Regarding a proper industrial application, the key will be to possess an accurately validated simulation model. As a prerequisite, this requires the validation of the simulation tools used for each discipline.

In this work, the disciplines were separated and it was focused on vehicle aerodynamics. Basic physical understanding for fluid dynamics during crosswind gust events was gathered. Still, the validation of a numerical setup using PowerFLOW® failed. When aiming for continuing working with this solver, one would have to rebuild the experiment by additionally modeling the contact between wheels and moving ground. Then, the numerical overestimation of total pressure losses at the underfloor with k-ϵ RNG turbulence model might diminish. Alternatively, experimental data could be used for the validation of another industrially applicable numerical solver. Indications for appropriate simulation setups and turbulence models are provided by this work, while OpenFOAM® and its sliding mesh implementation were shown to lack in performance.

List of Figures

List of Tables

References

[1] AEROPROBE CORPORATION. *Five- and Seven-Hole Probe Manual*. Blacksburg, Virginia, USA, 2003.

[2] ASCHWANDEN, P., MÜLLER, J., TRAVAGLIO, G., AND SCHÖNING, T. The Relevance of Transient Aerodynamic Effects on Vehicle Dynamics. In *MIRA International Vehicle Aerodynamics Conference* (England, 2008).

[3] BAEDER, D., INDINGER, T., ADAMS, N. A., AND DECKER, F. Comparison of Numerical Simulations with Experiments of Bluff Bodies Including Under-Hood Flow. *SAE Technical Paper Series*, 2011-01-0171 (2011).

[4] BAKER, C. Ground Vehicles in High Cross Winds Part 1: Steady Aerodynamic Forces. *Journal of Fluids and Structures 5* (1991), 69–90.

[5] BAKER, C. Ground Vehicles in High Cross Winds Part 2: Unsteady Aerodynamic Forces. *Journal of Fluids and Structures 5* (1991), 91–111.

[6] BAKER, C. Ground Vehicles in High Cross Winds Part 3: The Interaction of Aerodynamic Forces and the Vehicle System. *Journal of Fluids and Structures 5* (1991), 221–241.

[7] BAKER, C. The Behavior of Road Vehicles in Unsteady Cross Winds. *Journal of Wind Engineering and Industrial Aerodynamics* (1993), 439–448.

[8] BAKER, C., AND HUMPHREYS, N. Assessment of the Adequacy of Various Wind Tunnel Techniques to Obtain Aerodynamic Data for Ground Vehicles in Cross Wind. *Journal of Wind Engineering and Industrial Aerodynamics 60* (1996), 49–68.

[9] BEARMAN, P., AND MOREL, T. Effect of Free Stream Turbulence on the Flow Around Bluff Bodies. *Progress in Aerospace Sciences 20* (1983), 97–123.

[10] BEARMAN, P., AND MULLARKEY, S. Aerodynamic Forces of On-Road Vehicles due to Steady Side Winds and Gusts. In *Proceedings of the Royal Aeronautical Society* (London, England, 1994).

[11] BEAUDOIN, M., AND JASAK, H. Development of a Generalized Grid Interface for Turbomachinery Simulations with OpenFOAM. In *Open Source CFD International Conference* (Berlin, Germany, 2008).

[12] BENDAT, J., AND PIERSOL, A. *Measurement and Analysis of Random Data*. John Wiley & Sons, 1966.

[13] BENDAT, J., AND PIERSOL, A. *Engineering Applications of Correlation and Spectral Analysis.* John Wiley & Sons, 1980.

[14] BENDAT, J., AND PIERSOL, A. *Random Data, Analysis and Measurement Procedures.* John Wiley & Sons, 2000.

[15] BHATAGNAR, P., GROSS, E., AND KROOK, M. A Model for Collsision in Gases - Small Amplitude Processes in Charged and Neutral One-Component Systems. *Phys. Review A 94*, 3 (1954), 511–525.

[16] BRÜEL&KJAER. *Product Data Condenser Microphone Cartridges - Types 4133 to 4181.* Naerum, Denmark, 2009.

[17] CAIRNS, R. S. *Lateral Aerodynamics of Motor Vehicles in Transient Crosswinds.* PhD thesis, Cranfield University, 1994.

[18] CARETTO, L., GOSMAN, A., PATANKAR, S., AND SPALDING, D. Two Calculation Procedures for Steady Three-Dimensional Flows With Recirculation. In *International Conference Numerical Methods Fluid Dynamics* (Paris, France, 1972).

[19] CARLINO, G., AND COGOTTI, A. Simulation of Transient Phenomena with Turbulence Generation System in the Pininfarina Wind Tunnel. *SAE Technical Papers Series*, 2006-01-1031 (2006).

[20] CHADWICK, A., GARRY, K., AND HOWELL, J. Transient Aerodynamic Characteristics of Simple Vehicle Shapes by the Measurement of Surface Pressures. *SAE Technical Paper Series*, 2001-01-0876 (2001).

[21] CHEN, H., KANDASAMY, S., ORSZAG, S., SHOCK, R., SUCCI, S., AND YAKOT, V. Extended Boltzmann Kinetic Equation for Turbulent Flows. *Science 301* (2003), 633–636.

[22] CHEN, H., ORSZAG, S., STAROSELSKY, I., AND SUCCI, S. Expanded Analogy between Boltzmann Kinetic Theory of Fluid and Turbulence. *Journal of Fluid Mechanics 519* (2004), 301–314.

[23] CHEN, S., AND DOOLEN, G. Lattice Boltzmann Method for Fluid Flows. *Annual Review Fluid Mechanics 20* (1998), 329–364.

[24] COGOTTI, A. Generation of a Controlled Level of Turbulence in the Pininfarina Wind Tunnel for the Measurement of Unsteady Aerodynamics and Aeroacoustics. *SAE Technical Papers Series*, 2003-01-0430 (2003).

[25] COGOTTI, A. Generation of a Controlled Turbulent Flow in an Automotive Wind Tunnel and its Effect on Car Aerodynamics and Aeroacoustics. In *Progress in Vehicle Aerodynamics III - Unsteady Flow Effects*, J. Wiedemann and W. H. Hucho, Eds. Expert Verlag, 2004, pp. 150–176.

[26] COGOTTI, A., CARDANO, D., CARLINO, G., AND COGOTTI, F. Aerodynamics and Aeroacoustics of Passenger Cars in a Controlled High Turbulence Flow: Some

New Results. *SAE Technical Papers Series*, 2005-01-1455 (2005).

[27] COOPER, K., AND WATKINS, S. The Unsteady Wind Environment of Road Vehicles, Part One: A Review of the On-road Turbulent Wind Environment. *SAE 2007-01-1236* (2007).

[28] COOPER, R. The Effect of Cross-Winds on Trains. *Journal of Fluids Engineering 103* (1981), 127–136.

[29] COOPER, R. Atmospheric Turbulence with Respect to Moving Ground Vehicles. *Journal of Wind Engineering and Industrial Aerodynamics 17* (1984), 215–238.

[30] CYR, S., IH, K., AND PARK, S. Accurate Reproduction of Wind-Tunnel Results with CFD. *SAE Technical Paper Series*, 2011-01-0158 (2011).

[31] DAVENPORT, A. The Application of Statistical Concepts to the Wind Loading of Structures. In *Proceedings of the Institution of Civil Engineering* (1961), pp. 449–472.

[32] DEMUTH, R., AND BUCK, P. Numerical Investigations on the Unsteady Aerodynamics of Road Vehicles under Gusty Weather Conditions. In *MIRA International Vehicle Aerodynamics Conference* (England, 2006).

[33] DOCTON, M. *The Simulation of Transient Cross Winds on Passenger Vehicles.* PhD thesis, University of Durham, 1996.

[34] DOMINY, R., AND RYAN, A. An Improved Wind Tunnel Configuration for the Investigation of Aerodynamic Cross Wind Gust Response. *SAE Technical Paper Series*, 1999-01-0808 (1999).

[35] DUELL, E., KHAZARI, A., MULLER, S., EBELING, W., AND MERCKER, E. The BMW AVZ Wind Tunnel Center. *SAE Technical Paper Series*, 2010-01-0118 (2010).

[36] ENGINEERING SCIENCES DATA UNIT. *Characteristics of Atmospheric Turbulence near the Ground, Part 1: Definitions and General Information*, 1974.

[37] ENGINEERING SCIENCES DATA UNIT. *Characteristics of Atmospheric Turbulence near the Ground, Part 2: Single Point Data for Strong Winds (Neutral Atmosphere)*, 1985.

[38] FAVRE, T. *Numerical Investigation of Unsteady Crosswind Aerodynamics for Ground Vehicles.* Licentiate thesis, KTH Stockholm, 2009.

[39] FAVRE, T. *Aerodynamic Simulations of Ground Vehicles in Unsteady Crosswind.* PhD thesis, KTH Stockholm, 2011.

[40] FAVRE, T., AND EFRAIMSSON, G. Numerical Study of Design Alternatives Affecting the Crosswind Characteristics of a Generic Road Vehicle Model. In *MIRA International Vehicle Aerodynamics Conference* (England, 2008).

[41] FAVRE, T., AND EFRAIMSSON, G. An Assessment of Detached-Eddy Simulations

of Unsteady Crosswind Aerodynamics of Road Vehicles. *Flow, Turbulence and Combustion 87*, 1 (2011), 133–163.

[42] Favre, T., Efraimsson, G., and Diedrichs, B. Numerical Investigation of Unsteady Crosswind Vehicle Aerodynamics using Time-Dependent Inflow Conditions. In *MIRA International Vehicle Aerodynamics Conference* (England, 2008).

[43] Ferziger, J., and Perić, M. *Computational Methods for Fluid Dynamics*. Springer-Verlag, 2002.

[44] Filippone, A. Unsteady Aerodynamic Effects in Vehicle Passing. In *MIRA International Vehicle Aerodynamics Conference* (England, 2004).

[45] Flay, R. *Structure of a Rural Atmospheric Boundary Layer Near the Ground*. PhD thesis, University of Canterbury, 1978.

[46] Garry, K., and Cooper, K. Comparison of Quasi-Static and Dynamic Wind Tunnel Measurements on Simplified Tractor-Trailer Models. *Journal of Wind Engineering and Industrial Aerodynamics 22* (1986), 185–194.

[47] Gohlke, M., Beaudoin, J., Amielh, M., and Anselmet, F. Effect of Unsteady Separation on an Automotive Bluff-Body In Cross-Wind. In *IUTAM Symposium on Unsteady Separated Flows and Their Control* (2007).

[48] Gohlke, M., Beaudoin, J., Amielh, M., and Anselmet, F. Experimental Analysis of Flow Structures and Forces on a 3D-Bluff-Body in Constant Cross-Wind. *Experiments of Fluids 43* (2007), 579–594.

[49] Gohlke, M., Beaudoin, J., Amielh, M., and Anselmet, F. Thorough Analysis of Vortical Structures in the Flow Around a Yawed Bluff Body. *Journal of Turbulence 9 (15)* (2008).

[50] Guilmineau, E., and Chometon, F. Numerical and Experimental Analysis of Unsteady Separated Flow behind an Oscillating Car Model. *SAE Technical Paper Series*, 2008-01-0738 (2008).

[51] Heft, A. I., Indinger, T., and Adams, N. A. Investigation of Unsteady Flow Structures in the Wake of a Realistic Generic Car Model. No. 2011-3669.

[52] Hemida, H., and Krajnovic, S. LES Study of the Influence of a Train-Nose Shape on the Flow Structures Under Cross-Wind Conditions. *Journal of Fluids Engineering 130* (2008).

[53] Hemida, H., and Krajnovic, S. Investigation of Unsteady Flow Structures in the Wake of a Realistic Generic Car Model. *Journal of Fluids Engineering 131* (2009).

[54] Heuler, K. Analysis of the Flow Topology in the Wake of a Notchback Vehicle under Constant Yaw. Master's thesis, Technische Universitaet Muenchen, 2010.

[55] HINZE, J. O. *Turbulence: An Introduction to its Mechanism and Theory.* McGraw-Hill Book Company Inc., 1959.

[56] HOWELL, J., NEWNHAM, P., AND PASSMORE, M. Effect of Free Stream Turbulence on Road Vehicle Aerodynamics. In *FKFS Conference* (Stuttgart, Germany, 2007).

[57] HUCHO, W. *Aerodynamik stumpfer Körper: Physikalische Grundlagen und Anwendungen in der Praxis.* Vieweg-Verlag, 2002.

[58] HUCHO, W. *Aerodynamik des Automobils*, vol. 5. Vogel-Verlag„ 2005.

[59] HÄNEL, D. *Molekulare Gasdynamik.* Springer-Verlag, 2004.

[60] IYENGAR, A., AND FARELL, C. Experimental Issues in Atmospheric Boundary Layer Simulations: Roughness Length and Integral Length Scale Determination. *Journal of Wind Engineering and Industrial Aerodynamics 89* (2001), 1059–1080.

[61] JASAK, H. *Error Analysis and Estimation for the Finite Volume Method with Applications to Fluid Flows.* PhD thesis, Imperial College London, 1996.

[62] KAMEIER, F. *Experimentelle Untersuchung zur Entstehung und Minderung des Blattspitzen-Wirbellärms axialer Strömungsmaschinen.* PhD thesis, Deutsches Zentrum für Luft- und Raumfahrt, 1993.

[63] KICKINGER, F. *Tools for the Numerical Simulation of 3D Magnetic Field Problems: Construction, Analysis and C++ Implementation.* Trauner-Verlag, 1996.

[64] KICKINGER, F. Parallel Mesh Generation for Large Scale Applications using Hex-Dominant Meshes. In *ASIM 2005* (2005), p. 133.

[65] KOBAYASHI, N., AND YAMADA, M. Stability of a One Box Type Vehicle in Crosswind - an Analysis of Transient Aerodynamic Forces and Moments. *SAE Technical Paper Series*, 881878 (1988).

[66] KRAJNOVIC, S., BENGTSSON, A., DAVIDSON, L., AND BASARA, B. Numerical Study of Crosswind Stability of a Simplified Car at Gusty Wind. In *MIRA International Vehicle Aerodynamics Conference* (England, 2010).

[67] KULITE SEMICONDUCTOR PRODUCTS INC. *Kulite Miniature Ruggedized IS Pressure Transducers XT-190 (M) Series.* Leonia, New Jersey, USA, 2009.

[68] LAWSON, A., DOMINY, R., AND SIMS-WILLIAMS, D. A Comparison between On-Road and Wind Tunnel Surface Pressure Measurements on a Mid-Sized Hatchback. *SAE Technical Paper Series*, 2007-01-0898 (2007).

[69] LAWSON, A., SIMS-WILLIAMS, D., AND DOMINY, R. Effects of On-Road Turbulence on Vehicle Surface Pressures in the A-Pillar Region. *SAE Technical Paper Series*, 2008-01-0474 (2008).

[70] LEMKE, T. *Untersuchung der Fahrzeugumströmung bei Seitenwind für die Früh-*

phase der Pkw-Entwicklung. PhD thesis, Universität Siegen, 2006.

[71] LINDENER, N., MEIHLING, H., COGOTTI, A., COGOTTI, F., AND MAFFEI, M. Aeroacoustic Measurements in Turbulent Flow on the Road and in the Wind Tunnel. *SAE Technical Paper Series*, 2007-01-1551 (2007).

[72] MANKOWSKI, O., SIMS-WILLIAMS, D., DOMINY, R., DUNCAN, B., AND GARGOLOFF, J. The Bandwidth of Transient Yaw Effects on Vehicle Aerodynamics. *SAE Technical Paper Series*, 2011-01-0160 (2011).

[73] MANSOR, S., AND PASSMORE, M. Estimation of Bluff Body Transient Aerodynamics Using an Oscillating Model Rig. *Journal of Wind Engineering and Industrial Aerodynamics 96* (2008), 1218–1231.

[74] MAYER, J., SCHREFL, M., AND DEMUTH, R. On Various Aspects of Unsteady Aerodynamic Effects on Cars Under Crosswind Conditions. *SAE Technical Paper Series*, 07B-491 (2007).

[75] MENTER, F. Two-Equation Eddy-Viscosity Turbulence Models for Engineering Applications. *AIAA Journal 32*, 8 (1994), 1598–1605.

[76] MITSCHKE, M., AND WALLENTOWITZ, H. *Dynamik der Kraftfahrzeuge.* Springer-Verlag.

[77] MULLARKEY, S. *Aerodynamic Stability of Road Vehicles in Side Winds and Gusts.* PhD thesis, Imperial College London, 1990.

[78] NAKASHIMA, T., TSUBOKURA, M., IKENAGA, T., AND DOI, Y. HPC-LES for Unsteady Aerodynamics of a Heavy Duty Truck in Wind Gust - 2nd report: Coupled Analysis with Vehicle Motion. *SAE Technical Paper Series*, 2010-01-1021 (2010).

[79] NAKASHIMA, T., TSUBOKURA, M., MATSUDA, S., AND DOI, Y. Coupled Analysis of Unsteady Aerodynamics and 6DoF motion of a Heavy Duty Truck in Strong Wind Gusts. In *AIAA Applied Aerodynamics Conference* (Honolulu, USA, 2011).

[80] NEWNHAM, P., PASSMORE, M., AND BAXENDALE, A. Effect of Raised Freestream Turbulence on the Flow Around Leading Edge Radii. *SAE Technical Paper Series*, 2008-01-0473 (2008).

[81] OETTLE, N., SIMS-WILLIAMS, D., DOMINY, R., DARLINGTON, C., FREEMAND, C., AND TINDALL, P. The Effects of Unsteady On-Road Flow Conditions on Cabin Noise. *SAE Technical Paper Series*, 2010-01-0289 (2010).

[82] PASSMORE, M., AND MANSOR, S. The Measurement of Transient Aerodynamics Using an Oscillating Model Facility. *SAE Technical Paper Series*, 2006-01-0338 (2006).

[83] PASSMORE, M., RICHARDSON, S., AND IMAN, A. An Experimental Study of Unsteady Vehicle Aerodynamics. In *Journal of Automobile Engineering. Proceedings of the Institution of Mechanical Engineers – Part D* (2001), vol. 215.

[84] PERVAIZ, M., AND TEIXEIRA, C. Two Equation Turbulence Modeling with the Lattice-Boltzmann Method. *2nd International Symposium on Computational Technologies for Fluid-Thermal-Chemical Systems with Industrial Applications, ASME PVD Division Conference. Boston* (1999).

[85] PLATE, E. *Engineering meteorology: Fundamentals of Meteorology an Their Application to Problems in Environmental and Civil Engineering.* Elsevier, 1982.

[86] POPE, S. *Turbulent Flows.* Cambridge Univ. Press, 2009.

[87] RYAN, A. *The Simulation of Transient Cross-Wind Gusts and Their Aerodynamic Influence on Passenger Cars.* PhD thesis, University of Durham, 2000.

[88] RYAN, A., AND DOMINY, R. The Transient Aerodynamic Characteristics of a Passenger Vehicle Passing Through a Cross Wind-Jet. In *IMechE Automotive Vehicle Technologies* (1997), no. C524/117/97.

[89] SAUNDERS, J., AND WORDLEY, S. A Review of Measurement of Ambient Turbulence with Respect to Ground Vehicles. *SAE Technical Paper Series*, 2006-01-1028 (2006).

[90] SCHAEUFELE, S. *Validierung der neuen Windkanaele im Aerodynamischen Versuchszentrum der BMW Group und Analyse der Uebertragbarkeit der Ergebnisse.* PhD thesis, Karlsruhe Institute of Technology, 2010.

[91] SCHAIBLE, S. *Fahrzeugseitenwindempfindlichkeit unter natürlichen Bedingungen.* PhD thesis, RWTH Aachen.

[92] SCHLICHTING, H., AND GERSTEN, K. *Grenzschicht-Theorie.* Springer-Verlag, 1996.

[93] SCHREFL, M. *Instationäre Aerodynamik von Kraftfahrzeugen: Aerodynamik bei Überholvorgang und böigem Seitenwind.* PhD thesis, TU Darmstadt, 2008.

[94] SCHROECK, D., KRANTZ, W., WIDDECKE, N., AND WIEDEMANN, J. Instationäre aerodynamische Eigenschaften von Fahrzeugen unter böigem Seitenwind. In *Haus der Technik* (Munich, Germany, 2010).

[95] SCHROECK, D., WIDDECKE, N., AND WIEDEMANN, J. On-road Wind Conditions Experienced by a Moving Vehicle. In *FKFS Conference* (Stuttgart, Germany, 2007).

[96] SCHROECK, D., WIDDECKE, N., AND WIEDEMANN, J. Aerodynamic Response of a Vehicle Model to Turbulent Wind. In *FKFS Conference* (Stuttgart, Germany, 2009).

[97] SCHROECK, D., WIDDECKE, N., AND WIEDEMANN, J. The Effect of High Turbulence Intensities on Surface Pressure Fluctuations and Wake Structures of a Vehicle Model. *SAE Technical Paper Series*, 2009-01-0001 (2009).

[98] SHIH, T.-H., LIOU, W., SHABBIR, A., YANG, Z., AND ZHU, J. A New k-Epsilon

Eddy Viscosity Model for High Reynolds Number Turbulent Flows – Model Development and Validation. *NASA Technical Memorandum NASA-TM-106721* (1994).

[99] Sims-Williams, D. Cross Winds and Transients: Reality, Simulation and Effects. *SAE Technical Paper Series*, 2001-01-1041 (2001).

[100] Sims-Williams, D. *Self-Excited Aerodynamics Unsteadiness Associated with Passenger Cars.* PhD thesis, University of Durham, 2001.

[101] Sims-Williams, D., and Dominy, R. Experimental Investigation into Unsteadiness and Instability in Passenger Car Aerodynamics. *SAE Technical Paper Series*, 980391 (1998).

[102] Sims-Williams, D., and Dominy, R. The Validation and Application of a 5-Hole Pressure Probe with Tubing Transfer Function Correction for Time-Accurate Measurements in Unsteady Flows. In *MIRA International Vehicle Aerodynamics Conference* (England, 1998).

[103] Sockel, H. *Aerodynamik der Bauwerke.* Vieweg-Verlag, 1984.

[104] Succi, S. *The lattice Boltzmann Equation for Fluid Dynamics and Beyond.* University Press Oxford, 2001.

[105] Teixeira, C. Incorporating Turbulence Models into the Lattice-Boltzmann Method. *International Journal of Modern Physics C* (1998).

[106] Telionis, D., Fahrner, C., and Jones, G. An Experimental Study of Highway Aerodynamic Interferences. *Journal of Wind Engineering and Industrial Aerodynamics* (1984), 267–293.

[107] Theissen, P. *Unsteady Vehicle Aerodynamics in Gusty Crosswind.* PhD thesis, Technische Universitaet Muenchen.

[108] Theissen, P., Demuth, R., and Adams, N. A. Unsteady Phenomena in Vehicle Aerodynamics under Time-Dependent Flow Conditions. In *Stuttgart International Symposium* (Stuttgart, Germany, 2010).

[109] Theissen, P., Demuth, R., Wojciak, J., Indinger, T., and Adams, N. A. Instationäre aerodynamische Eigenschaften von Fahrzeugen unter böigem Seitenwind. In *Haus der Technik* (Munich, Germany, 2010).

[110] Theissen, P., Wojciak, J., Demuth, R., Indinger, T., and Adams, N. A. Unsteady Aerodynamic Phenomena under Time-Dependent Flow Conditions for Different Vehicle Shapes. In *MIRA International Vehicle Aerodynamics Conference* (England, 2010).

[111] Theissen, P., Wojciak, J., Heuler, K., Demuth, R., Indinger, T., and Adams, N. A. Experimental Investigation of Unsteady Vehicle Aerodynamics under Time-Dependent Flow Conditions - Part 1. *SAE Technical Paper Series*, 2011-01-0177 (2011).

[112] TRAN, V. T. Determining the Wind Forces and Moments Acting on Vehicles by Means of Pressure Sensors. *SAE Technical Paper Series*, 900313 (1990).

[113] TSUBOKURA, M., CHENG, S., NAKASHIMA, T., OKADA, Y., AND NOUZAWA, T. Simulation and Analysis of Effects of Dynamic Pitching for Idealized Sedan-Type Vehicle Models. *SAE Technical Paper Series*, 2011-01-0153 (2011).

[114] TSUBOKURA, M., IKEDA, J., NAKASHIMA, T., KITOH, K., AND KITAYAMA, M. On the Aerodynamics of Ground Vehicles Subjected to Crosswind Gust and its Shape Dependence. In *AIAA Applied Aerodynamics Conference* (Honolulu, USA, 2011).

[115] TSUBOKURA, M., KOBAYASHI, T., NAKASHIMA, T., NOUZAWA, T., NAKAMURA, T., ZHANG, H., ONISHI, K., AND OSHIMA, N. Computaional Visualization of Unsteady Flow around Vehicles Using High Performance Computing. *Computer and Fluids 38* (2009), 981–990.

[116] TSUBOKURA, M., NAKASHIMA, T., KITOH, K., AND SASAKI, Y. Development of Unsteady Aerodynamic Simulator Using Large-Eddy Simulation. In *FKFS Conference* (Stuttgart, Germany, 2009).

[117] TSUBOKURA, M., NAKASHIMA, T., OSHIMA, N., KITOH, K., ZHANG, H., ONISHI, K., AND KOBAYASHI, T. High Performance Computing for the Assessment of Unsteady Aerodynamic Forces on Vehicles Using Large Eddy Simulation. In *FKFS Conference* (Stuttgart, Germany, 2007).

[118] TSUBOKURA, M., TAKAHASHI, K., MATSUUKI, T., NAKASHIMA, T., IKENAGA, T., AND KITOH, K. HPC-LES for Unsteady Aerodynamics of a Heavy Duty Truck in Wind Gust - 1st report: Validation and Unsteady Flow Structures. *SAE Technical Paper Series*, 2010-01-1010 (2010).

[119] WAGNER, A. *Ein Verfahren zur Vorhersage und Bewertung der Fahrerreaktion bei Seitenwind.* PhD thesis, Universität Stuttgart, 2003.

[120] WALLENTOWITZ, H. *Fahrer - Fahrzeug - Seitenwind.* PhD thesis, TU Braunschweig, 1987.

[121] WATKINS, S., AND COOPER, K. The Unsteady Wind Environment of Road Vehicles, Part Two: Effects on Vehicle Development and Simulation of Turbulence. *SAE Technical Paper Series*, 2007-01-1237 (2007).

[122] WOJCIAK, J., ADAMS, N. A., INDINGER, T., THEISSEN, P., AND DEMUTH, R. Investigation of Unsteady Vehicle Aerodynamics under Time-Dependent Flow Conditions. In *AIAA Applied Aerodynamics Conference* (Honolulu, USA, 2011), no. 2011-3349.

[123] WOJCIAK, J., SCHNEPF, B., INDINGER, T., AND ADAMS, N. A. Study on the Capability of an Open-Source CFD Software for Unsteady Vehicle Aerodynamics. *SAE Technical Paper Series*, 2012-01-0585 (2012). Accepted.

[124] Wojciak, J., Theissen, P., Heuler, K., Indinger, T., Adams, N. A., and Demuth, R. Experimental Investigation of Unsteady Vehicle Aerodynamics under Time-Dependent Flow Conditions - Part 2. *SAE Technical Paper Series*, 2011-01-0164 (2011).

[125] Wojciak, J., Theissen, P., Indinger, T., Adams, N. A., and Demuth, R. Experimental Study of On-Road Aerodynamics during Crosswind Gusts. In *MIRA International Vehicle Aerodynamics Conference* (England, 2010).

[126] Wordley, S., and Saunders, J. On-Road Turbulence. *SAE Technical Paper Series*, 2008-01-0475 (2008).

[127] Wordley, S., and Saunders, J. On-Road Turbulence: Part 2. *SAE Technical Paper Series*, 2009-01-0002 (2009).

[128] Zhu, J., and Shih, T.-H. Calculations of Diffuser Flows with an Anisotropic k-Epsilon Model. *NASA Contractor Report CR-198418* (1995).